

## Stratospheric Plume Dispersion: Measurements from STS and Titan Solid Rocket Motor Exhaust

20 April 1999

Prepared by

E. J. BEITING  
Mechanics and Materials Technology Center  
Technology Operations

Prepared for

SPACE AND MISSILE SYSTEMS CENTER  
AIR FORCE MATERIEL COMMAND  
2430 E. El Segundo Boulevard  
Los Angeles Air Force Base, CA 90245

Systems Planning and Engineering

APPROVED FOR PUBLIC RELEASE;  
DISTRIBUTION UNLIMITED

 **THE AEROSPACE  
CORPORATION**  
Segundo, California

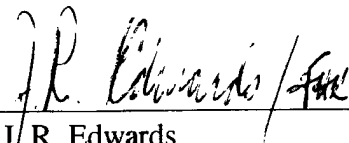
DTIC QUALITY INSPECTED 4

19990909 055

This report was submitted by The Aerospace Corporation, El Segundo, CA 90245-4691, under Contract No. F04701-93-C-0094 with the Space and Missile Systems Center, 2430 E. El Segundo Blvd., Los Angeles Air Force Base, CA 90245. It was reviewed and approved for The Aerospace Corporation by P. D. Fleischauer, Principal Director, Mechanics and Materials Technology Center. Mr. John R. Edwards was the project officer.

This report has been reviewed by the Public Affairs Office (PAS) and is releasable to the National Technical Information Service (NTIS). At NTIS, it will be available to the general public, including foreign nationals.

This technical report has been reviewed and is approved for publication. Publication of this report does not constitute Air Force approval of the report's findings or conclusions. It is published only for the exchange and stimulation of ideas.

A handwritten signature in cursive script, appearing to read "J.R. Edwards", is written over a horizontal line.

J. R. Edwards  
SMC/AXFV

REPORT DOCUMENTATION PAGE			Form Approved OMB No. 0704-0188	
Public reporting burden for this collection of information is estimated to average 1 hour per response, including the time for reviewing instructions, searching existing data sources, gathering and maintaining the data needed, and completing and reviewing the collection of information. Send comments regarding this burden estimate or any other aspect of this collection of information, including suggestions for reducing this burden to Washington Headquarters Services, Directorate for Information Operations and Reports, 1215 Jefferson Davis Highway, Suite 1204, Arlington, VA 22202-4302, and to the Office of Management and Budget, Paperwork Reduction Project (0704-0188), Washington, DC 20503.				
1. AGENCY USE ONLY (Leave blank)		2. REPORT DATE 20 April 1999		3. REPORT TYPE AND DATES COVERED
4. TITLE AND SUBTITLE Stratospheric Plume Dispersion: Measurements from STS and Titan Solid Rocket Motor Exhaust			5. FUNDING NUMBERS  F04701-93-C-0094	
6. AUTHOR(S)  E. J. Beiting				
7. PERFORMING ORGANIZATION NAME(S) AND ADDRESS(ES) The Aerospace Corporation Technology Operations El Segundo, CA 90245-4691			8. PERFORMING ORGANIZATION REPORT NUMBER  TR-99(1306)-1	
9. SPONSORING/MONITORING AGENCY NAME(S) AND ADDRESS(ES) Space and Missile Systems Center Air Force Materiel Command 2430 E. El Segundo Boulevard Los Angeles Air Force Base, CA 90245			10. SPONSORING/MONITORING AGENCY REPORT NUMBER  SMC-TR-99-24	
11. SUPPLEMENTARY NOTES				
12a. DISTRIBUTION/AVAILABILITY STATEMENT  Approved for public release; distribution unlimited			12b. DISTRIBUTION CODE	
13. ABSTRACT (Maximum 200 words)  Plume expansion was measured from nine Space Shuttle and Titan IV vehicles at altitudes of 18, 24, and 30 km in the stratosphere. The plume diameters were inferred from electronic images of polarized, near-infrared solar radiation scattered from the exhaust particles, and these diameters were found to increase linearly with time. The expansion rate was measured for as long as 50 min after the vehicle reached altitude. Measurements made simultaneously at multiple altitudes showed that the expansion rate increased with increasing altitude for six measurements made at Cape Canaveral but decreased between 24 and 30 km for the one measurement made at Vandenberg AFB. The average expansion rates for all measurements are $4.3 \pm 1.0$ m/s at 18 km, $6.8 \pm 1.9$ m/s at 24 km, and $8.7 \pm 2.5$ m/s at 30 km. Expansion rates varied from launch to launch by as much as a factor of 1.6 at 18 km, 2.2 at 24 km, and 2.7 at 30 km. No correlation between the expansion rate and wind speed or shear was evident. These data are compared to several models for diffusivity and are used to update a comprehensive particle model of solid rocket motor exhaust in the stratosphere. The expansion rates are required by models to calculate the spatial extent and temporal persistence of the local stratospheric ozone depletion cause by solid rocket exhaust.				
14. SUBJECT TERMS Plume dispersion, Stratospheric diffusion, Rocket exhaust, Stratospheric ozone depletion, Solid rocket motor plume, Air pollution, Environmental impact, Launch vehicles, Ozone depletion			15. NUMBER OF PAGES 77	
			16. PRICE CODE	
17. SECURITY CLASSIFICATION OF REPORT UNCLASSIFIED	18. SECURITY CLASSIFICATION OF THIS PAGE UNCLASSIFIED	19. SECURITY CLASSIFICATION OF ABSTRACT UNCLASSIFIED	20. LIMITATION OF ABSTRACT	

## **Acknowledgments**

The author acknowledges the exceptional support given before, during, and after each field trip by Mr. Luis Ortega. Mr. Douglas Schulthess provided excellent logistical support for all CCAS launches. Camera operators and support crew for various launches also included Messrs. Jerry Brokow, John Gladwell, Eric Fournier, William Hansen, Jimmy Kephart, Richard Reyes, John Diaz, John Ligda, Chris Ihde, and Drs. Valerie Lang and Ronald Cohen. The cooperation of Chevron USA and Bixby Ranch for access to the Harvest Oil Platform and Bixby Ranch for the K-13 launch is gratefully acknowledged.



## Contents

1. Introduction.....	1
2. Method and Instrumentation.....	3
3. Data Acquisition and Processing.....	5
4. Results.....	7
5. Diffusivity.....	11
6. Generalized Particle Model for a SRM Plume in the Stratosphere.....	15
7. Summary.....	19
References.....	21
Appendix 1—STS-80 Analysis.....	23
Appendix 2—K-13 Analysis.....	29
Appendix 3—STS-83 Analysis.....	49
Appendix 4—STS-94 Analysis.....	53
Appendix 5—STS-85 Analysis.....	57
Appendix 6—STS-90 Analysis.....	63
Appendix 7—STS-91 Analysis.....	71

## Figures

1. Instruments used for recording dynamic and static images of the plume.....	3
2. Plot of stratospheric wind speed versus plume expansion rate.....	9
3. Plot of stratospheric vertical wind speed shear and directional shear versus rate.....	10
4. Correlation study of plume expansion rate to diffusion parameter.....	13

## Tables

1. Optical Characteristics of Instruments.....	4
2. Stratospheric Plume Data Synopsis .....	8
3. Averages of Plume Expansion Rates .....	10
4. Stratospheric Plume Diffusivity Study.....	14

## 1. Introduction

Recent models predict that stratospheric ozone concentrations in the exhaust of solid rocket motors are depressed by after-burning HCl [Danilin, 1993; Kruger, 1994; Zittel, 1994; Denison *et al.*, 1994; Ross, 1996; Brady *et al.*, 1997]. This prediction instigated a number of measurements [Hanning-Lee, *et al.*, 1996; Dao *et al.*, 1997; Ross *et al.*, 1997; Molina *et al.*, 1997; Beiting, 1997a; Burke and Zittel, 1998; Ross *et al.*, 1999]. A recent bibliography on the environmental impacts of launch vehicles is available [Cocchiaro, 1998]. Ross *et al.* [1997] verified ozone depletion in the exhaust of two Titan IV rockets in the lower stratosphere. This local depletion could be significant (>50%) even two hours after launch. In all models of this phenomenon, the size and persistence of the predicted reduced ozone concentrations are sensitive functions of the plume dispersion rate. Unfortunately, measurements of this rate were nearly nonexistent. The total observational database consists of a Titan III plume expansion rate taken from photographic images measured more than 20 years ago at an altitude of 18 km [Hoshizaki, 1975] and two recently reported measurements made in this series of plumes at 30 km [Beiting & Klingberg, 1997; Beiting, 1997a]. These previous measurements were of short duration (~10 min) and at a single altitude.

In this report, data are presented from seven additional launches acquired using instruments that image the polarized near-infrared sunlight scattered off the solid plume particles. Six of the observations were made of plumes from the Space Shuttle launched from Cape Canaveral Air Station (CCAS) and one was made of a Titan IV (K-13) launched from Vandenberg Air Force Base (VAFB). Expansion rates were measured at altitudes of 18, 24, and 30 km with duration as long as 50 min. The data from the Vandenberg launch are notable because the plume was imaged at the 24 km altitude simultaneously from two sites at nearly orthogonal views allowing a three-dimensional understanding of the interaction of the rocket plume with the stratosphere to be obtained. Adding these seven measurements to the three previously reported single-altitude, short-duration measurements creates a database of sufficient size to identify trends. Although the expansion rates show considerable variability from launch to launch, a clear pattern of increasing expansion rate with altitude is evident.



## 2. Method and Instrumentation

The data were acquired as electronic video and still images. The instruments imaged near-infrared, polarized solar radiation scattered from the plume particles. By choosing the correct wavelength, polarization, and scattering angle of the radiation, the contrast of the image of the plume against the bright sky could be enhanced considerably, allowing the viewing time of the plume to be increased. The principles and details of the method used are discussed in detail elsewhere [Beiting, 1998], and only a brief description of the instruments is presented here.

Three video recording instruments and one high-resolution electronic still camera were built to study the morphology of the plume. Figure 1 is a diagram showing the principal components of the instruments. The video camera is a Hitachi KP-160 high-sensitivity CCD with 786 horizontal and 488 vertical pixels where the pixels have a 100% fill factor. These pixels are rastered into 570 horizontal and 350 vertical television lines. With the IR cut-off filter removed, the spectral sensitivity of the camera peaks at 800 nm and has good response to 1100 nm. Each of these cameras was equipped with an 8–48 mm zoom lens, a spectral filter, and an IR polarizer. The filter and polarizer were cut to fit in standard 49-mm-diam threaded lens mounting rings, allowing quick interchange and stacking of optical components. The composite spectral response curves for the instruments have a peak near 900 nm.

The video images are recorded at SVHS resolution with voice annotation using portable video recorders. The cameras are mounted on commercial tripod heads that were modified with two pairs of orthogonally mounted gears, each pair coupled to an optical encoder that fed signals to digital readouts for the azimuth and elevation of the image. The images are monitored during launch using high-resolution black and white video monitors. This wide range of fields-of-view enables images of the plume to be recorded with good spatial resolution for nearly an hour of expansion. Recording the azimuth and elevation of the plume centerline permitted the wind direction and speed be measured (assuming that there is no vertical component to the stratospheric winds).

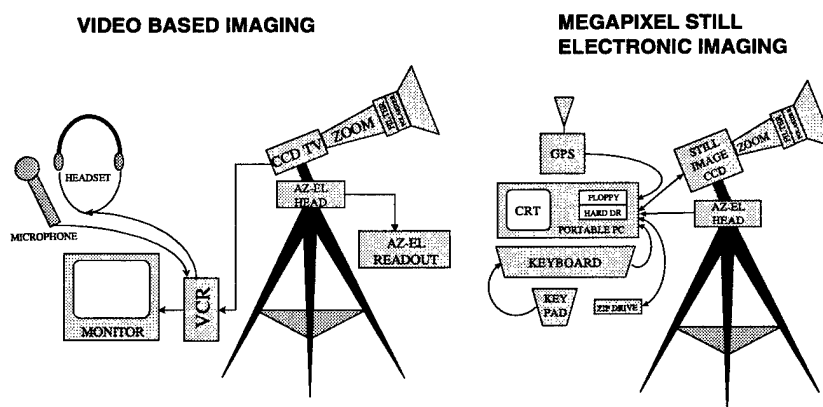


Figure 1. Instruments used for recording dynamic and static images of the plume.

Raster noise reduces the signal-to-noise ratio of the video images to about 5 bits (32 gray levels). To enhance both spatial resolution and contrast, a Kodak Megapixel 1.6i CCD camera with 1.533 million pixels and 10-bit intensity resolution was acquired. This camera was mated to a fast digital frame grabber and equipped with a standard 35-mm wide-angle zoom lens, spectral filter, and polarizer. Numerical image processing was used to enhance the digital images.

The images recorded of objects with known widths were used to spatially calibrate the instruments. That is, the actual width,  $W$ , of the plume is calculated from its image width,  $w$ , knowing the distance,  $D$ , from the camera-to-plume segment (calculated from the rocket trajectory) and a focal-length-dependent calibration factor,  $d_f$ , which was measured in the laboratory, *viz*,

$$W = D \frac{w}{d_f}. \quad (1)$$

The measured fields-of-view (FOV) and reciprocal dispersions on the readout medium for the various focal lengths used are presented in Table 1. The maximum field-of-view for both instruments is about 40°, but the video instruments had much higher magnifications available than the Kodak still camera. The video instruments had greater dispersion, but this advantage is offset somewhat by the greater spatial resolution and by the ability to image enhance the high-resolution, 10-bit still images.

Table 1. Optical Characteristics of Instruments

Camera/Readout	Focal Length (mm)	FOV (deg)	Reciprocal Dispersion (deg/cm)
Hitachi/Monitor	8	38.9	0.94
Hitachi/Monitor	10	33.6	0.81
Hitachi/Monitor	15	22.3	0.54
Hitachi/Monitor	20	17.2	0.41
Hitachi/Monitor	30	11.4	0.275
Hitachi/Monitor	48	7.10	0.17
Kodak/Hardcopy	18	40.6	2.09
Kodak/Hardcopy	35	23.0	1.15

### 3. Data Acquisition and Processing

The data acquisition procedure was straightforward. Each operator of a video camera was assigned one or two of the target altitudes (18, 24, or 30 km). The operator tracked the vehicle to the assigned altitude (using the time-to-altitude obtained from the precalculated trajectory) and identified a feature near this altitude in order to follow the plume segment as it blew across the sky. This method of tracking altitude used the fact that there was little vertical component to the stratospheric winds. Periodically, the operator would read in the camera's azimuth and elevation onto the audio portion of the video tape. Usually the focal length of all three cameras was initially set to 48 mm, yielding a horizontal field-of-view of 7°. As the plume expanded, the focal lengths would be decreased sequentially to 30, 20, 15, and 10 mm. The operators adjusted the focal length of the zoom lens to keep the plume width between 20% and 80% of the screen size, thus assuring a resolution of at least 100 pixels across the plume width. This procedure was also followed for the electronic still camera. Here, however, the first images were taken when the rocket reached each of the target altitudes. Subsequently, images were stored every 15 to 30 s to record a clear progression of the changing plume morphology.

Most data were acquired using the three video recorder instruments; the still instrument became operational late in the program. Estimates of plume width from the video tape images were made by eye directly from a large (41.4 cm x 30.8 cm) SVHS video monitor. The large size and the significant image enhancement created by the eye averaging multiple video frames yielded more accurately measured widths than could be obtained from smaller hardcopy images. Estimates of plume widths from the still camera images were taken from laser jet printed images (20.3 cm x 13.8 cm) after image processing.

More sophisticated methods of data analysis (i.e., digitization of a line of pixels across the plume and defining a full-width-half-maximum-FWHM) were not warranted because the complex plume morphology at all but the earliest times (<5 min.) created considerable ambiguity in selecting a width. For example, even at early times, side-by-side features could differ significantly in width [Beiting & Klingberg, 1997] where at later times these features could coalesce into a single feature; or the plume would develop open sections, rendering the definition of a FWHM meaningless. In these situations, the ability of the eye to identify and associate disparate structures is unsurpassed. Thus, the plume extent could be assigned under complex and dynamic conditions even when a highly structured plume had an angular extent as large as 40°.

It is also for these reasons that traverses through the plume by aircraft or by LIDAR beams that sample only a part of the plume without knowledge of the total plume morphology are not useful for defining an expansion rate. These techniques can provide a consistency check [Beiting, 1997a], but a temporal history of the entire plume structure is required for a measure of plume dispersion. Because of these highly variable structures, all measured diameters are assigned an accuracy of  $\pm 10\%$ .

## 4. Results

A detailed analysis of the data from the seven launches discussed in this report is presented in Appendices 1–7. Analysis of data from two previous measurements of this series is described in a previous report [Beiting and Klingberg, 1997] and in a publication on plume particles [Beiting, 1997a]. In this section, all results are presented and compared to the one previous single-altitude measurement made much earlier by Hoshizaki [1975].\*

When the widths inferred from the images are graphed as a function of time, the plots are remarkably linear. The data and the linear fits used to infer expansion rates are shown in Appendices 1–7. The results of the seven launches as well as analysis the three previous launches are listed chronologically in Table 2. The values in this table were the slopes obtained from linear regression fits to the plume widths and are averages when multiple measurements at a given altitude were made. The short observation times shown for some of the launches were usually caused by portions of the tropospheric (low altitude) plume or clouds blowing in front of the stratospheric section of the plume being monitored. The longest observation times (25 to 50 min) were terminated because of clouds, or because the edge of the plume expanded beyond the FOV of the camera. Although nearly all the  $R^2$  values\*\* listed in Table 2 are greater than 0.96, indicating good linearity, some of the longer observations show considerable deviations from the average expansion rates. For example, the subinterval expansion rate at the 27 and 30 km altitudes of STS-90 could vary from the lowest to highest rate by a factor of 2 to 3. In contrast, the expansion rate of the 17 km altitude plume section of STS-85 was remarkably constant over a 36-min interval.

The wind direction and speed from rawinsonde data are also listed in Table 2. The plume speed also could be inferred from the motion and direction of the plume centerline. Whenever comparison was made between those two sets of wind speeds (K-2, K-13, STS-85, STS-94, STS-90), the plume speed was found to be in reasonable agreement with rawinsonde data. Comparison of the wind speed with the expansion rate shows that there is no obvious correlation between wind speed and expansion rate. For example, the wind speed does increase with altitude for the K-13 flight, but the expansion rate does not. While the expansion rate increases with altitude for the remainder of the flights, the wind speed decreases with altitude for half of them (STS-83, STS-90 and STS-91) and increases for the other half (STS-80, STS-94, STS-85). The plot of wind speed and expansion rate presented in Figure 2 confirms this observation. This lack of correlation holds true even for a single segment of a given plume if it showed considerable variability in both expansion rate and velocity. The expansion rate of STS-94 at an altitude of 30 km varied nearly a factor of 3 among 4 3-min subintervals of its 13 min observation interval. The velocity of this plume segment varied between 0 and 17 m/s during

---

\*Expansion of a plume from a Delta II vehicle was measured near an altitude of 27 km for a period of 1.5 min. [R. N. Abernathy, personal communication, 1998.] This unpublished result is not included in this analysis because expansion rates during the first 2 min can differ considerably from longer ( $\geq 10$  min) rates.

\*\* $R^2$  returns the square of the Pearson product moment correlation coefficient through data points in known y's and known x's. The R-squared value can be interpreted as the proportion of the variance in y attributable to the variance in x.

Table 2. Stratospheric Plume Data Synopsis

IDENTIFICATION		WIND		PLUME DATA	
Launch ID Date Vehicle-LT* Rawinsonde-LT	Alt (km)	Speed (m/s) Direction	SHEAR: Speed/ Direction (m/s/km)\ (deg/km)	Obs Time (min)	Expansion Rate (R²) (m/s)
Titan? [1] VAFB	18	NA		10	6.2(0.94)
4 Oct 74	24	--		--	--
?	30	--		--	--
K-10 [2] KSC					
7 Feb 94	18	--		--	--
2147 UT	24	--		--	--
1716 UT	30	15-W(21km)	-3\0	10	10(0.99)
K-2 [3] KSC					
2 July 96	18	--		--	--
3 July 0030 UT	24	--		--	--
2 July 2330 UT	30	7-E(20km)	3\ -20	12	9.0
STS-80 KSC					
19 Nov 96	18	--		--	--
1956 UT	24	20-W	-1\ -26	3	6.8 (0.98)
1623 UT	30	25-W	1\ 5	2	10 (0.98)
K-13 VAFB					
20 Dec 96	18	--		--	--
1804 UT	24	7-W	4.3\ 3	10	8.2 (0.98)
1749 UT	30	15-W	0\ 0	10	5.2 (0.98)
STS-83 KSC					
4 April 97	18	--		--	--
1920 UT	24	10-E	0\ 46	3.0	4.5 (0.97)
1905 UT	30	10-N	2\ 150	3.5	7.5 (0.97)
STS-94 KSC					
1 July 97	18	--		--	--
1802 UT	24	8-E	2\ 15	7	10.1 (0.94)
1720 UT	30	10-E	1.5\ 22	12	13.7 (0.98)
STS-85 KSC					
7 Aug 97	17	2.5-S	-3.5\ 200	36	3.1 (0.99)
1441 UT	24	15-E	-4\ 7	7	5.3 (0.96)
1411 UT	30	30-E	4\ 0	8	6.5 (0.99)
STS-90 KSC					
17 April 98	18	10-NW	-5\ 21	3	4.7 (0.80)
1819 UT	24	6-SE	1\ 33	4	5.8 (0.98)
1819 UT	27	5-E	1\ 37	25	7.0 (0.98)
1949 UT	30	4-E		25	8.0 (0.98)
STS-91 KSC					
2 June 98	18	10-N	-6\ 0	50	5.1 (0.99)
2206 UT	24	8-E	2\ -7	10	6.9 (0.99)
2135 UT	30	10-E	-1\ -12	25	8.7 (0.97)

\*LT = Launch Time: EST = UT - 5 and EDT = UT - 4; PST = UT - 8 and PDT = UT - 7. The vehicle reached the stratosphere in 1.5 min, whereas the rawinsonde balloon required about 60 min to reach these altitudes. [1] = Hoshizaki, 1973; [2] = Beiting, 1997a; [3] = Beiting & Klingberg, 1997

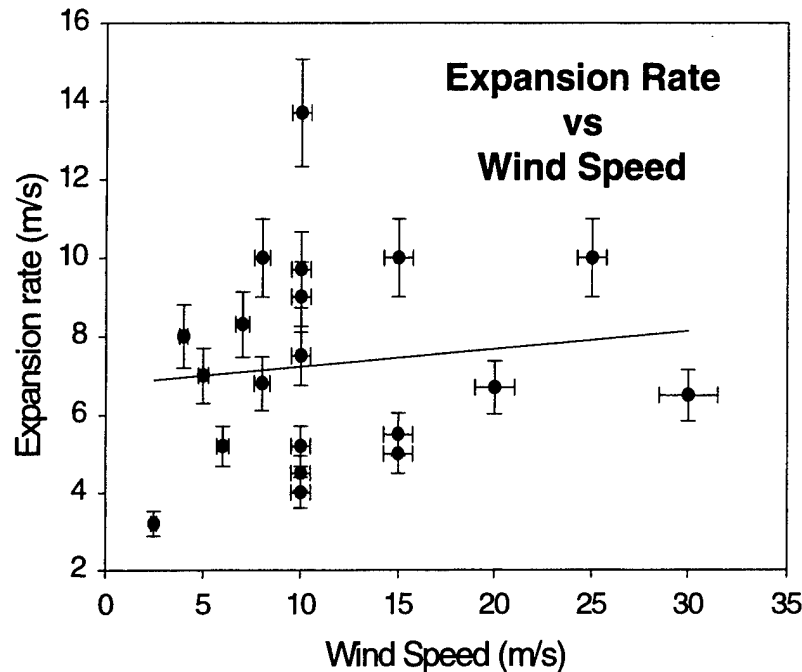


Figure 2. Plot of stratospheric wind speed versus plume expansion rate showing little correlation between the two parameters. A linear fit of wind speed to expansion rate has a correlation coefficient ( $r^2$ ) of 0.01.

these subintervals with no obvious correlation between this plume centerline speed and the expansion rate (see Tables 4-1 and 4-2 in Appendix 4). Therefore, based on these data we conclude that variation in wind speed is not responsible for the observed variation in expansion rates.

A similar comparison can be made with wind shear. Vertical wind shear (rate of change of wind speed or direction with altitude) can be calculated from the rawinsonde data albeit with large error. The results from this exercise are present in column 4 in Table 2. Figure 3 compares the speed and directional wind shear values with the expansion rate. Again no discernable pattern is evident.

The predominate trend in the data is increasing expansion rate with increasing altitude. This relationship is seen for all east coast rates where diameters at multiple altitudes were measured simultaneously. Only the one measurement made at the Western Test Range (K-13), shows a decrease in expansion rate between 24 and 30 km. Whether there is a difference between the east and west coast expansion rates with altitude or this is an anomaly of this one measurement cannot be answered without additional west coast measurements.

Table 3 averages the expansion rates for all altitudes for the nine launches taken during the course of this work and for the east coast launches only. There is not a significant difference between the two sets of averages although the east coast averages show the trend of increasing expansion rate with increasing altitude more clearly. The expansion rates have standard deviations between 20–30%, but the ratio of the extreme values of the rate at a given altitude can be 10 times larger than this standard

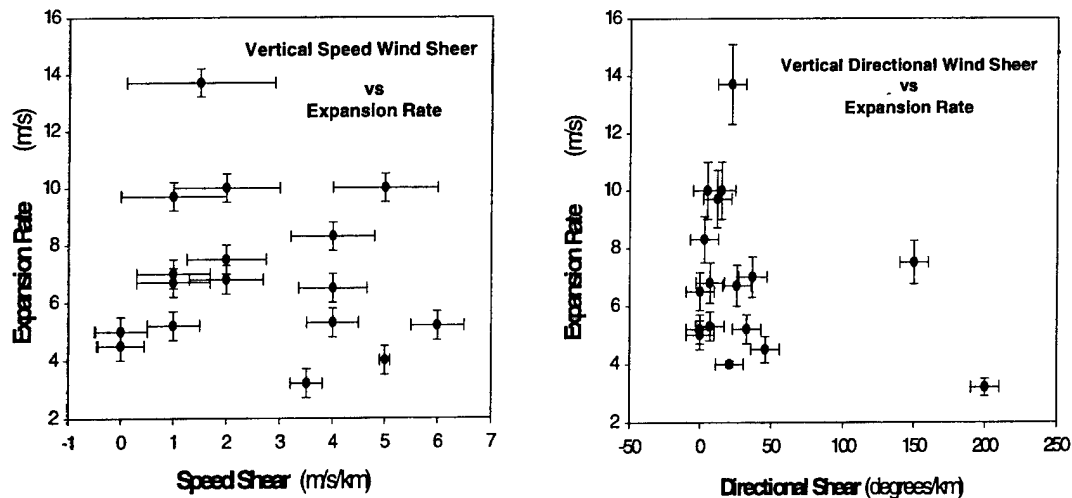


Figure 3. Plot of stratospheric vertical wind speed shear and directional shear versus rate showing little correlation between the plume expansion rate and either parameter.

deviation. In general, there is about a 50% increase in expansion rate between 18 and 24 km altitude and between 24 and 30 km altitude or a factor of 2 increase in expansion rate from 18 to 30 km. Note that the extreme variation in expansion rate from measurement to measurement at a given altitude (presented in the last column of Table 3) is significantly larger than this increase with altitude.

The data obtained from the K-13 launch are noteworthy because two, nearly orthogonal, views of the plume were obtained at an altitude of 24 km. This was accomplished by placing a camera nearly directly under the flight path on an oil platform 10 km off shore and another onshore camera that viewed the side of the plume at the same altitude (see Fig 2-1 in Appendix 2). These two views helped to differentiate between pure plume expansion and the plume shearing into packets. This differentiation was important for defining the chemical dilution rate. The series of images given in Appendix 2 indicate that although the plume does sheer into identifiable segments or packets, these segments expand nearly uniformly in cross section, continuing the chemical dilution process for the 10-min expansion interval observed at this launch.

Table 3. Averages of Plume Expansion Rates

Altitude (km)	Avg Rate: All (m/s)	Avg Rate East Only (m/s)	Max Variation Ratio
18	4.3 ± 1.0	4.3 ± 1.0	1.6
24	6.8 ± 1.9	6.6 ± 2.0	2.2
30	8.7 ± 2.4	9.2 ± 2.2	2.6

## 5. Diffusivity

The dispersion of an ensemble of particles in the atmosphere is commonly modeled using the diffusion equation. This equation simply indicates that the time rate of change in the particle concentration at a point is proportional to the spatial rate of change of the density gradient with a proportionality constant,  $K_d$ , called the diffusivity:

$$\frac{dn}{dt} = K_d \nabla^2 n. \quad (2)$$

For a rocket plume, there is no gradient along the axis of the plume, and expansion is solely in the radial direction (advection is removed by allowing the coordinate system of the plume to move with the wind). For a line source and a constant diffusivity, the solution to Eq. 4-1 of Appendix 4 has a Gaussian radial dependence as is commonly used in modeling plumes from smokestacks [Stern *et al.* 1973]:

$$n(x, y, t) = \frac{Q}{4\pi K_d t} \exp\left[-(x^2 + y^2) / 4K_d t\right] \quad (3)$$

The criterion for identifying the edge of the plume is somewhat instrument and operator dependent. However, the plume is visible only if the integrated concentration along the line of sight is above some threshold. This method of the visible threshold was proposed early [Roberts, 1923] and has been used many times [Joseph *et al.*, 1975]. Accordingly, if the radius of the plume is  $y_0$  at this constant threshold value,  $T$ , then

$$\begin{aligned} T &= \int_{-\infty}^{\infty} n(x, y_0, t) dx \\ &= 2 \frac{Q}{4\pi K_d t} \exp(-y_0^2 / 4K_d t) \int_0^{\infty} \exp(-x^2 / 4K_d t) dx \\ &= \frac{Q}{2\sqrt{\pi K_d t}} \exp\left(-\frac{r_e^2}{4K_d t}\right) \end{aligned} \quad (4)$$

where  $r_e$  in the last line is defined as the observed edge of the plume. Then

$$\frac{r_e^2}{t} = -2K_d \ln t + \text{constant} \quad (5)$$

and we see that a plot of  $r_e^2 / t$  versus  $\ln(t)$  should be linear and have a slope of  $-2K_d$  if this model is valid.



Assuming that the threshold for detection of the plume edge was a constant value of density, *Denison et al.* [1994] found that the spatial and temporal dependence of this solution did not agree with the plume expansion of rocket exhaust measured at 18 km as reported by *Hoshizaki*, [1975]. Subsequently, they proposed a size-dependent diffusivity ( $K_d = br$ ) used in a form of the diffusion equation that permitted the first partial derivative of this diffusivity:

$$\frac{\partial n}{\partial t} = \frac{1}{r} \frac{\partial}{\partial r} r K \frac{\partial n}{\partial r} \quad (6)$$

with the line source solution

$$n(r) = \frac{A}{t^2} \exp\left(-\frac{r}{bt}\right). \quad (7)$$

This interpretation of the diffusivity is consistent with the diffusion of a plume being driven by the small eddies in the turbulent spectrum on the order of the plume size and not by the much larger integral scale of the atmosphere, which give plume dissipation times on the order of milliseconds. Using this constant-density criterion, they noted that a plot of  $r/t$  versus  $\ln(t)$  for the data would yield a straight line with slope of  $-2b$  for a diffusivity with linear radial dependence. This procedure provided reasonable agreement with the *Hoshizaki* data.

Assuming the functional form for the particle density of *Denison et al.*, but applying a constant integrated concentration criterion for edge detection, we have

$$\begin{aligned} T &= \int_{-\infty}^{\infty} n(r, t) dx \\ &= 2 \frac{A}{t^2} \int_0^{\infty} \exp[-(x^2 + y_0^2)^{1/2} / bt] dx \\ &= 2 \frac{A}{t^2} \int_{y_0}^{\infty} \frac{u e^{-u/bt}}{\sqrt{u^2 - y_0^2}} du \\ &= \frac{2A}{t^2} [y_0 K_1(y_0 / bt)] \end{aligned} \quad (8)$$

where  $K_1(z)$  is the modified Bessel function [see *Gradshteyn and Ryzhik*, 1965, p 316, 3.365-2, for the evaluation of the integral]. A useful asymptotic expansion of  $K_\nu(z)$  is [*Arfkin*, 1970] p. 508]:

$$K_\nu(z) \approx \sqrt{\frac{\pi}{2z}} e^{-z} \left[ 1 + \frac{(4\nu^2 - 1^2)}{1!8z} + \frac{(4\nu^2 - 1^2)(4\nu^2 - 3^2)}{2!(8z)^2} + \dots \right]. \quad (9)$$

For a real argument  $>3$ , (if  $b \approx 1$ , this condition is met for expansion rates  $>3$  m/s),  $K_1(z)$  can be approximated to 10% accuracy using the leading term only, allowing Eq. (8) to be written:

$$T \equiv A\sqrt{2\pi b} \left( \frac{r_e}{t^3} \right)^{1/2} e^{-r_e/bt} \quad (10)$$

where  $r_e$  has been substituted for  $y_0$ . If this analysis is correct then a plot of  $r_e/t$  versus  $\ln(t^3/r_e)$  would be linear with a slope of  $-b/2$ .

The results of the analysis of the data for these three methods are shown in Table 4. There is consistently poor agreement between the data and the Gaussian model. The plots of  $r_e^2/t$  versus  $\ln t$ , in general, are not linear (as indicated by  $R^2$  values  $<0.90$ ), and the fits have negative slopes yielding unphysical values for the diffusion constant. The diffusivity model advocated by *Denison et al.* fits the data better than the Gaussian model, although the agreement is not particularly good. Using the integral edge detection analysis with this model does produce somewhat better fits for all the data and yields a diffusivity parameter,  $b$ , about twice that obtained from using the constant density criterion for edge detection.

We note that there is poor correlation between the linear expansion rates and the  $b$  value. This can be seen in Figure 4. The  $R^2$  correlation parameter for a linear fit between expansion rate and the  $b$  parameter obtained from the model using either of the edge criteria is below 0.2. The poor correlation is not unexpected since none of the models yields a constant expansion rate as is indicated by most of the data.

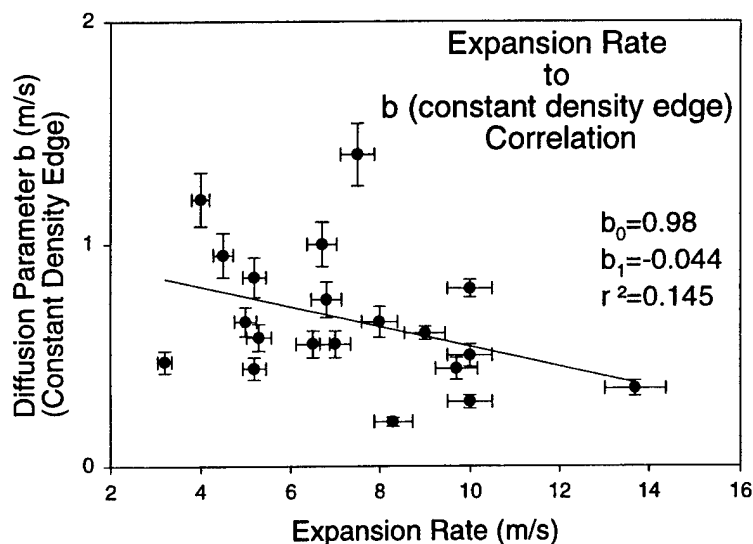


Figure 4. Correlation study of plume expansion rate to diffusion parameter. A linear fit of the diffusion parameter to expansion rate has a correlation coefficient ( $R^2$ ) of 0.145 using the constant density edge criterion and 0.056 for the constant integral edge criterion. The  $b_0$  and  $b_1$  values are the ordinate intercept and slope of the line fit to the data.

Table 4. Stratospheric Plume Diffusivity Study

IDENTIFICATION			Gaussian Solution, Constant Integral Edge $r^2/t = -2K \ln t - e$ ; $K = \text{constant}$			Dennison Solution; Constant Density Edge $r/t = -2b \ln t - a$ ; $K = br$ ;			Dennison Solution; Constant Integral Edge $r/t = -(b/2) \ln(t^2/r) - d$ ; $K = br$ ;		
Launch ID	Alt (km)	Obs Time (min)	Fitting Interval (min)	Diffusivity Slope -2K	Goodness of Fit $R^2$	Diffusivity Slope -2b (m/s)	Goodness of Fit $R^2$	Diffusivity Slope -b/2 (m/s)	Goodness of Fit $R^2$	Diffusivity Slope -b/2 (m/s)	Goodness of Fit $R^2$
Titan? [VAFB 4 Oct 74 ?	18	10	1-10	1340	0.50	-2.6**	0.92	-1.11**	0.94		
	24	--	--	--	--	--	--	--	--		
	30	--	--	--	--	--	--	--	--		
K-10 [KSC 7 Feb 94 2147 UT 1716 UT	18	--	--	--	--	--	--	--	--		
	24	--	--	--	--	--	--	--	--		
	30	10	0.5-10(2-10)	4840(7525)	0.82(0.85)	-0.57	0.61	-0.49	0.76		
K-2 [KSC 2 July 96 3 July 0030 UT 2 July 2330 UT	18	--	--	--	--	--	--	--	--		
	24	--	--	--	--	--	--	--	--		
	30	12	0-12(0-1.5/2-12)	1240	0.96	-1.2(3.9/0.08)	0.63(0.99/0.09)	-0.55	0.69		
STS-80 KSC 19 Nov 96 1956 UT 1623 UT	18	--	--	--	--	--	--	--	--		
	24	3	0-3	630	0.96	-2.0	0.99	-0.84	0.99		
	30	2	0.3-2	1540	0.97	-1.6	0.88	-0.73	0.90		
K-13 VAFB 20 Dec 96 1804 UT 1749 UT	18	--	--	--	--	--	--	--	--		
	24	10	1-9(1-3/3-9)	2770	0.91	-0.4(1.5/0.5)	0.5(0.99/0.5)	-0.18(0.62/0.23)	0.52(0.99/0.57)		
	30	10	1-10	1250	0.77	-1.3	0.90	0.56	0.92		
STS-83 KSC 4 April 97 1920 UT 1905 UT	18	--	--	--	--	--	--	--	--		
	24	3.0	0.5-3	210	0.37	-1.9	0.93	-0.78	0.95		
	30	3.5	0.3-4	475	0.65	-2.8	0.92	-1.2	0.94		
STS-94 KSC 1 July 97 1802 UT 1720 UT	18	--	--	--	--	--	--	--	--		
	24	7	0-7(0-4/4-7)	1123(50/1950)	0.21(0.01/0.98)	-1.0(1.9)	0.5(0.99)	-0.50(0.82)	0.58(0.99)		
	30	12	0-12(0-4)	9480(2030)	0.66(0.88)	-0.7(2.0)	0.3(0.95)	-0.35(0.89)	0.38(0.96)		
STS-85 KSC 7 Aug 97 1441 UT 1411 UT	17		1-36	1262	0.61	-0.93	0.80	-0.41	0.84		
	17	36	1-8/8-16/14-36	//3540	//0.95	-1.8/0.90/0.18	0.95/0.88/0.50	-0.72//	0.97//		
	24	7	1-7	1100	0.64	-1.15	0.87	-0.51	0.91		
	30	8	2-8	2345	0.89	-1.1	0.90	-0.49	0.92		
STS-90 KSC 17 April 98 1819 UT 1949 UT	18	3	0-11	105	0.41	-2.4	0.94	-0.98	0.94		
	24	4	0.5-4	480	0.79	-1.7	0.98	-0.73	0.99		
	27	25	1-25(1-6/6-25)	3945(917/13200)	0.56(0.96/0.91)	-1.1(1.9/0.81)	0.71(0.98/0.83)	-0.53(-0.80/-0.45)	0.76(0.98/0.79)		
	30	25	0.3-25(0.3-3)	4750(765/2260)#	0.53(0.60/0.94)#	-1.3(2.2)	0.65(0.98)	-0.61(-0.90/0.74)#	0.72(0.95/0.84)#		
STS-91 KSC 2 June 98 2206 UT 2135 UT	18	50	0-50(0-8/35-50)	4200(920/29600)	0.71(0.92/0.87)	-0.44(1.2/)	0.79(0.94/)	-0.21	0.82		
	24	10	0-10	1730	0.72	-1.5	0.85	-0.66	0.88		
	30	25	0-25	9010	0.92	-0.88	0.85	-0.42	0.87		

\*LT = Launch Time; EST = UT - 5 and EDT = UT - 4; PST = UT - 8 and PDT = UT - 7 \*\*Pursima Hills data only #0-10/10-25 min

## 6. Generalized Particle Model for a SRM Plume in the Stratosphere

Recently, a unified model was presented for particle size distribution, particle density, and geometrical dispersion for the particles in the exhaust of an SRM plume in the stratosphere. [Beiting, 1997a] New *in situ* measurements of the particle size distribution in the lower stratosphere and the data presented here allow this model to be updated.

Because the data clearly show an increase of expansion rate with altitude, it is desirable to reflect this dependence in the model. However, as noted above, the values for the diffusion parameter,  $b$ , obtained from the data fitting procedure above do not reflect the expansion rate with precision; i.e., the average of the ratios of the diffusion parameter to the expansion rate has a standard deviation of about 60% for both methods of identifying the plume edge. Even in light of this shortcoming, it is the best available model to define the expansion in terms of diffusivity—a concept almost universally used to describe the temporal evolution of atmospheric plumes. Accordingly, we search for a method to define a functional relationship between  $b$  and the expansion rate.

Using Eq. (10) to define this relationship would be a good method to assign a diffusion parameter to each expansion rate if this equation were not transcendental. An alternate method is to use a constant-density criterion to identify the scaling between  $b$  and the expansion rate. This is a reasonable procedure because the  $b$  values for the integral and density edge identification methods are related by a constant factor of 1.75 with a standard deviation of only 13%. Therefore, let the radial distance from the center of the plume at which the particle density falls to some value  $e^{-\alpha}$  define the edge of the plume. Then, using Eq. (7), we have

$$\frac{n(r_e, t)}{n(r=0, t)} = e^{-\frac{r_e}{bt}} = e^{-\alpha} \quad (11)$$

or

$$r_e = \alpha bt, \quad (12)$$

which indicates that the expansion rate,  $r_e$ , is directly proportional to  $b$ . The average value of  $b$  (calculated from values given in Table 4, column 9, east coast values) is 1.3 for the center altitude of 24 km. The corresponding values for altitudes of 18 and 30 km are then scaled from the expansion rates given in Table 3, column 3. Accordingly,  $b$  can be expressed as

$$b(z) = 0.85 + 0.079(z - 18) \quad (13)$$

where  $b(z)$  is in m/s,  $z$  is the altitude in km, and the expression is valid for altitudes between 18 and 30 km.

Collecting data from several sources, the particle size distribution of the alumina particles from SRM exhaust in the stratosphere was found to be trimodal. [Beiting, 1997a] This trimodal distribution was recently verified by WB-57 flights in the lower stratosphere (18.5 km). [Ross *et al.*, 1999] Although the geometrical mean diameters of the three modes are in general agreement, the mass fraction in the smallest particle mode differs significantly between the two sets of measurements. The reason for this difference is not known, indicating that additional measurements are warranted. Accordingly, the generalized model for the stratospheric plume particle is presented in two forms, the first using the previous particle distribution, and the second using the most recently measured particle distribution. The model with the original particle size distribution is\*:

$$n_D(D, r, z, t) = \left( \frac{t_n}{t} \right)^2 \exp \left( -\frac{r}{b(z)t} \right) \sum_{i=1}^3 n_i e^{-\gamma_i D}, \quad (14)$$

where

$$n_1 = 8.3 \times 10^{12} \text{ m}^{-3} \mu\text{m}^{-1} \quad \gamma_1 = 63.3 \text{ } (\mu\text{m}^{-1})$$

$$n_2 = 1.8 \times 10^8 \text{ m}^{-3} \mu\text{m}^{-1} \quad \gamma_2 = 3.13 \text{ } (\mu\text{m}^{-1})$$

$$n_3 = 3.3 \times 10^7 \text{ m}^{-3} \mu\text{m}^{-1} \quad \gamma_3 = 0.80 \text{ } (\mu\text{m}^{-1})$$

Using the distribution from Ross *et al.* [1999], the model becomes:\*\*

$$n_D(D, r, z, t) = \left( \frac{t_n}{t} \right)^2 \exp \left( -\frac{r}{b(z)t} \right) \sum_{i=1}^3 n_i e^{-(D-\delta_0)^2/\sigma^2}, \quad (15)$$

where

$$n_1 = 4.3 \times 10^{11} \text{ m}^{-3} \mu\text{m}^{-1} \quad \delta_1 = 0.005 \text{ } (\mu\text{m}^{-1}) \quad \sigma_1 = 0.006 \text{ } (\mu\text{m}^{-1})$$

---

\*The absolute number density of particles at a given time is required to normalize the model. The normalization used here is for a Titan IV vehicle. As discussed in Appendix A of [Beiting, 1997a], normalization requires a spatial average over the exponential factor to the summation in Eq. (14). This average is a function of the diameter over which the plume is spatially averaged. The spatial average of the factor  $\exp[-r/b(z)t]$  yields a factor  $\alpha/(1-e^{-\alpha})$  that multiplies the  $n_i$  coefficients. The  $n_i$  coefficients given above were calculated for  $\alpha = 2$ , where the spatial average was taken to a radius where the centerline density drops to a value of  $e^{-\alpha}$ . Changing the  $b$  parameter in the model does not affect the normalization procedure.

\*\*The parameters given by Ross *et al.* imply an absolute particle density at an unspecified time. Since no absolute density of the aggregate plume was measured, only relative density among the three modes was used, and the normalization procedure used for Eq. (14) was also applied to Eq. (15).

$$n_2 = 3.8 \times 10^{10} \text{ m}^{-3} \mu\text{m}^{-1} \quad \delta_2 = 0.090 \text{ } (\mu\text{m}^{-1}) \quad \sigma_1 = 0.090 \text{ } (\mu\text{m}^{-1})$$

$$n_3 = 7.7 \times 10^9 \text{ m}^{-3} \mu\text{m}^{-1} \quad \delta_3 = 2.03 \text{ } (\mu\text{m}^{-1}) \quad \sigma_1 = 1.49 \text{ } (\mu\text{m}^{-1})$$

One should refer to *Beiting* [1997a] for applications of this model.

## 7. Summary

The expansion rates of plumes from nine Space Shuttle and Titan IV vehicles were measured and compared for altitudes throughout the atmosphere. The expansion rates were found to be constant in time but increased with increasing altitude for all measurements made at the eastern test range. The one measurement made at the western test range showed a higher expansion rate at an altitude of 24 km than the rate measured at an altitude of 30 km. There was considerable variability in the magnitude of the expansion rate at a given altitude from launch to launch, but this variation did not correlate with wind speed or shear. Attempts to associate the expansion with a diffusivity were only partially successful; models that allowed the diffusivity to vary with plume size were more successful than a constant diffusivity model. The results presented here will be useful to models that calculate the chemical effects of aircraft and rocket exhaust in the stratosphere.

## References

- Anon., Range Reference Atmosphere, Range Commanders Council, Document 361-383, White Sands, NM, 1983.
- Arfkin, G., *Mathematical Methods for Physicists*, 2<sup>nd</sup> edition, Academic Press, New York, 1970.
- Beiting, E. J., "Solid rocket Motor Exhaust Model for Alumina Particles in the Stratosphere," *J. Spacecraft and Rockets*, 34, 303-310, 1997a.
- Beiting, E. J., "Predicted Optical Characteristics of Solid Rocket Motor Exhaust Model in the Stratosphere," *J. Spacecraft and Rockets*, 34, 311-317, 1997b.
- Beiting, E. J., "Field Instrumentation for Atmospheric Plume and Contrail Measurements," The Aerospace Corp., TR-98(1306)-5, El Segundo, CA, July 1998.
- Beiting, E. J., and Klingberg, R. L., "K-2 Titan IV Stratospheric Plume Dispersion," The Aerospace Corp. TR-97(1306)-1, January, 1997.
- Brady, B. B., L. R. Martin, and V. I. Lang, "Effects of Launch Vehicle Emissions in the Stratosphere," *J. Spacecraft and Rockets*, 34, 774-779, 1997.
- Burke, M. L. and P. F. Zittel, "Laboratory Generation of Free Chlorine from HCl under Stratospheric Afterburning Conditions," *Combust. Flame* 112, 210-220, 1998.
- Cocchiaro, J. E. (ed.), *Environmental Impacts of Launch Vehicles—A Bibliography*, Chemical Propulsion Information Agency (CPIA), The Johns Hopkins University, Columbia, MD, Aug. 1998.
- Coulson, K. L., *Polarization and Intensity of Light in the Atmosphere*, A. Deepak Publishing, Hampton, Virginia, USA, 1988.
- Danilin, M. Yu, "Local Stratospheric Effects of Solid-fueled Rocket Emissions," *Ann. Geophysicae* 11, 828-836 1994.
- Dao, P. D., J. Gelwachs, R. Farley, R. Garner, and P. Soletsky, "LIDAR Stratospheric SRM Exhaust Plume Measurements," 35th AIAA Aerospace Sciences Meeting, Reno, NV, paper AIAA-97-0526, 1997.
- Denison, M. R., J. J. Lamb, W. D. Bjorndahl, E. Y. Wong, and P. D. Lohn., "Solid Rocket Exhaust in the Stratosphere: Plume Diffusion and Chemical Reactions," *J. Spacecraft & Rockets*, 31, 435-442, 1994.
- Gradshteyn, I. S. and I. M. Ryzhik, *Table of Integrals, Series, and Products*, 4<sup>th</sup> edition, Academic Press, New York, p. 316, 1965.



- Hanning-Lee, M. A., B. B. Brady, L. R. Martin, and J. A. Syage, "Ozone Decomposition on Alumina: Implications for Solid Rocket Motor Exhaust," *Geophys. Res. Lett.* 23, 1961-1964, 1996.
- Hoshizaki, H. (Chairman), "Aircraft Wake Microscale Phenomena," Chap 2, pp 60-73, in *The Stratosphere Perturbed by Propulsion Effluents*, edited by G. D. Robinson, H. Hidalgo, and N. Sundararaman (1975). Volume 4 of the CIAP monograph series. U.S. Department of Transportation Rept. No. DOT-TST-75-53. (Available for NTIS as PB249684).
- Joseph, J. H., Z. Levin, Y. Mekler, G. Ohring, and J. Otterman, "Study of Contrails Observed from the ERTS 1 Satellite Imagery," *J. Geophys. Res.*, 80, 366-372, 1975.
- Kruger, B. C., "Ozone Depletion in the Plume of a Solid-fuel Rocket," *Ann. Geophysicae*, 12, 409-416, 1994.
- Molina, M. J., L. T. Molina, R. Zhang, and R. F. Meads, "The Reaction of  $\text{ClONO}_2$  with HCl on Aluminum Oxide," *Geophys. Res. Letts.*, 24, 1619-1622, 1997.
- Roberts, O. F. T., "The Theoretical Scattering of Smoke in a Turbulent Atmosphere," *Proc. Roy. Soc. Ser. A* 104, 640-, 1923.
- Ross, M. N., "Local Impact of Large Solid Rocket Motor Exhaust on the Stratospheric Ozone and Surface Ultraviolet Flux," *J. Spacecraft & Rockets*, 33, 144-153, 1996.
- Ross, M. N., P. D. Whitefield, D. E. Hagen, and A. R. Hopkins, "In-situ measurement of the aerosol size distribution in stratospheric solid rocket motor exhaust plumes," *Geophys. Res. Letts.*, in press, 1999.
- Ross, M. N., J. R. Benbrook, W. R. Sheldon, P. F. Zittel, and D. L. McKenzie, "Observation of Stratospheric Ozone Depletion in Rocket Plumes," *Nature*, 390, 62-65, 1997.
- Stern, A. C., H. C. Wohlers, R. W. Boubel, and W. P. Lowry, *Fundamentals of Air Pollution*, Academic Press, New York, 1973.
- U.S. Government Printing Office, Washington, D.C., 1985.
- Zittel, P.F., "Computer Model Predictions of the Local Effects of Large, Solid-fuel Rocket Motors on Stratospheric Ozone," The Aerospace Corp. TR-94(4231)-9, El Segundo, CA, Sept. 1994.

## Appendix 1—STS-80 Analysis

The STS-80 was launched from Pad 39B of the Kennedy Space Center at 2:55:47 p.m. EST on 19 Nov 96 into partly cloudy skies with moderate haze. The launch was viewed from Camera Site U176L46 of Cape Canaveral Air Station (CCAS), which is 13.5 km south and 4.9 km east of Pad 39B. The locations of Pad 39B and the camera site are shown in Figure 1-1.

There was a 30° change in the azimuth of the cameras from the 17-km altitude position to the 30 km position. This change was required to differentiate these altitudes since there was 3° or less change in elevation among these altitudes.

As seen from Figure 1-2, at launch time just before 3:00 p.m. EST, the scattering angle is between 75° and 80° at stratospheric altitudes, and little contrast enhancement due to polarization would be expected. Viewing the plume at infrared wavelengths resulted in considerable contrast enhancement, which was expected based on previous analysis. [Beiting, 1999]

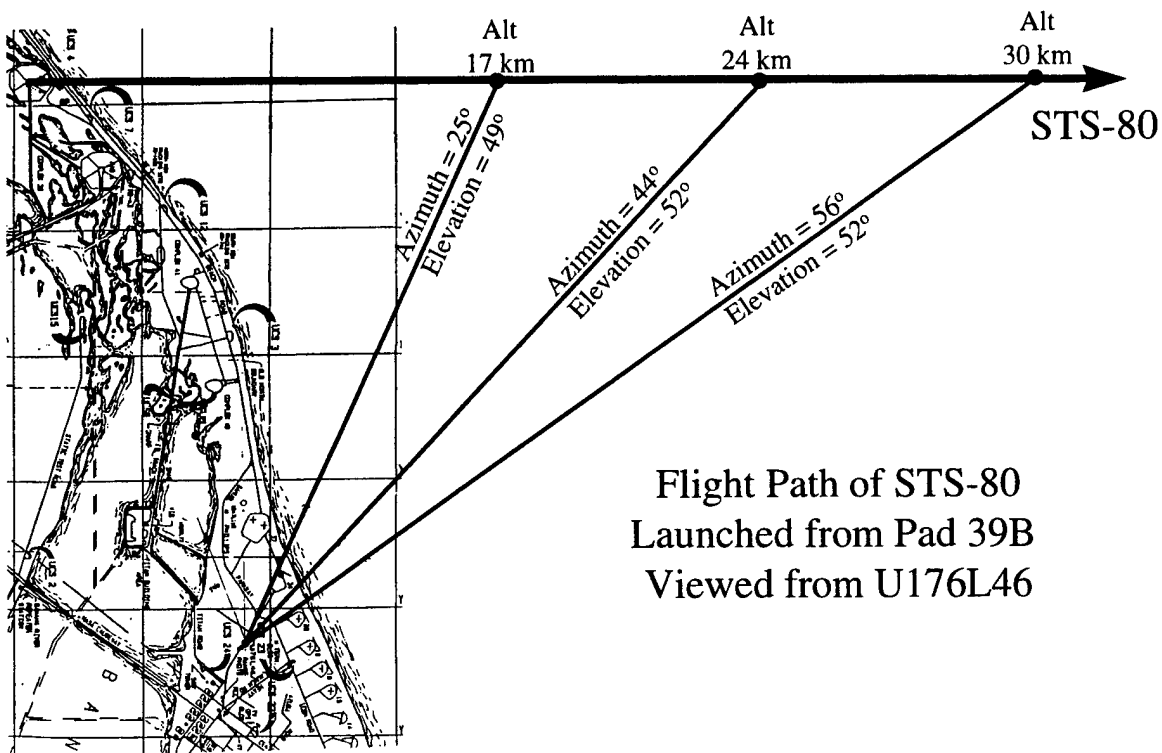


Figure 1-1. Scale map of the launch pad 39B, camera position, ground projection of STS-80 trajectory and viewing vectors at the three altitudes studied.

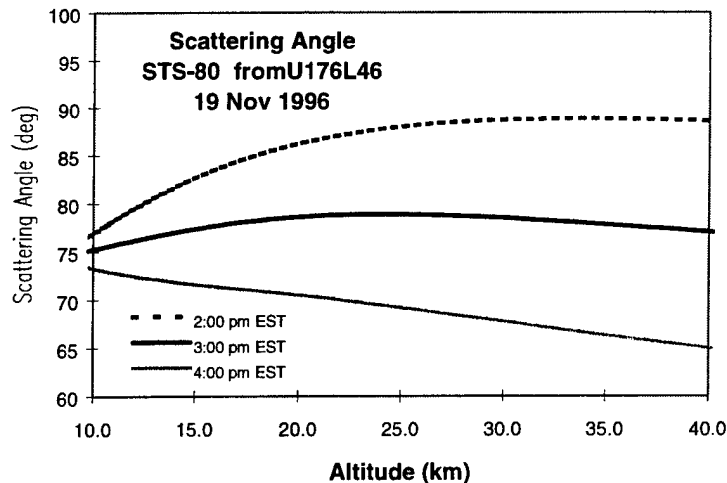


Figure 1-2. Scattering angle of light scattered from the plume for three different times. Launch time was just before 3 p.m.

Rawinsonde balloons were released during the day of the launch and provided stratospheric wind data. Figure 1-3 shows the wind data available closest to the time of vehicle launch. This rawinsonde balloon was released at 16:23 Zulu and reached stratospheric altitudes about an hour later. The STS-80 passed through the stratosphere at 16:56 Zulu, about one-half hour before these wind data were taken. As seen, the wind is predominately from west to east (270°) with a magnitude of 20 m/s (1.2 km/min). Seasonal predictions for the zonal and meridional components of the wind between 17 and 30-km altitude are 6–12 m/s (from west) and 2–3 m/s (from south), respectively, during January. [Anon., 1983]

The instruments and personnel operating the instruments performed flawlessly. Data were acquired at all three altitudes. Unfortunately, the amount of useful data acquired was limited by sections of the lower plume and clouds being blown in front of the upper plume section being studied. The plume observed at 17-km altitude was obscured by the tropospheric plume after about 1 min of expansion, the plume viewed at 24-km altitude was obscured by the tropospheric plume after about 3 min of expansion, and the plume at 30-km altitude was obscured by clouds after 2 min of expansion. Past measurements of the plume expansion indicate a constant expansion rate for the first 10–12 min, and these rates can be compared to the previous measurements. However, these past experiences also show that the expansion rates obtained from linear fits during the first couple of minutes can vary significantly from those obtained over longer times and may not be accurate indicators of the true expansion rate.

The expansion measurements for the three altitudes are shown in Figures 1-4 through 1-6. Two sets of measurements are shown for each altitude. The first series of values of each set was measured from a large (41 cm x 30 cm) monitor, and the second set was taken from laser printer hardcopy of the electronic images (13 cm x 10 cm). Table 1-1 shows the approximate expansion rates obtained from a linear fit to each of the datasets.

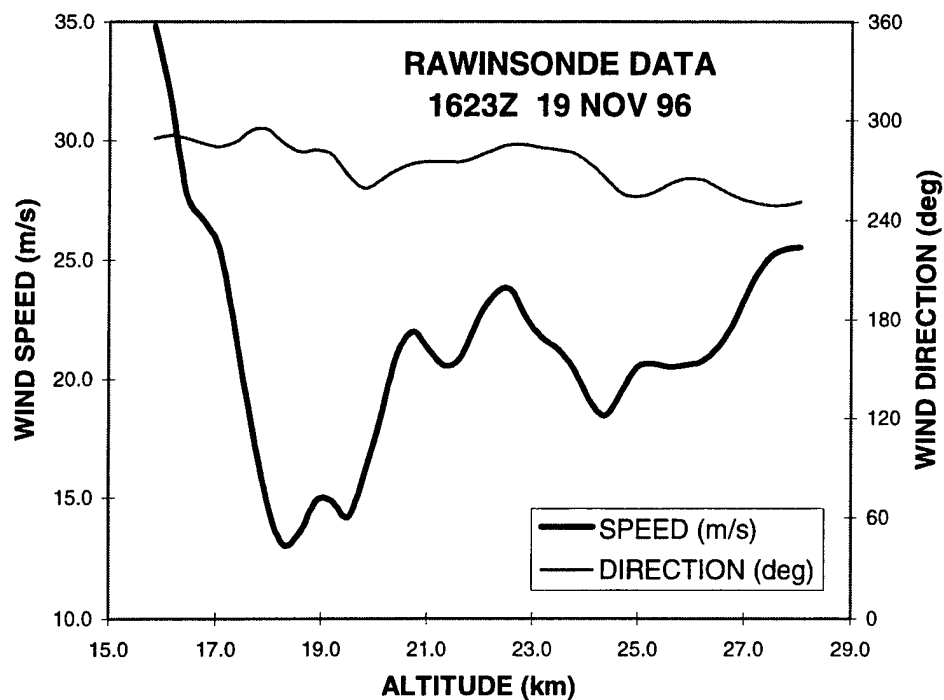


Figure 1-3. Stratospheric rawinsonde wind measurements about 30 min after STS-80 passage.

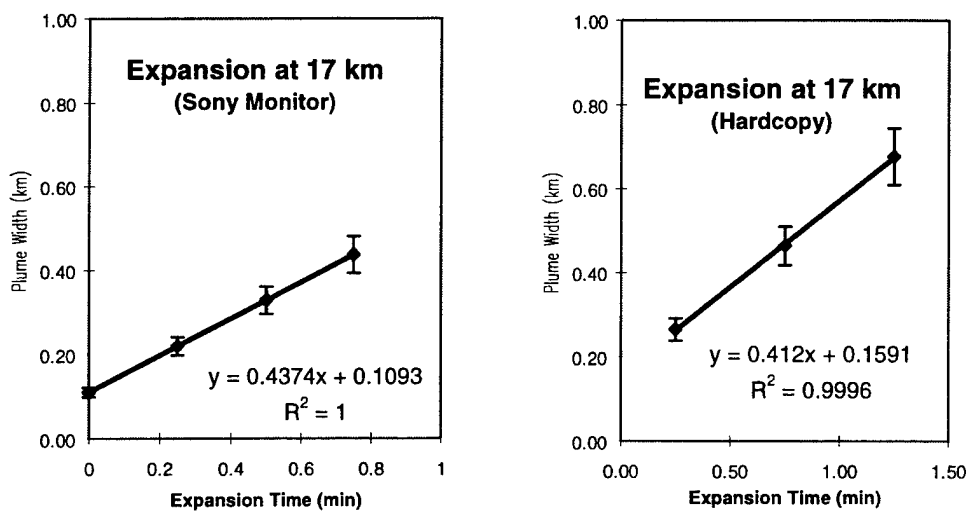


Figure 1-4. Plume width at an altitude of 17 km as a function of expansion time.

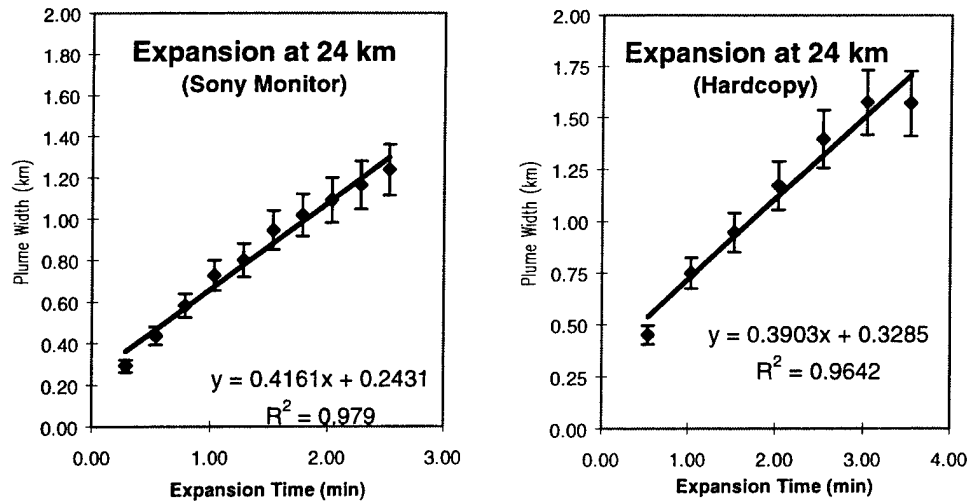


Figure 1-5. Plume width at an altitude of 24 km as a function of expansion time.

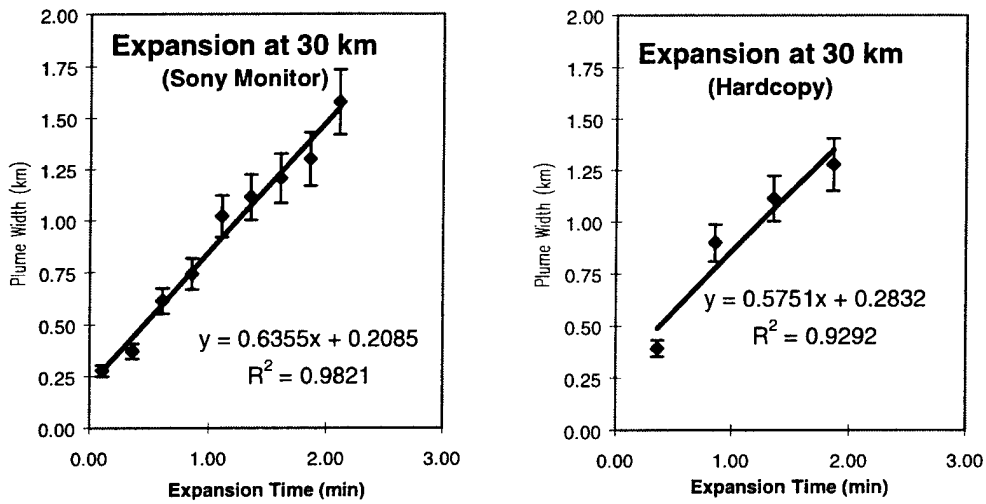


Figure 1-6. Plume width at an altitude of 30 km as a function of expansion time.

Table 1-1. Plume Expansion Rates

Altitude (km)	Sony Monitor (km/min)	Hardcopy (km/min)	Time (min)
17	0.44	0.41	1
24	0.42	0.39	3
30	0.64	0.58	2

As noted above, the day was hazy, and the haze had two effects: it reduced the contrast of the images of the plume and it reduced the polarization of the tropospheric-scattered light. The poor contrast of the plume in the sky was evident when viewed visually; however, the infrared images recorded have considerably better contrast. The contrast of the images of the plume did not improve significantly as a function of polarization angle due to the haze and because of the low scattering angle. [Beiting, 1999]

## Appendix 2—K-13 Analysis

The K-13 was launched from SLC-4E of the Vandenberg Air Force Base at 10:04:00.743 p.m. PST (18:04:00.743 Z) on 20 Dec 96 into mostly clear skies with scattered cirrus clouds. The launch was viewed from a site on the road that parallels the coast on Bixby Ranch south of Jalama Beach (24 and 30 km altitudes) and from the Texaco Harvest oil platform located about 10 km off shore and about 15 km from the ranch site (24-km altitude). The relative positions of SLC-4E and the camera sites are shown in Figure 2-1. The approximate vehicle ground track and the ground projection of the observation line-of-site vectors at the three altitudes studied also are shown to scale in this figure.

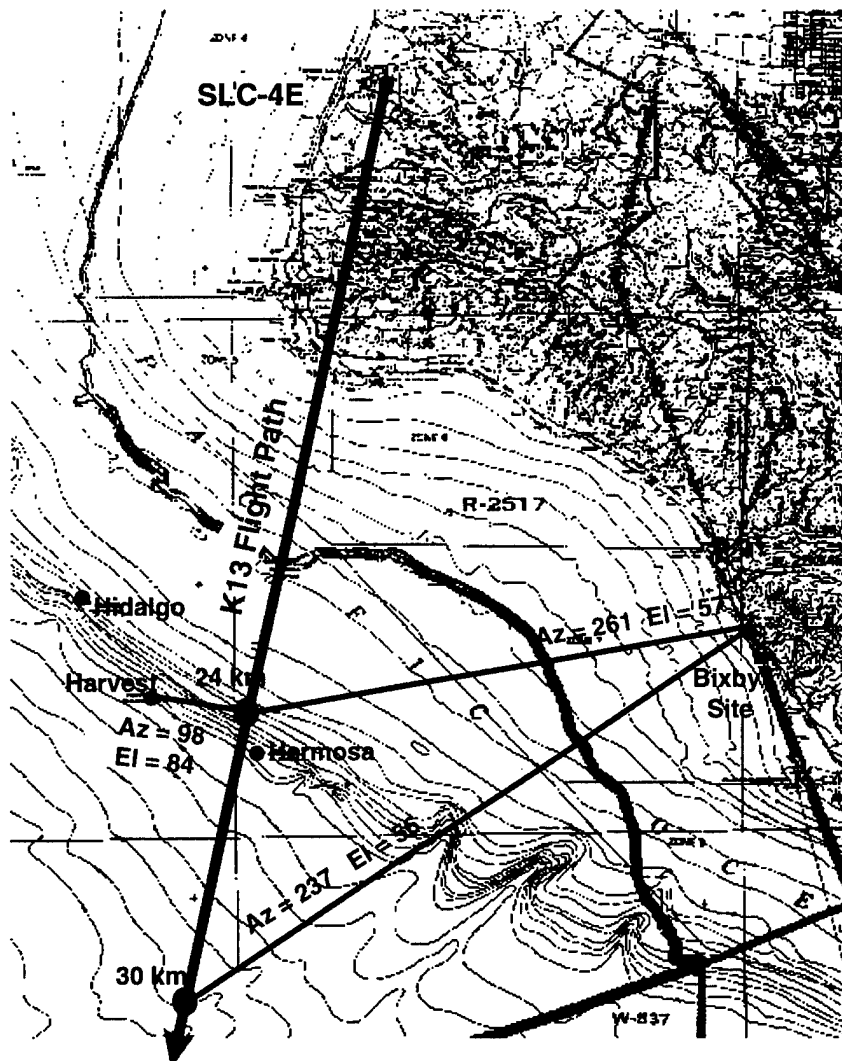


Figure 2-1. Scale map of Vandenberg area showing the launch pad SLC-4E, camera positions on Bixby Road and Harvest Platform, ground projection of K-13 trajectory, and viewing vectors at the two altitudes studied.

The vehicle attained the 24-km altitude at  $T + 85$  s, and the 30-km altitude at  $T + 96$  s. At the Bixby site, there was a  $24^\circ$  change in the azimuth of the cameras from the 24-km altitude position to the 30-km altitude. This change was required to differentiate these altitudes since there was only  $1^\circ$  change in elevation between these altitudes. Tracking the vehicle from the Harvest site was especially challenging because the vehicle was nearly directly overhead (elevation =  $84^\circ$ ) at the assigned altitude of 24 km and the azimuth was changing at a rate of 1.5 deg/s. The distance to and altitude of the vehicle nearly coincide near the assigned altitude indicating that this observation site provided the minimum observation distance to the plume.

The scattering angles of sunlight off the plume in the stratosphere for the two sites are presented in Figures 2-2 and 2-3. At launch time just after 10 a.m. PST, the scattering angle is between  $90^\circ$  and  $110^\circ$  between 24- and 30-km altitude at the Bixby site, which is nearly ideal for contrast enhancement using the polarization method. The scattering angle from the Harvest site at 24-km altitude at 10 a.m. was near  $120^\circ$ —also favorable for image contrast enhancement. Viewing the plume at infrared wavelengths also resulted in considerable contrast enhancement.

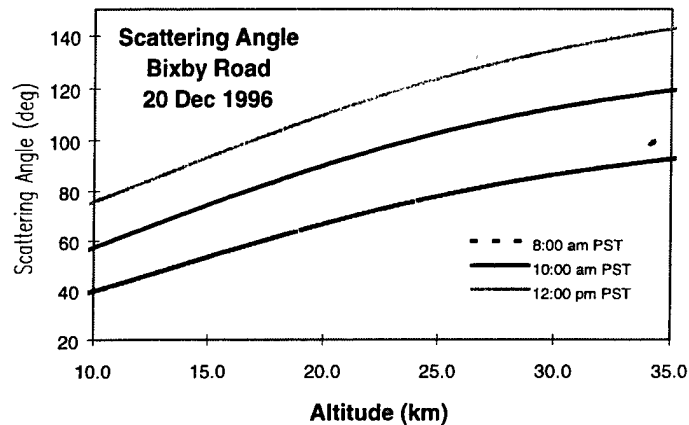


Figure 2-2. Scattering angle of light scattered from the plume for three different times. Launch time was just after 10 a.m.

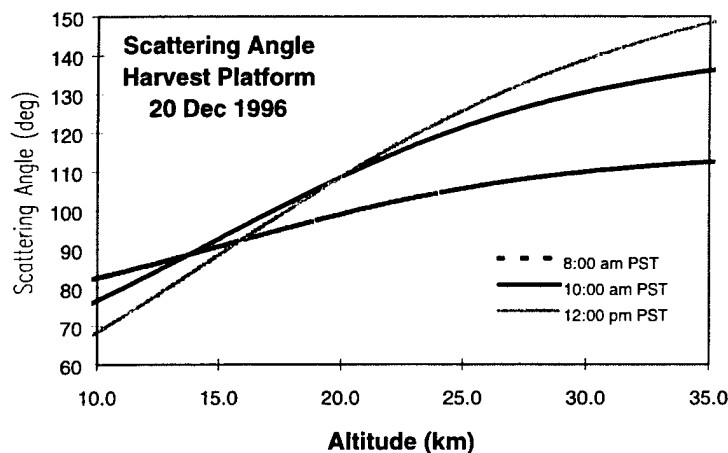


Figure 2-3. Scattering angle of light scattered from the plume for three different times. Launch time was just after 10 a.m.



Rawinsonde balloons were released during the day of the launch and provide stratospheric wind data. Figure 2-4 shows the wind data available closest to the time of vehicle launch. This rawinsonde balloon was released at 17:49 Zulu and rose at 1000 ft/min, reaching stratospheric altitudes about an hour later and bursting at an altitude of 27 km (90,000 ft). The K-18 passed through the stratosphere at 18:05 Zulu, about one-half hour before these wind data were taken. As seen, the wind is predominately from west to east (270°) with a magnitude varying between 5 and 25 m/s (0.3–1.5 km/min).

The motion of the observed plume segment as it expands can be used to measure the wind speed if both the speed and direction of the plume are recorded. The speed of the plume can be obtained by timing the motion of the plume segment on the video screen. The azimuth and elevation of the segment are not recorded so directional information was not available (instrumental upgrades are in progress to record the azimuth and elevation on the video tapes). If we assume a wind direction, the wind speed can be measured. Fortunately, at stratospheric altitudes, the wind has no vertical component and its horizontal component is almost directly from the west (+ zonal) as was confirmed by the rawinsonde. Thus, if we define  $\mathbf{r}$  as the position vector of the plume segment, and  $\mathbf{v}$  as its velocity vector (see Figure 2-5), then noting that the observed component of the velocity is component perpendicular to the position vector, we have

$$\begin{aligned} v_{obs} &= |\hat{\mathbf{r}} \times \vec{\mathbf{v}}| \\ &= \frac{1}{r} \sqrt{(v_x r_z)^2 + (v_x r_y)^2} \end{aligned} \quad (1)$$

where

$$r_y / r = \sin \theta \sin \phi; \quad r_z / r = \cos \theta; \quad \theta = 90 - \theta_{el}; \quad \phi = \text{MOD}_{360}(450^\circ - \theta_{az}),$$

and  $\theta_{el}$  and  $\theta_{az}$  are the azimuth and elevation of the plume segment. Then the fraction of the velocity that is observed assuming a purely westerly wind is

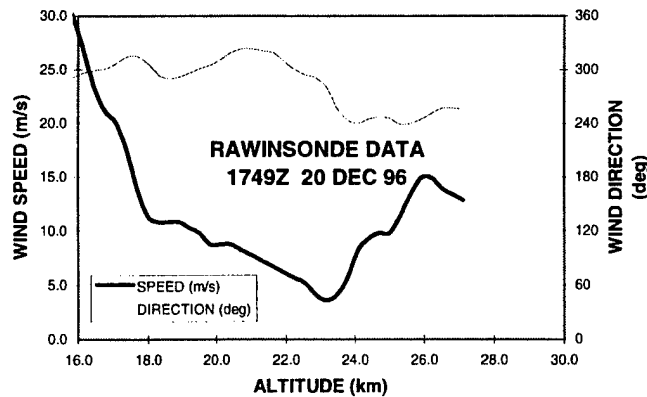


Figure 2-4. Stratospheric rawinsonde wind measurements about 30 min after K-13 passage.

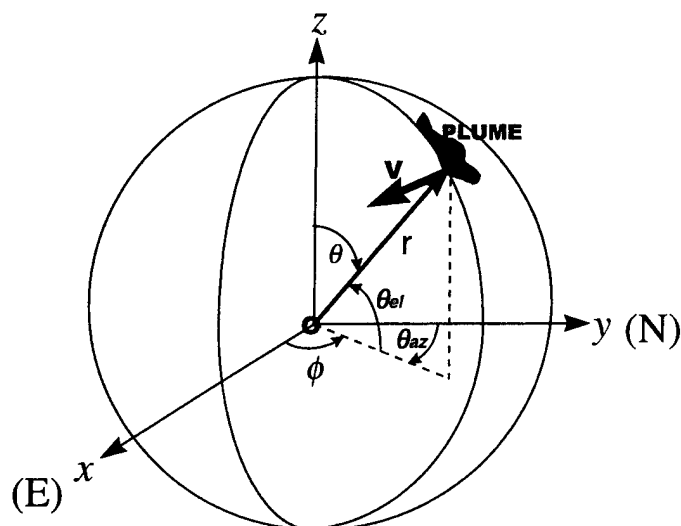


Figure 2-5. Definition of coordinates used to calculate the observed velocity.

$$v_{obs} / v = \sqrt{\cos^2 \theta + \sin^2 \theta \sin^2 \phi}. \quad (2)$$

For the Harvest site, this ratio is 0.98; for the two Bixby Road cameras, the ratios are 0.88 at 24 km and 0.94 at 30 km.

About 10 min of expansion data were obtained from the 24-km altitude Harvest camera and the 30-km altitude Bixby camera. About 8 min of data were obtained from the 24-km altitude Bixby camera. Expansion data were not obtained beyond these times because sections of the tropospheric plume blew in front of the stratospheric sections studied.

The plume widths as a function of time are presented graphically in Figures 2-6 to 2-8. Adjacent sections of the plume at the 24-km altitude position showed different diameters; these diameters were measured separately and are displayed in separate graphs. The narrow and wide sections of the plume did not yield significantly different expansion rates at the Bixby Road site but the narrow section measured from the Harvest Platform was about 20% smaller than its wide rate and of the rate measured at the Bixby Road site. Only one rate was observed at the 30-km altitude plume segment. The second and third columns of Table 2-1 show the expansion rates obtained from linear fits to the datasets.

Table 2-1. Plume Expansion Rates (km/min)

Altitude (km)	K-13 Harvest	K-13 Bixby Road	Observation Time (min)
17	--		
24	0.44-0.52	0.50-0.51	10/8
30	--	0.31	10

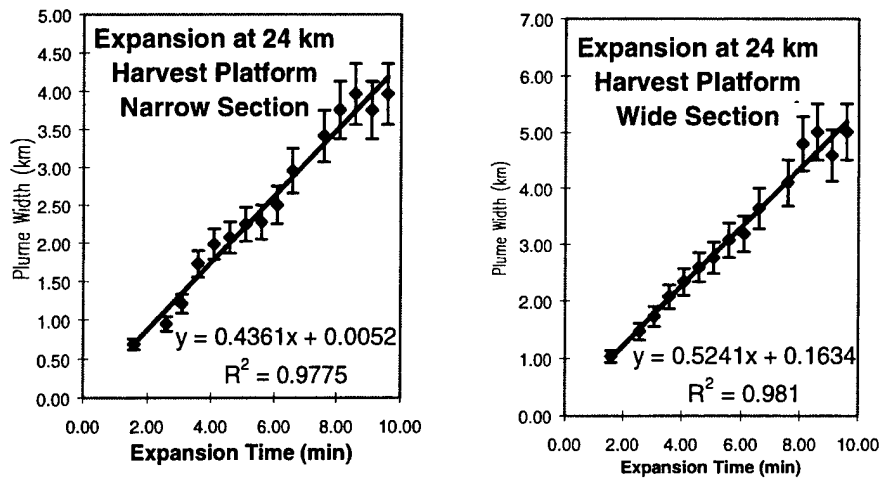


Figure 2-6. Plume width at an altitude of 24 km from Harvest as a function of expansion time.

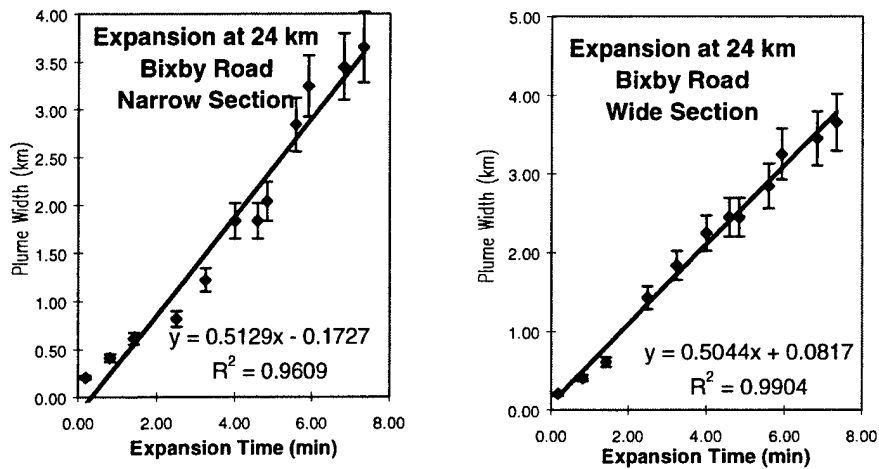


Figure 2-7. Plume width at an altitude of 24 km as a function of expansion time.

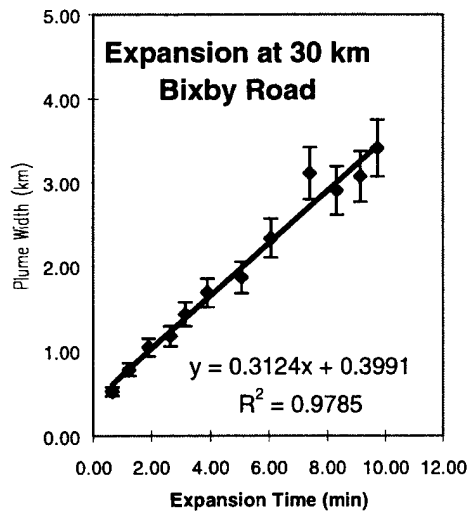


Figure 2-8. Plume width at an altitude of 30 km as a function of expansion time.

The analyses of the measured drift rates are shown in Table 2-2. The geometric factors calculated using Eq. (2) (which are the ratios of the observed-to-true wind speeds assuming a purely westerly horizontal wind direction) do not vary greatly for the three cameras. The velocities shown are for approximately the maximum drift rates observed on the screen. The bulk plume motion at times could appear to be stationary. The velocities shown in the table do vary significantly, and this variation appears surprising for the two sites measuring the same altitude. However, this is not inconsistent with the rawinsonde data shown in Figure 2-4. There is a large wind shear for the altitudes near 24 km, the wind speed varying between 3.6 m/s and 14.9 m/s for the altitudes between 23 and 26 km. Thus, an error in the observed altitude of just  $\pm 1$  km would explain the difference in inferred wind speeds. The rawinsonde data did not measure the wind speed at 30 km. Measurements of wind velocity by the observing plume motion are useful but quantitatively approximate.

The principal reason for selecting two sites to view the same altitude was to gain an understanding of the three-dimensional plume morphology from the two-dimensional images. The Harvest site was fortuitously positioned to allow a view nearly perpendicular to the view given by the Bixby Road site. Selected images of the plume from both sites are shown below in this appendix. In these images, the Harvest Platform is 24.15 km from the 24 altitude plume segment (indicating that the platform is nearly directly under the trajectory at this altitude, as can be seen in Figure 2-1), and the Bixby site is 28.5 km from the 24-km altitude segment. For the images taken with the camera lens set at a focal length of 20 mm, the  $16.5^\circ \times 12.5^\circ$  field-of-view yields an image size of approximately  $5 \times 7$  km and an altitude range of 23.7 to 24.5 from Harvest and an image size of about  $6 \times 8$  km and an altitude range of 22 to 25.5 km from Bixby Road. The lower segment of the plume appears on the right in the Bixby Road images and on the left on the Harvest images. The vehicle required 85 s to reach the 24-km altitude so 1.4 min should be subtracted from the T+ times indicated on the figures to obtain the expansion time (i.e. the first image shows an expansion time of 1.6 min.). At later times, the lower tropospheric section of the plume is seen blowing in front of the 24-km altitude segment of the plume. The 24-km altitude position is marked in each of these images, as are corresponding segments of the plume. These images show that although individual segments of the plume are shearing from each other and the expansion of the narrower section of the plume is slightly (20%) asymmetrical, in general, however, each segment appears to be expanding more or less symmetrically.

Images of the plume segment at 30 km taken from the Bixby Road site are also presented below in this appendix. The  $16.5^\circ$  horizontal field-of-view of the 20 mm focal length images encompassed the 28 to 33-km altitude range. The time to the 30-km altitude was 96 s, requiring 1.6 min to be subtracted from the T+ times listed to obtain the expansion times. At T + 11 min, a tropospheric section of the plume can be seen to be moving in front of the plume segment under study, precluding further measurements.

Table 2-2. Estimated Wind Velocity from Plume Motion

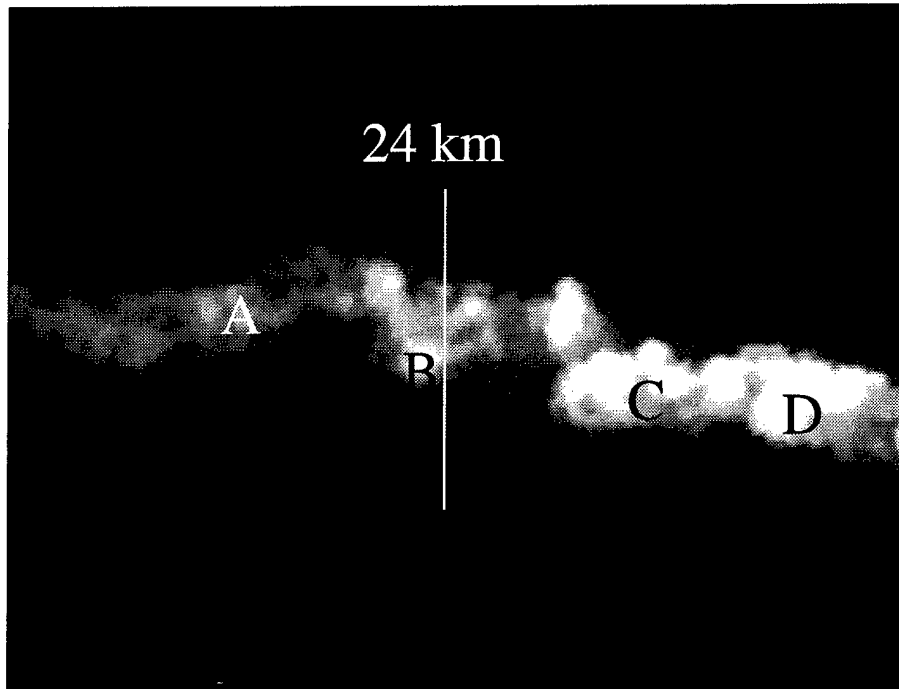
Site	Altitude (km)	Azimuth (deg)	Elevation (deg)	Geometric Factor	Velocity (m/s)
Harvest	24	94	79	0.98	5.4
Bixby Rd	24	258	60	0.88	12
Bixby Rd	30	223	60	0.94	21

The principal results from these measurements are: the plume expansion rate at 24-km altitude was an intermediate value (0.4–0.5 km/min) between previously measured values at 18 km (0.3 km/min.) and 30 km (0.6 km/min.); the plume expansion rate at 30 km (0.3 km/min.) was about half the value of the rates previously measured at the eastern test range; the inferred wind velocity indicated considerable wind shear, an observation consistent with the observed plume morphology; the dual views of the plume indicate that the individual sheared packets of plume expanded symmetrically ( $\pm 20\%$ ).

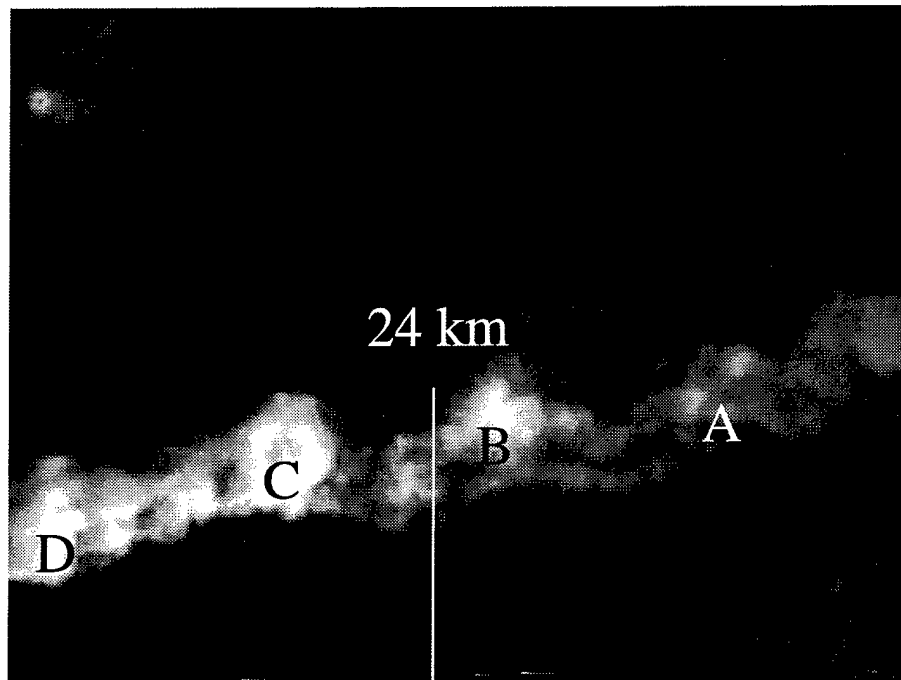
High, wispy cirrus clouds reduced the contrast of the plume images, but the favorable scattering angle from both sites allowed the polarizer to mitigate this effect. Additionally, viewing the images in the near infrared also increased the contrast of the images over visual observations. Consequently, the time interval that expansion was able to be observed was determined not by loss of contrast but by sections of the tropospheric plume blocking view of the stratospheric plume. Light scattered off the camera filters and polarizers into the CCD when the camera lens was set to a short focal length detrimentally affected the quality of the data because the sun was near the edge of the field-of-view.

Orthogonal Views at 24-km Altitude

K13; 24 Km Alt; T+3:00 min

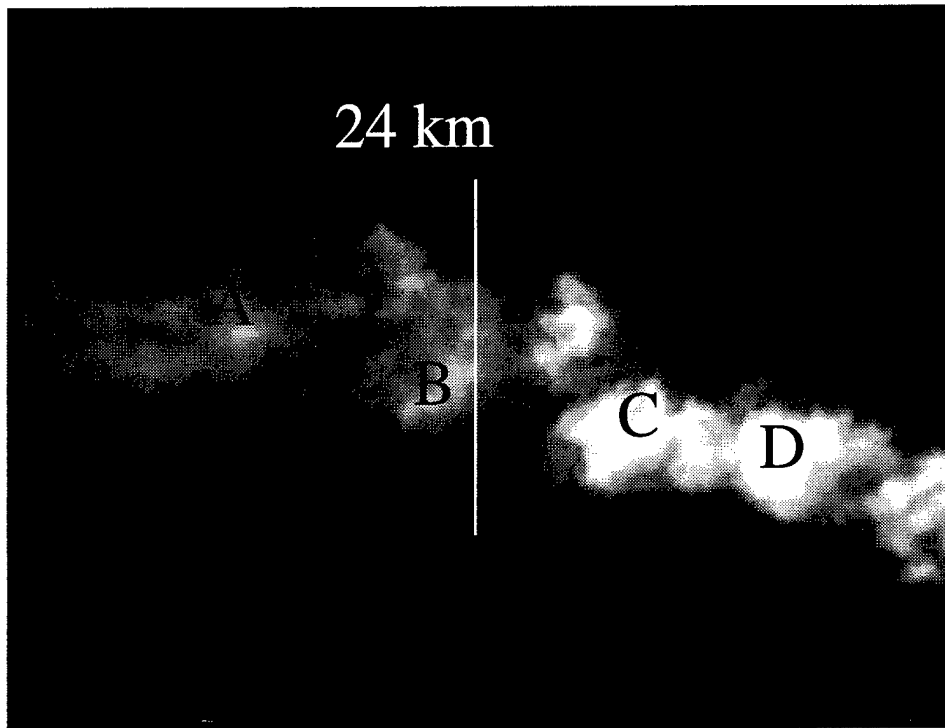


Bixby Road View;  $f = 20$  mm

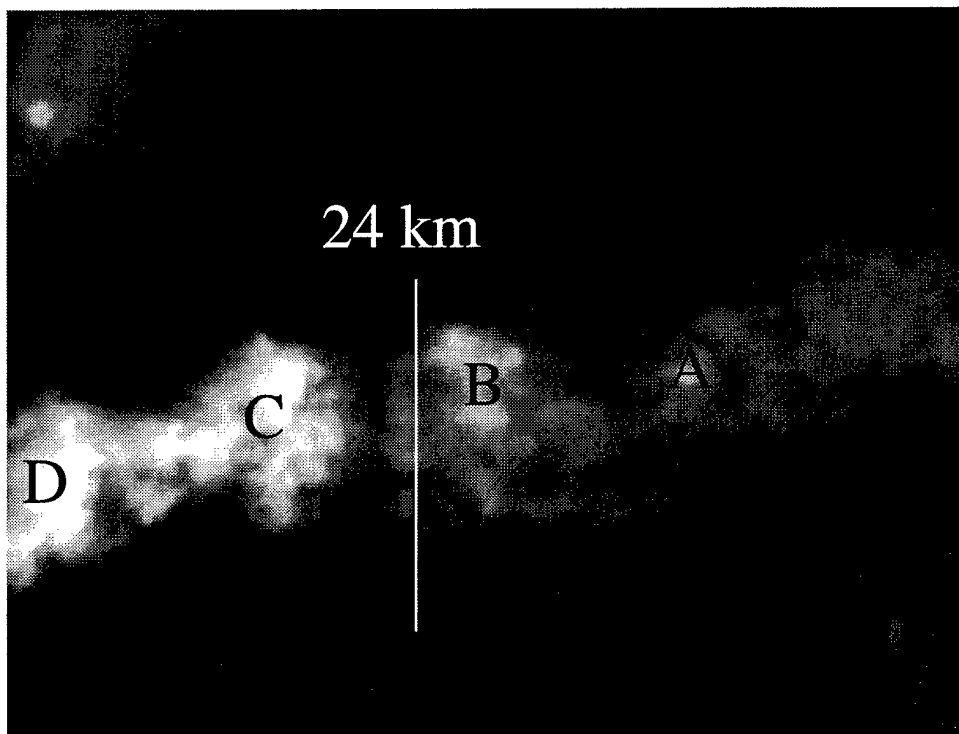


Harvest Platform View ;  $f = 20$  mm

K13; 24 Km Alt; T+4:00 min

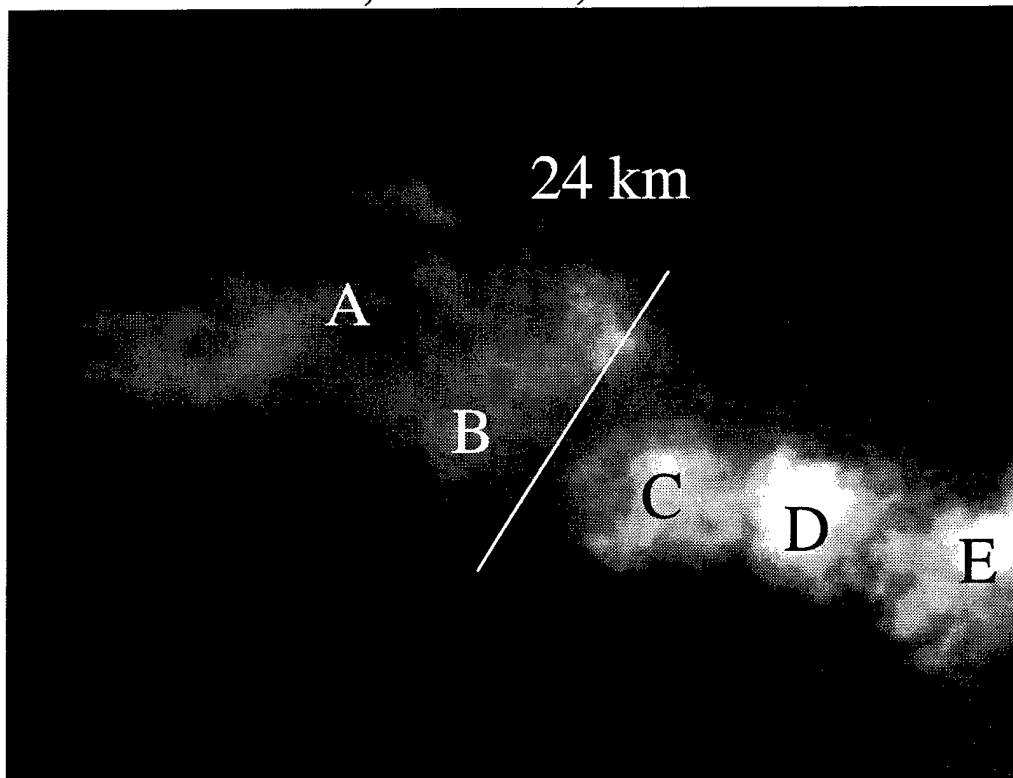


Bixby Road View;  $f = 20$  mm

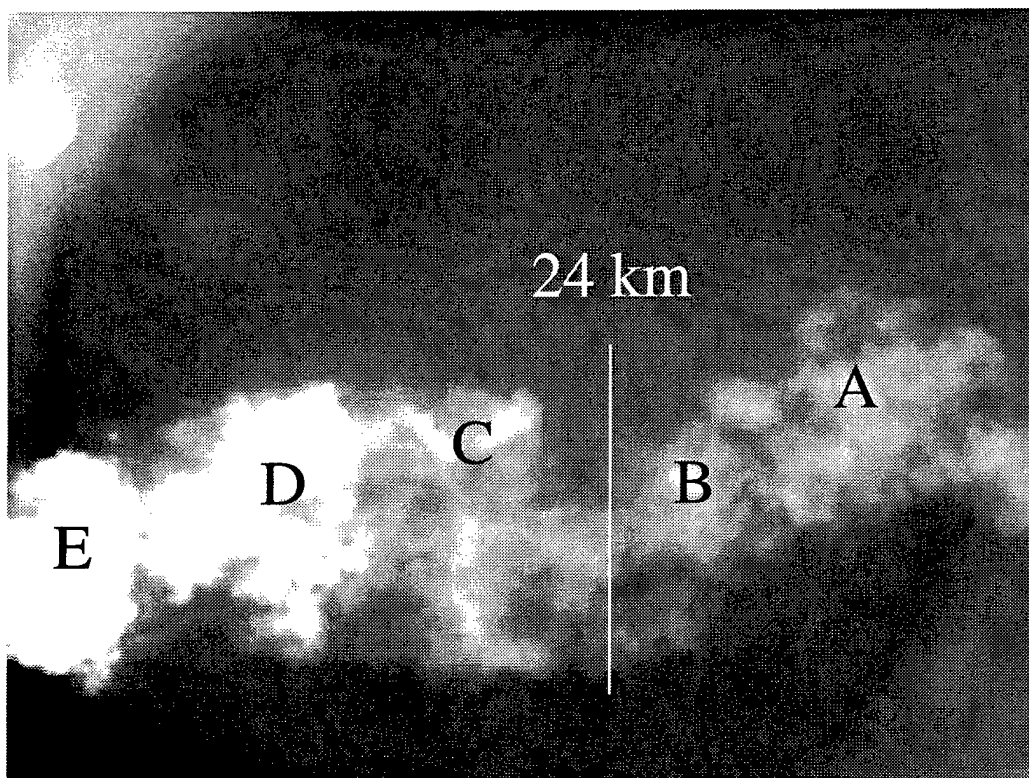


Harvest Platform View;  $f = 20$  mm

K13; 24 Km Alt; T+5:00 min



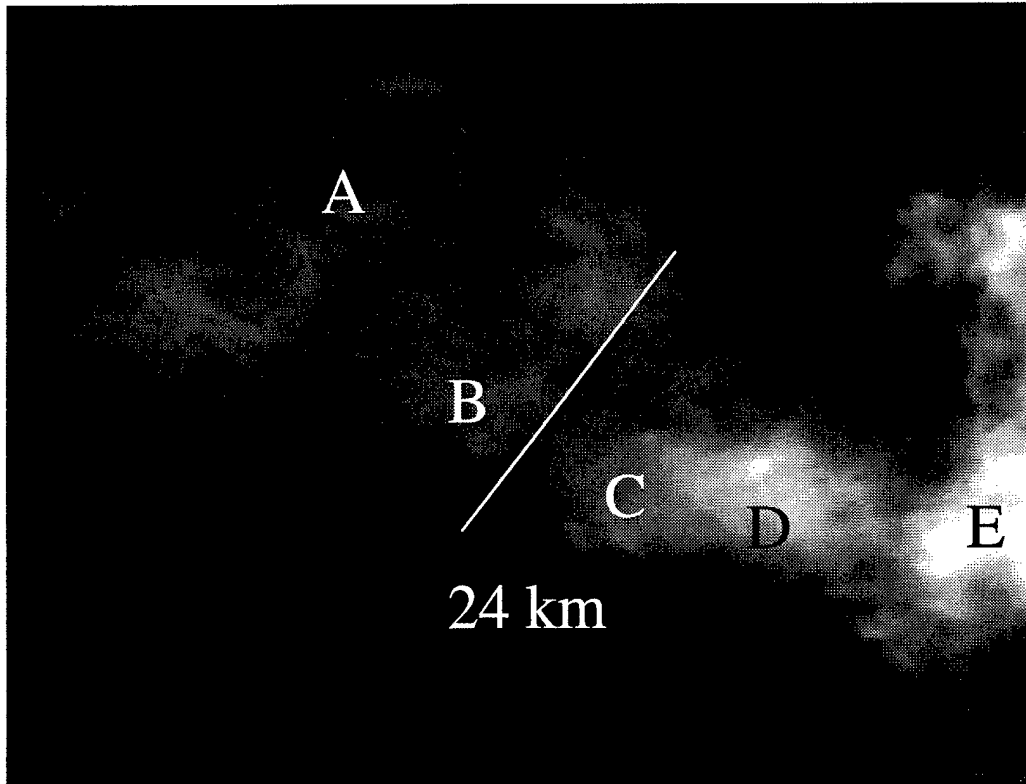
Bixby Road View;  $f=20$  mm



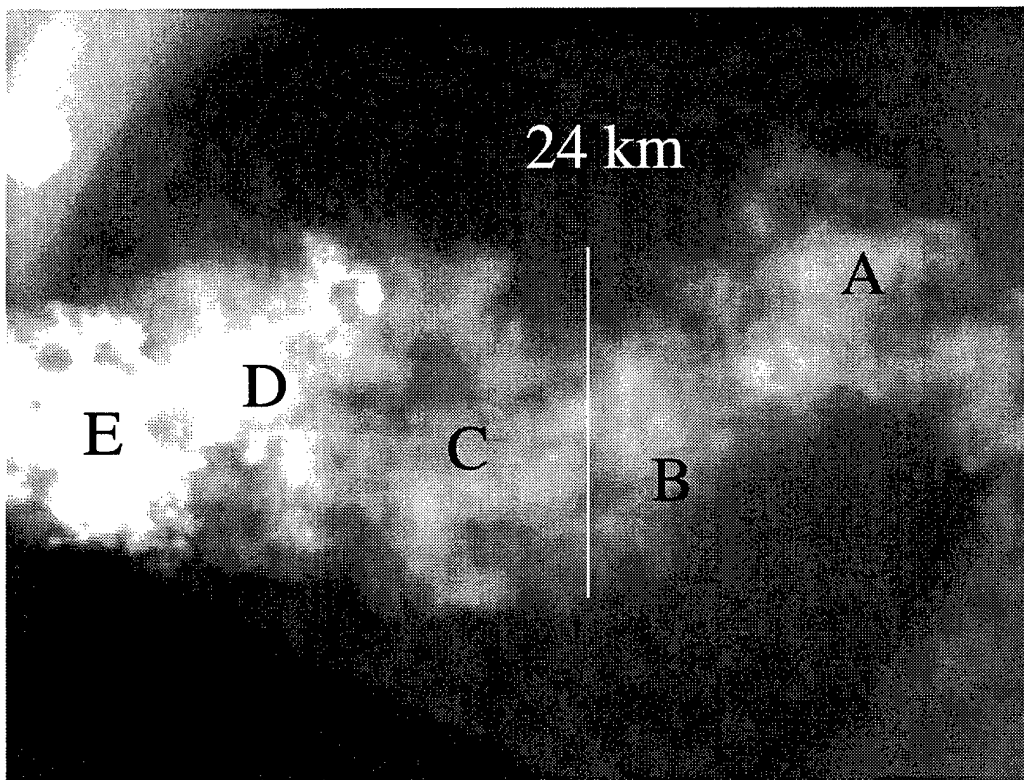
Harvest Platform View ;  $f=20$  mm



**K13; 24 Km Alt; T+6:00 min**

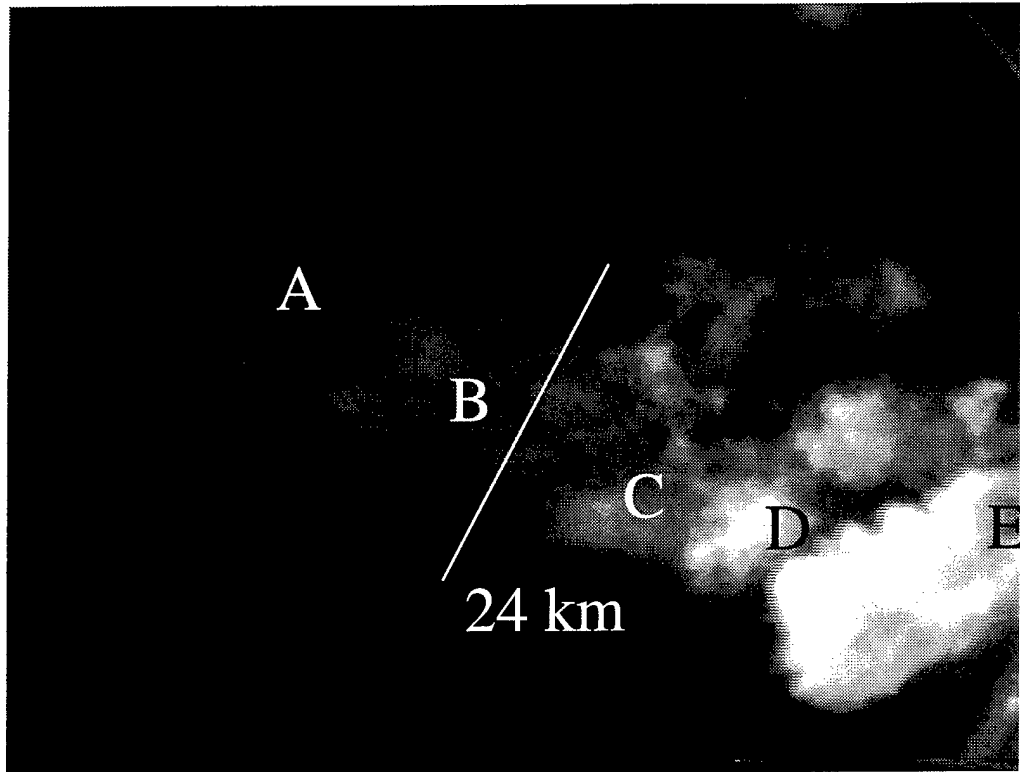


Bixby Road View ;  $f=20$  mm

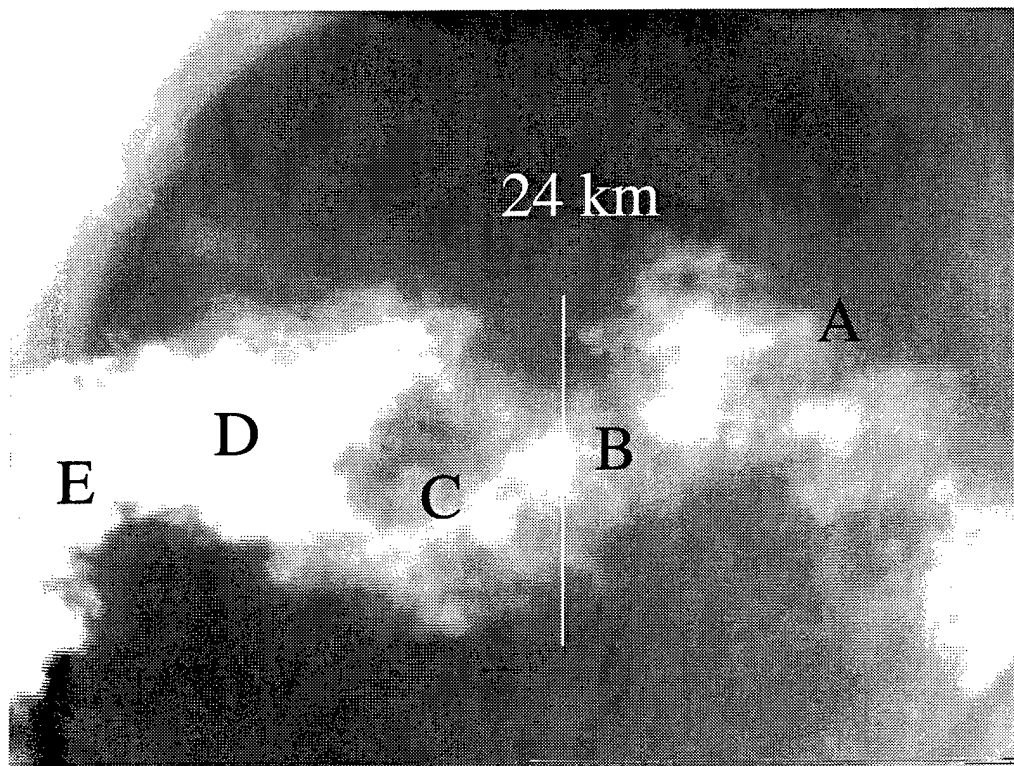


Harvest Platform View ;  $f=20$  mm

K13; 24 Km Alt; T+7:00 min

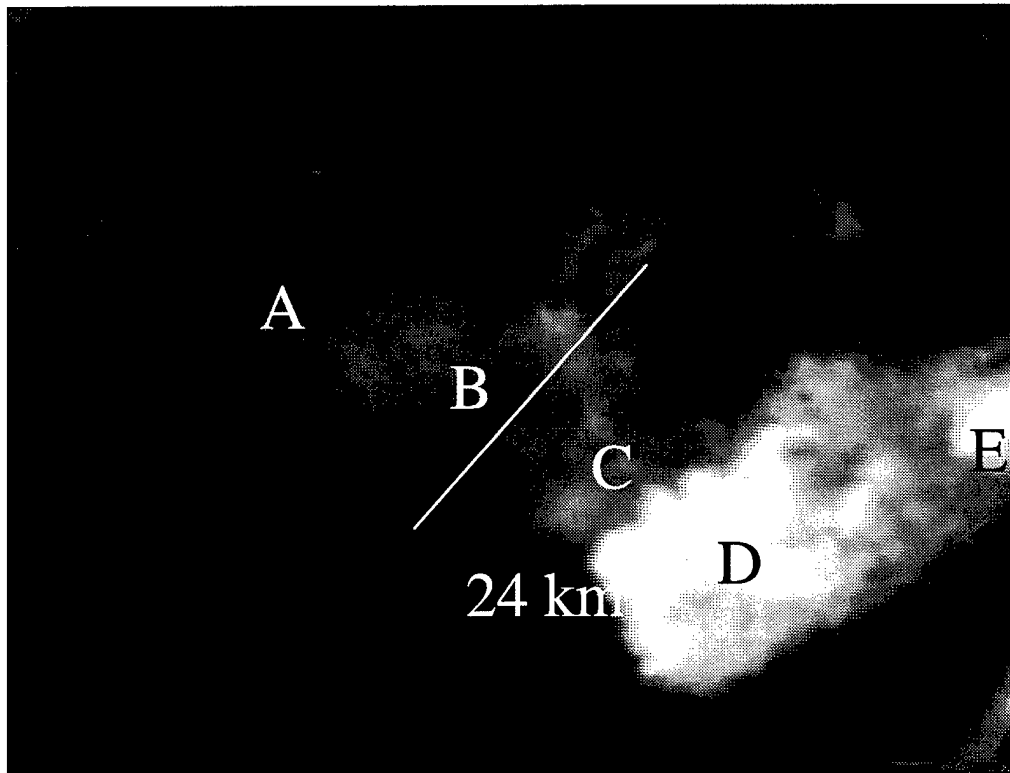


Bixby Road View ;  $f=10$  mm

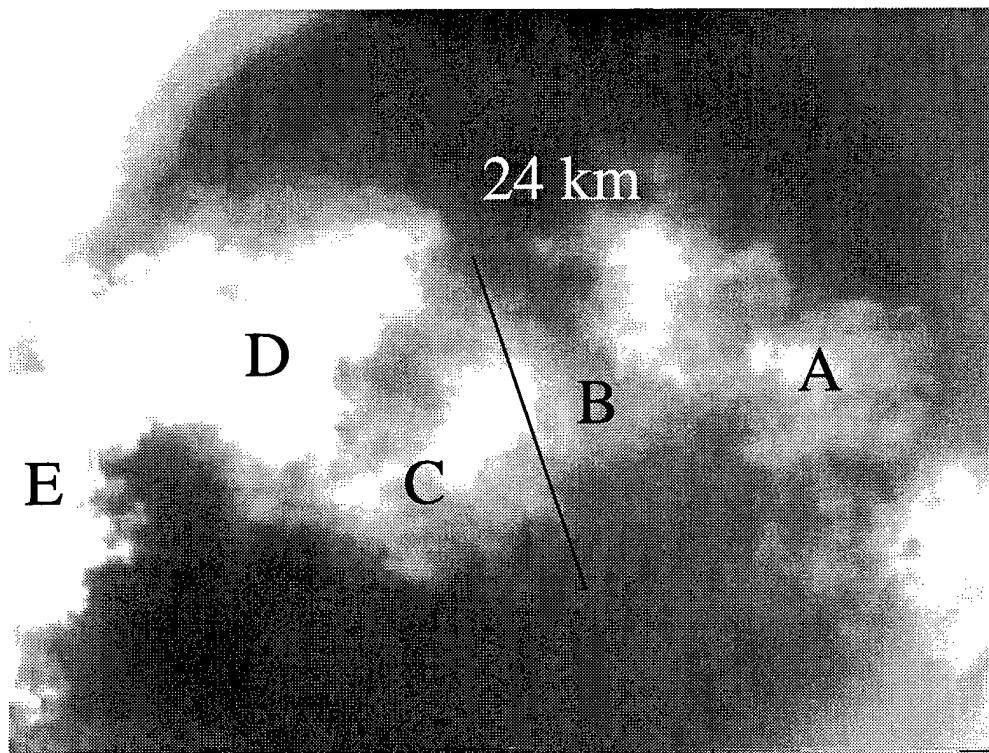


Harvest Platform View ;  $f=15$  mm

**K13; 24 Km Alt; T+8:00 min**

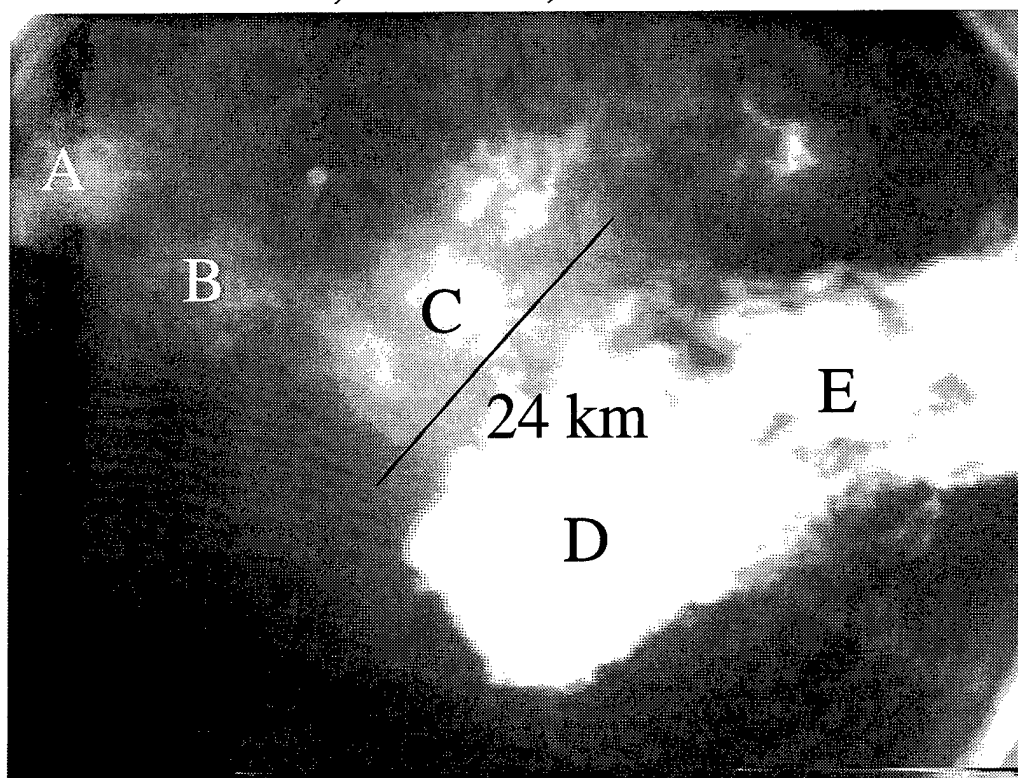


Bixby Road View ; f=10 mm

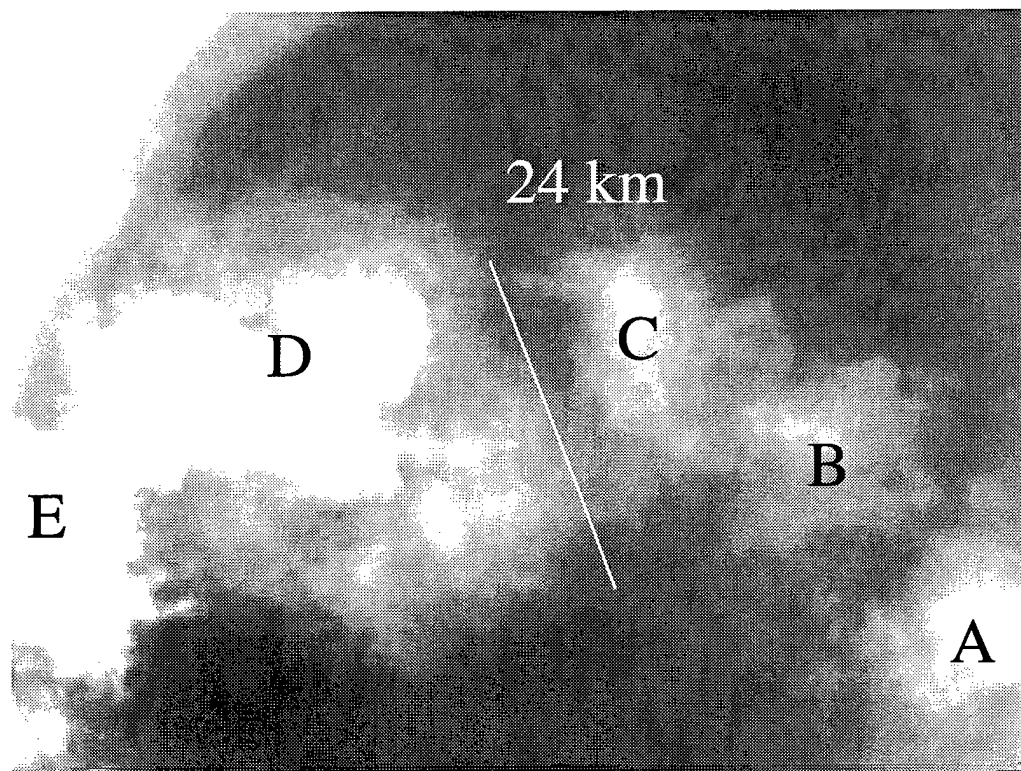


Harvest Platform View ; f=15 mm

K13; 24 Km Alt; T+9:00 min

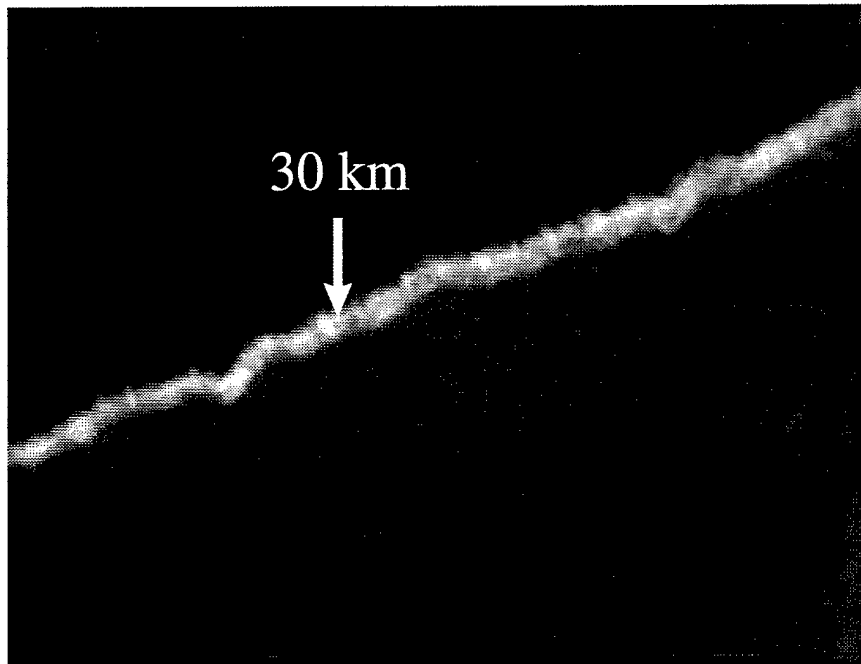


Bixby Road View ;  $f=10$  mm

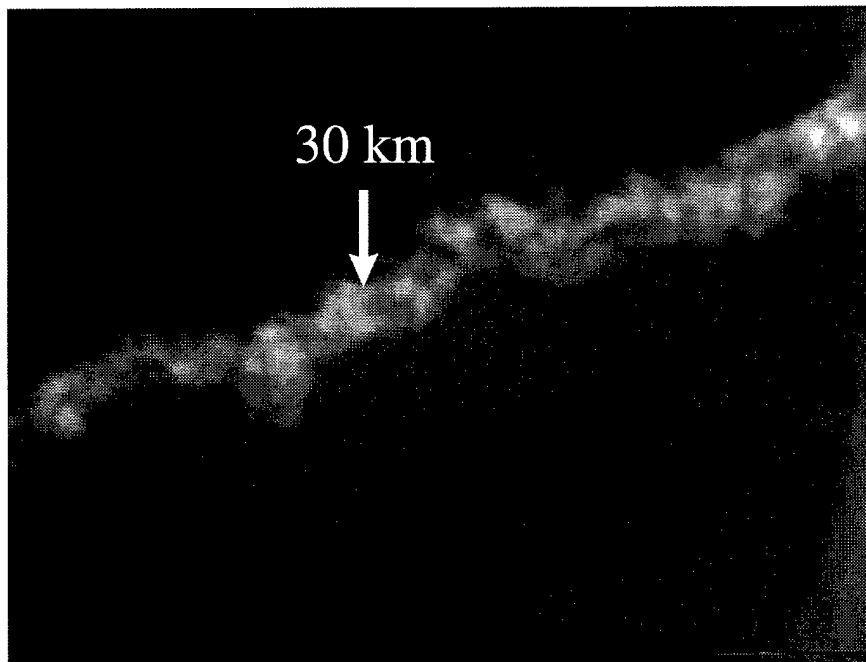


Harvest Platform View ;  $f=15$  mm

Appendix II  
Plume Images at 30-km Altitude  
K13; 30 Km Alt; Bixby Road

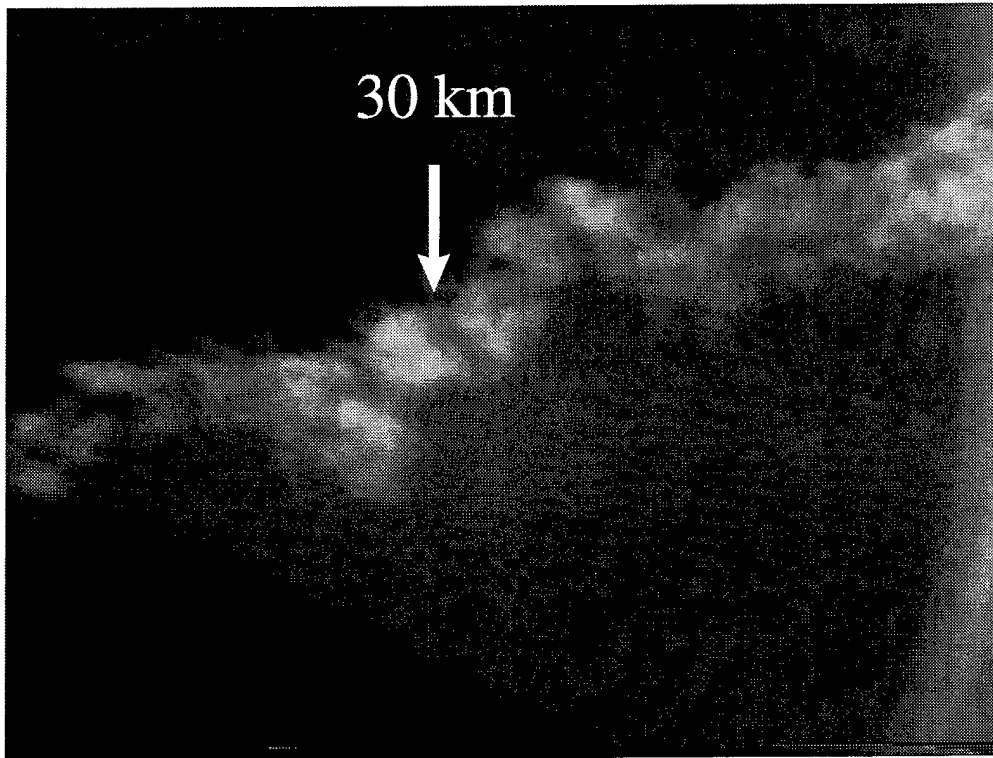


T+2:00 min ; f =20 mm

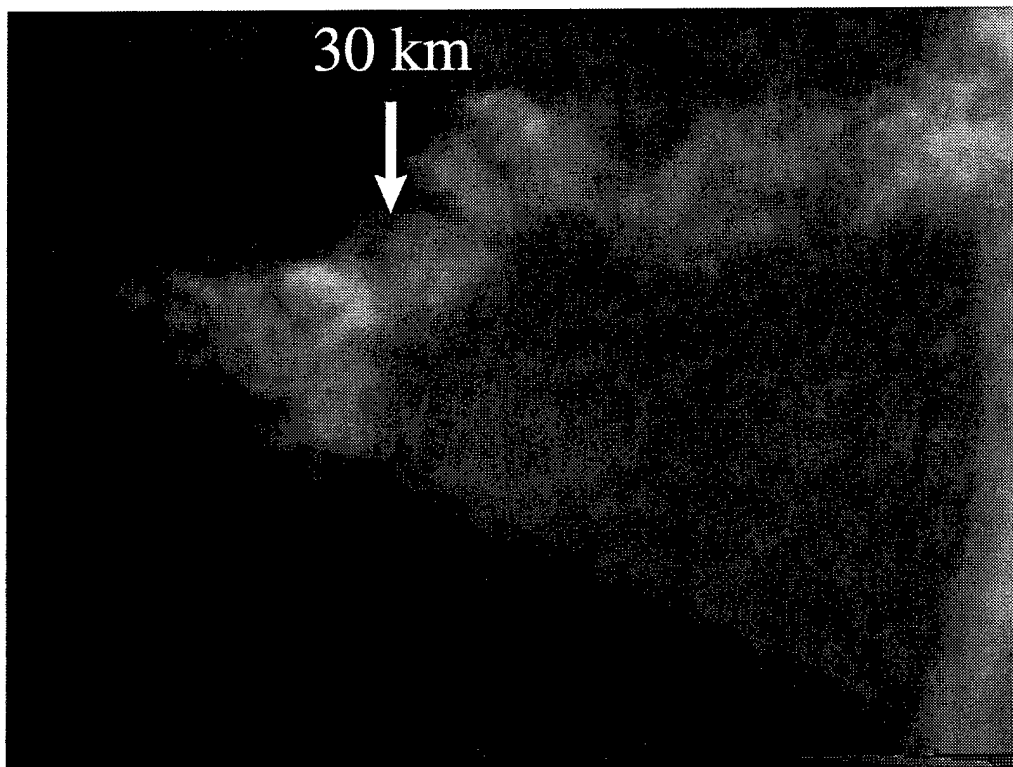


T+3:00 min ; f =20 mm

**K13; 30 Km Alt; Bixby Road**

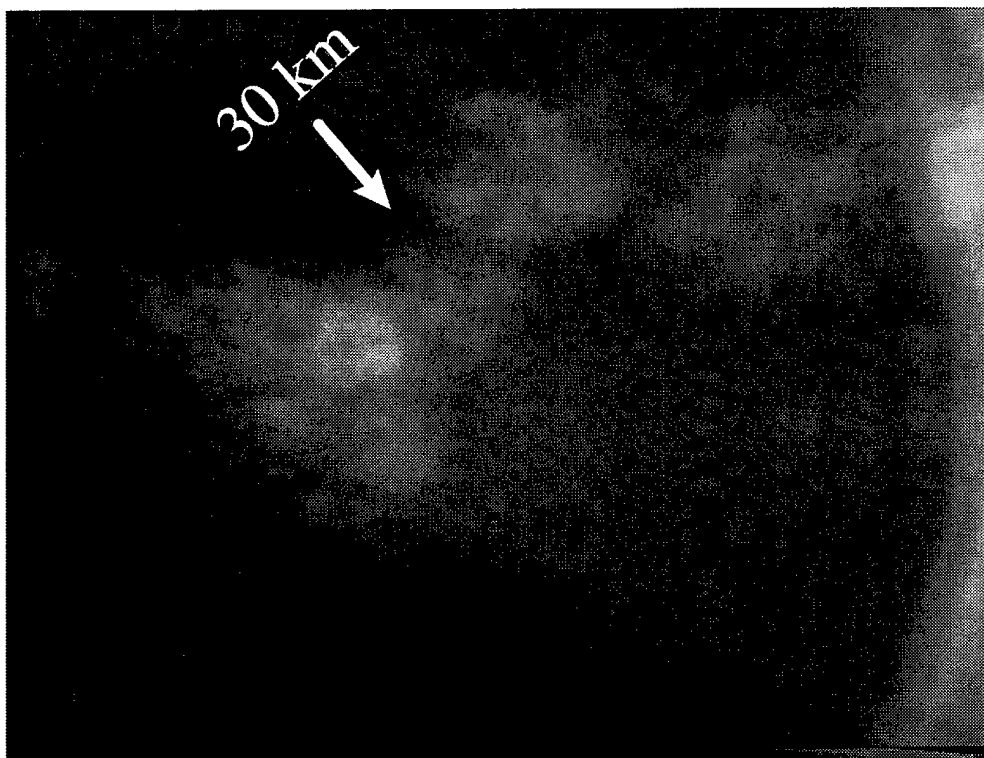


T+:4:00 min ; f =20 mm

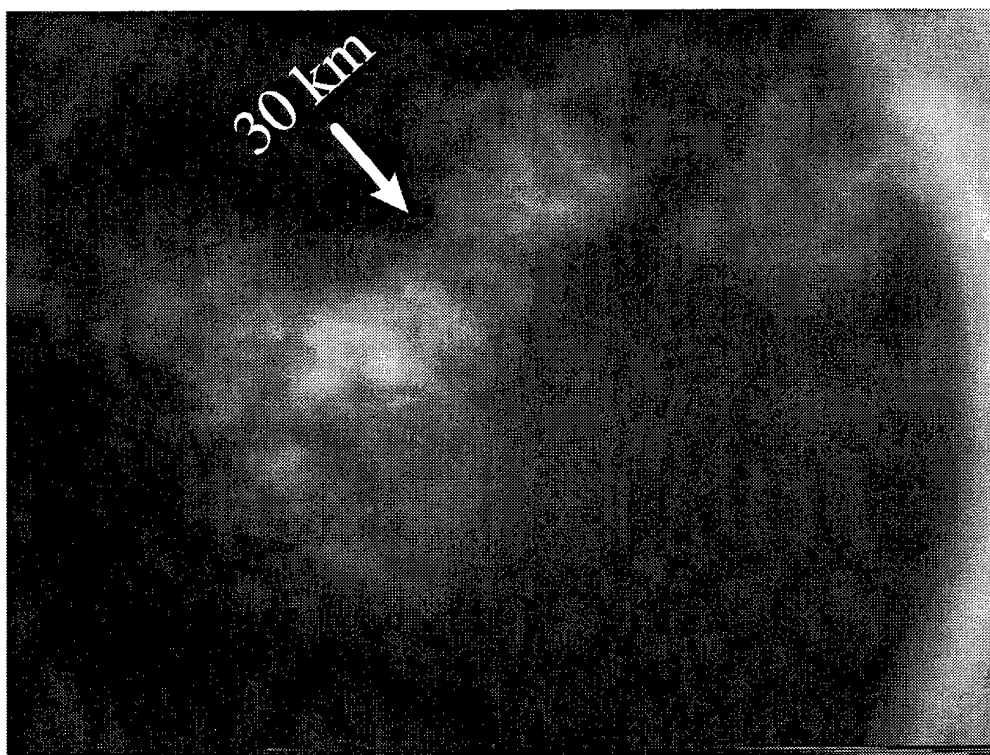


T+5:00 min ; f =20 mm

**K13; 30 Km Alt; Bixby Road**



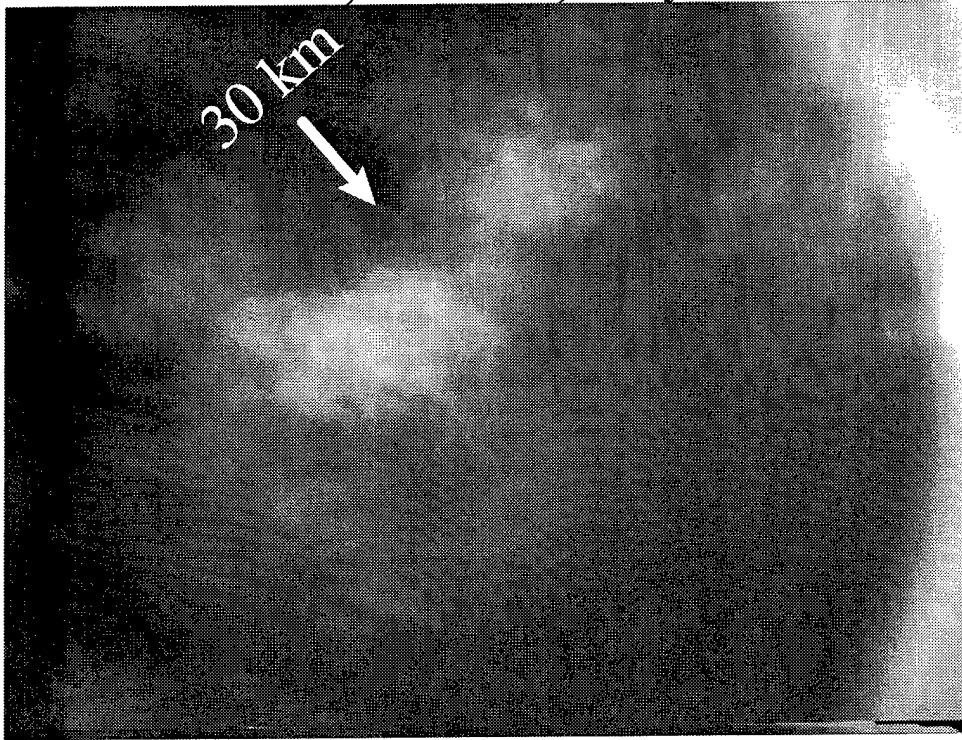
T+:6:00 min ; f =20 mm



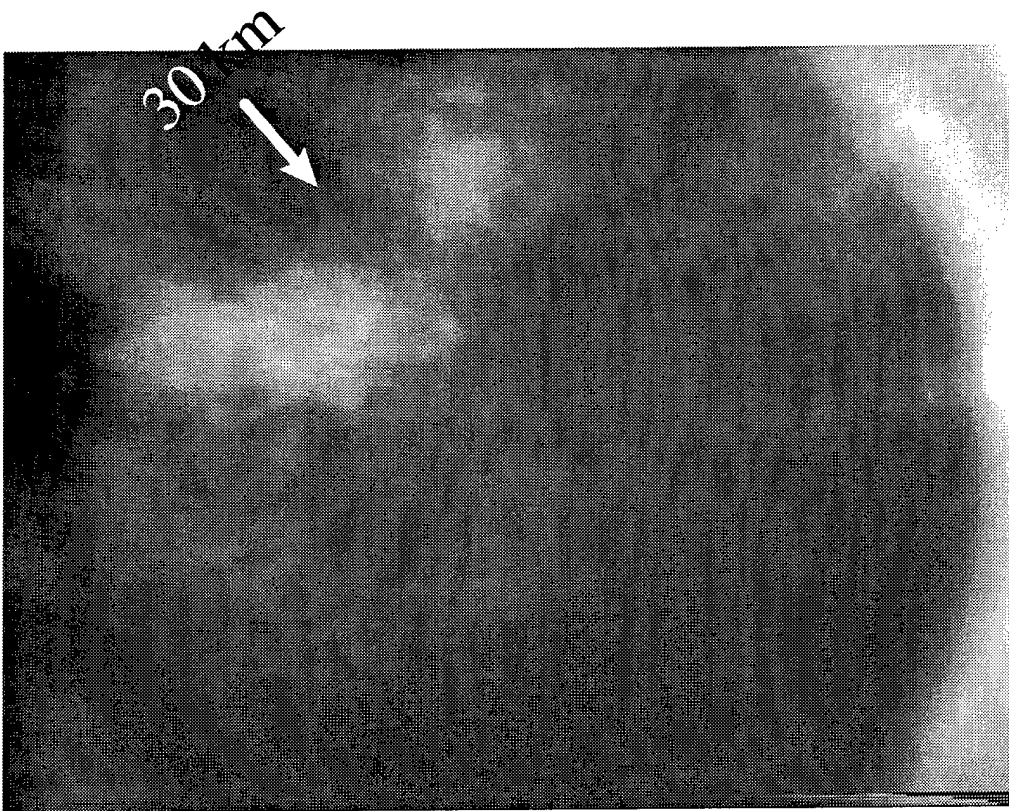
T+7:00 min ; f =20 mm



**K13; 30 Km Alt; Bixby Road**



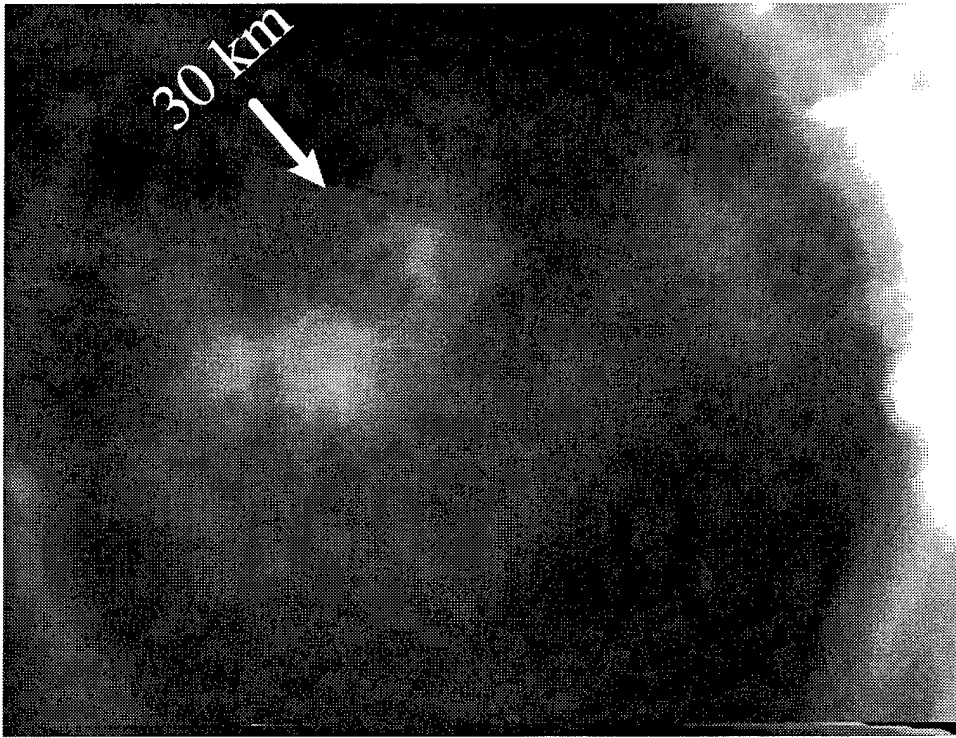
T+:8:00 min ; f =20 mm



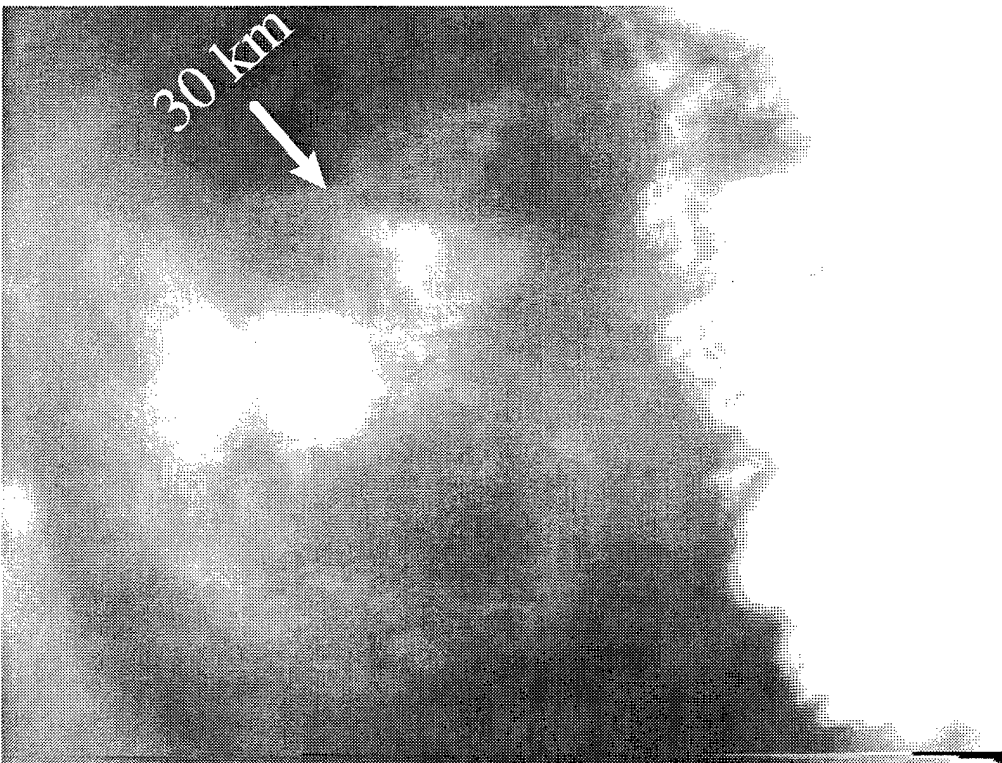
T+9:00 min ; f =20 mm



**K13; 30 Km Alt; Bixby Road**



T+:10:00 min ; f =15 mm



T+11:00 min ; f =15 mm

### Appendix 3—STS-83 Analysis

The STS-83 was launched from Pad 39A of the Kennedy Space Center at 2:20:32.074 p.m. EST on 4 April 97 into partly cloudy skies with moderate haze. The launch was viewed from Camera Site U176L46 of Cape Canaveral Air Station (CCAS) which is 13.3 km south and 3.2 km east of Pad 39A. The location of Pad 39A and the camera site are shown in Figure 3-1.

The approximate vehicle ground track and the ground projection of the observation line-of-site vectors at the three altitudes studied also are shown to scale in Figure 3-1. The vehicle attained the 17-km altitude at T + 76 s, the 24-km altitude at T + 89 s, and the 30-km altitude at T + 99 s. There was a 26° change in the azimuth between the 17-km altitude position and the 30-km altitude position. This change was required to differentiate among these altitudes since there was 2° or less change in elevation among the three altitudes.

The scattering angles of the sunlight off the plume segment studied were calculated and are shown in Figure 3-2 as a function of altitude for three times of day. At launch, just after 2:20 p.m. EST, the scattering angle is between 90° and 110° between 24 km and 30 km altitude, which is nearly ideal for contrast enhancement using the polarization method.

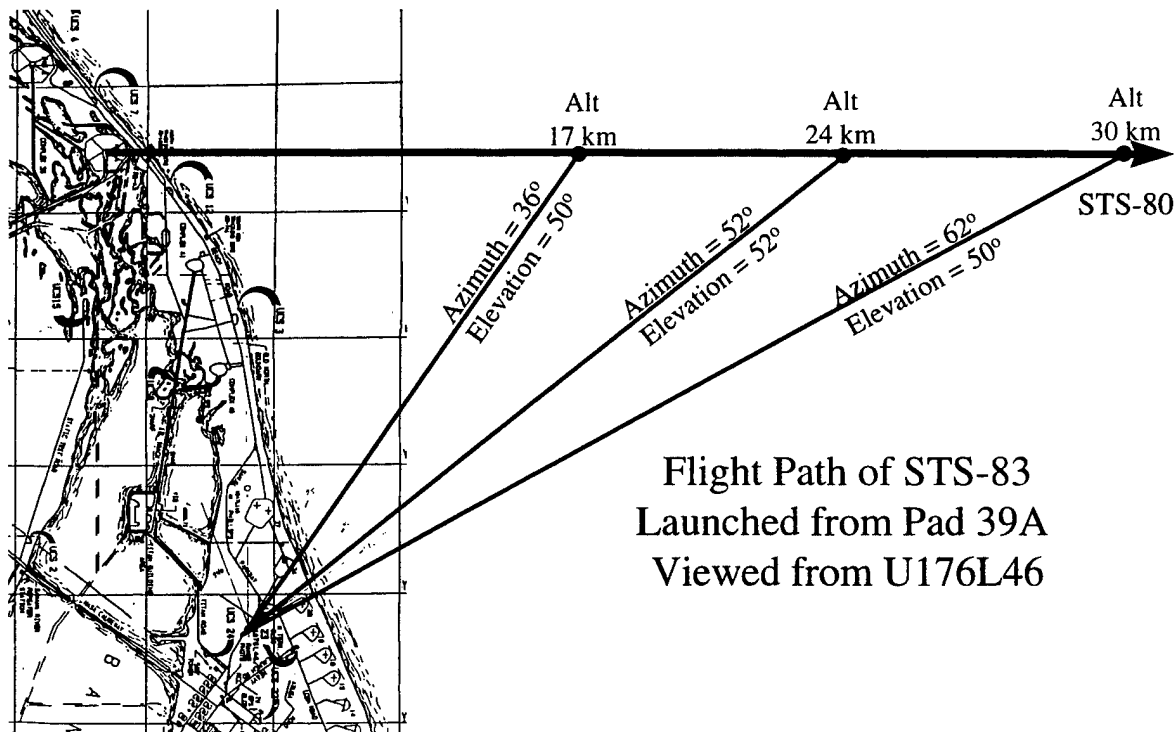


Figure 3-1. Scale map of the launch pad 39A, camera positions, ground projection of STS-83 trajectory, and viewing vectors at the three altitudes studied..

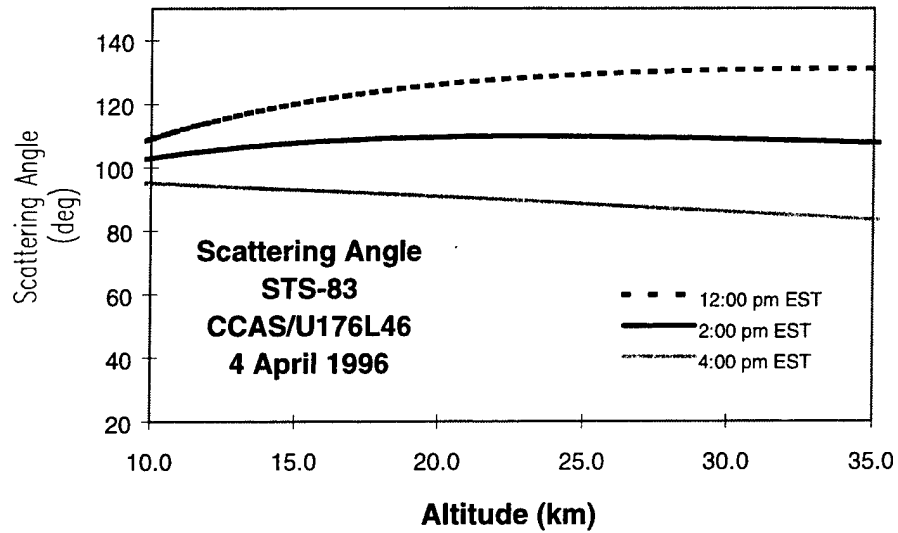


Figure 3-2. Scattering angle for three times. Launch time was just after 2:20 p.m.

Rawinsonde balloons were released during the day of the launch and provide stratospheric wind data. Figure 3-3 shows the wind data available closest to the time of vehicle launch. This rawinsonde balloon was released at 19:05 Zulu and rose at 1000 ft/min, reaching stratospheric altitudes about an hour later and bursting at an altitude of 28 km (110,000 ft). STS-83 passed through the stratosphere at 18:20 Zulu, about 2 h before these wind data were taken. As seen, the wind is predominately from the northeast with a magnitude varying between 1 and 9 m/s (0.06–0.5 km/min) at the two altitudes observed.

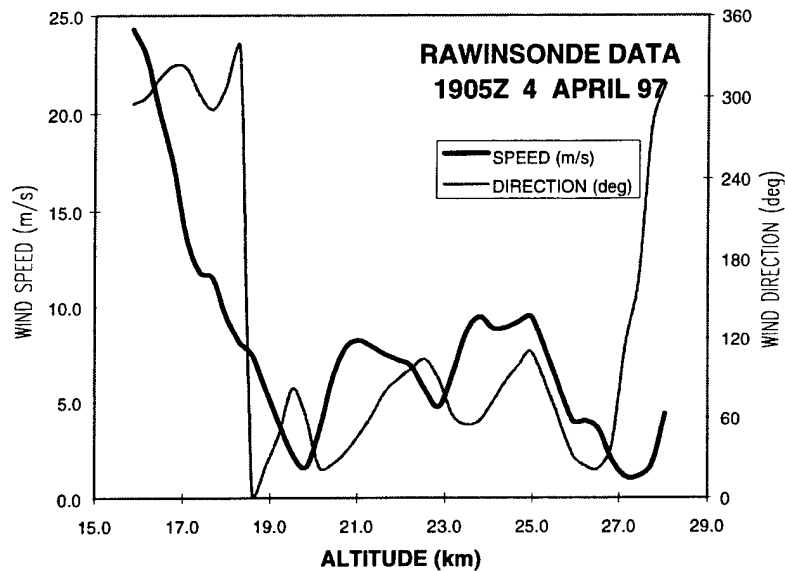


Figure 3-3. Stratospheric rawinsonde wind measurements about 10 h before STS-83 passage.

As discussed in Appendix 2, the motion of the centerline of the observed plume segment can be used to measure the wind speed if both the speed and direction of the plume are recorded. For this launch, the plume appeared to be stationary. This observation is consistent with the low velocity of the plume measured by the rawinsonde.

Strong northerly tropospheric winds blew sections of the lower plume in front of the stratospheric plume very soon after launch. Consequently, no data were obtained from the camera observing the 17-km altitude, and only about 3 min of expansion data were obtained from the 24 km and 30 km altitude cameras. Expansion rates presented in this section are based on these short-term data. Experience from previous measurements indicates that expansion rates inferred from the first 2–3 min of data can deviate significantly from those obtained when 10 or more minutes of data are used to calculate the expansion rate.

The plume widths as a function of time for the 24-km and 30-km altitudes are presented graphically in Figures 3-4 through 3-6. Figure 3-4 displays the data from the video camera assigned to the 24-km altitude; Figure 3-5 displays the data from the video camera assigned to the 30-km altitude; and Figure 3-6 displays the data from the still camera assigned to the 24-km altitude. The viewing geometry permitted the measurement of two altitudes for the 30-km video camera and for two altitudes for a lesser time for the still camera, thus allowing the inference of the plume expansion rate at the 24-km altitude to be made by three different instruments. The expansion rates measured at this altitude by the two video cameras agree well (avg = 0.27 km/min), and this average agrees with the rate measured with the still camera (0.26 km/min). The rate measured at the 30-km altitude by the video camera (0.40 km/min) is about 20% lower than that measured by the still camera (0.50 km/min). It is difficult to judge which of the two values is better. The 30-km video camera was set at a very short focal length, degrading the precision of the measurements (see Appendix 1). Although the still camera gave a larger view of the plume expansion, the 30-km altitude was visible in its images only for about 2.5 min of expansion, decreasing the reliability of the inferred expansion rate. Thus, an equal weighting of the values to obtain an average expansion rate of 0.45 km/min with an uncertainty of 20% is judged to be a conservative evaluation of the data. The second and third columns of Table I show the expansion rates obtained from linear fits to the datasets.

Table 3-1. Plume Expansion Rates (km/min)

Altitude (km)	STS-83		
	Video	Still	min
17	--	--	--
24	0.27	0.26	3
30	0.40	0.50	2-3

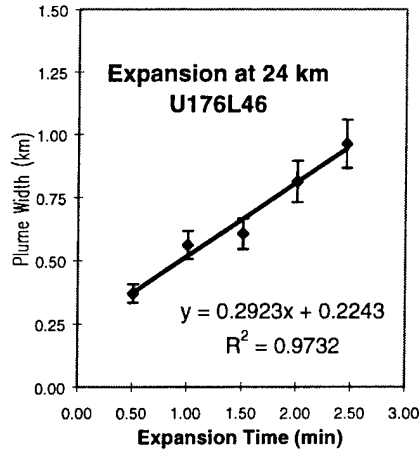


Figure 3-4. Plume width as a function of expansion time from U176L46 taken with the camera assigned to observe the plume at an altitude of 24 km.

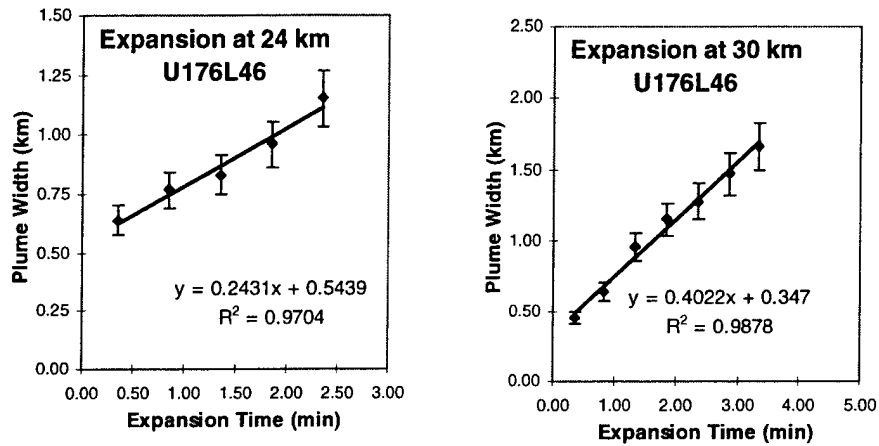


Figure 3-5. Plume width as a function of expansion time from U176L46 taken with the camera assigned to observe the plume at an altitude of 30 km.

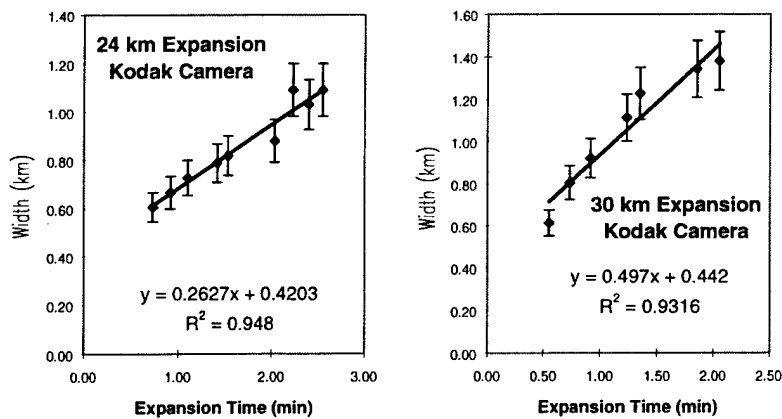


Figure 3-6. Plume width as a function of expansion time from U176L46 taken with the still camera assigned to observe the plume at an altitude of 24 km.

## Appendix 4—STS-94 Analysis

The STS-94 was launched from Pad 39A of the Kennedy Space Center at 2:02:02 p.m. EDT (1802Z) on 1 July 97 into partly cloudy skies with moderate haze. The launch was viewed from Camera Site U176L46 of Cape Canaveral Air Station (CCAS) which is 13.3 km south and 3.2 km east of Pad 39A. The location of Pad 39A and the camera site are shown in Figure 4-1.

Two identical instruments were used to study the expansion of the STS-94 SRM plume. Each instrument comprised a CCD video camera (equipped with a zoom lens, spectral filter, and polarizer), a video monitor, and a SVHS recorder. The focal lengths of both cameras were initially set to 30 mm, yielding a horizontal field-of-view of  $11^\circ$ . Subsequently, the focal length of the camera observing the 30-km altitude was changed to 20 and 15 mm.

The approximate vehicle ground track and the ground projection of the observation line-of-site vectors at the three altitudes studied also are shown to scale in Figure 4-1. The vehicle attained the 24-km altitude at  $T + 87.5$  s, and the 30-km altitude at  $T + 97.7$  s. There was an  $11^\circ$  change in the azimuth between the 24-km altitude position and the 30-km altitude position. This change was required to differentiate between these altitudes since there was less than  $1.5^\circ$  change in elevation between the two altitudes.

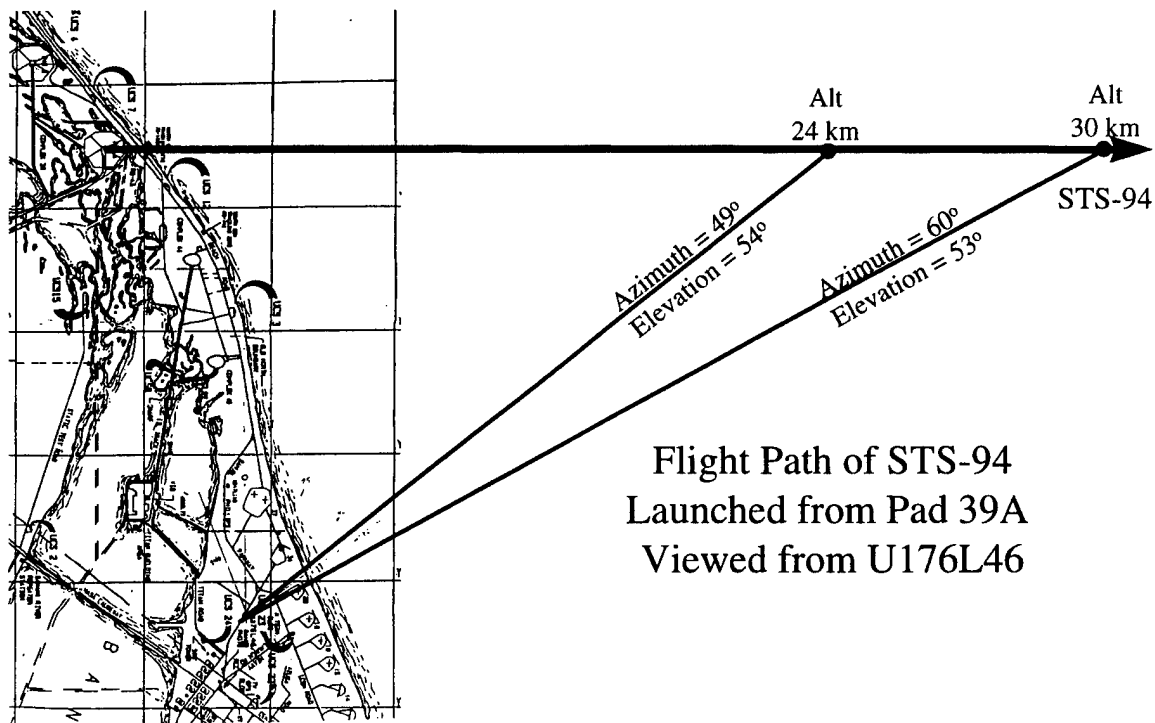


Figure 4-1. Scale map of the launch pad 39A, camera positions, ground projection of STS-94 trajectory, and viewing vectors at the two altitudes studied..

The scattering angles of the sunlight off the plume segment studied were calculated from the predicted trajectory and sun position; these angles are shown in Figure 4-2 as a function of altitude for three times of day. At launch time, just after 2:02 p.m. EDT, the scattering angle is between 90° and 100° between 24-km and 30-km altitude and which is nearly ideal for contrast enhancement using the polarization method described previously. Viewing the plume at infrared wavelengths also resulted in considerable contrast enhancement, which is expected based on previous analysis.

Rawinsonde balloons were released during the day of the launch and provided stratospheric wind data. Figure 4-3 shows the wind data available closest to the time of vehicle launch. This rawinsonde

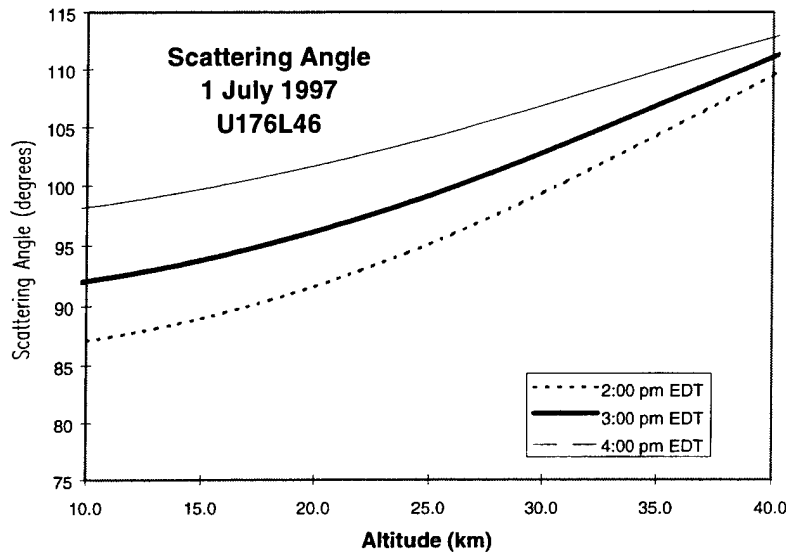


Figure 4-2. Scattering angle of light scattered from the plume for three different times. Launch time was just after 2:02 p.m.

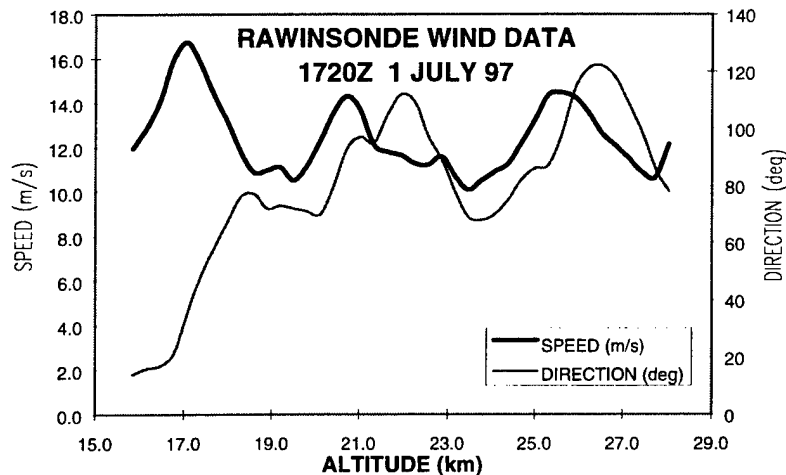


Figure 4-3. Stratospheric rawinsonde wind measurements about 1 h before STS-94 passage.

balloon was released at 17:20 Zulu and rose at 1000 ft/min, reaching stratospheric altitudes about an hour later and bursting at an altitude of 28 km (110,000 ft). STS-94 passed through the stratosphere at 18:04 Zulu, near the time these wind data were taken. As seen, the wind is predominately from the east with a magnitude varying between 10 and 16 m/s (0.60–0.96 km/min) at the two altitudes.

The plume widths as a function of time for the 24-km altitude are presented graphically in Figure 4-4; the diameters taken at 30-km altitude are shown in Figure 4-5. The measurements were terminated when sections of the tropospheric plume blew in from of the section of the stratospheric plume

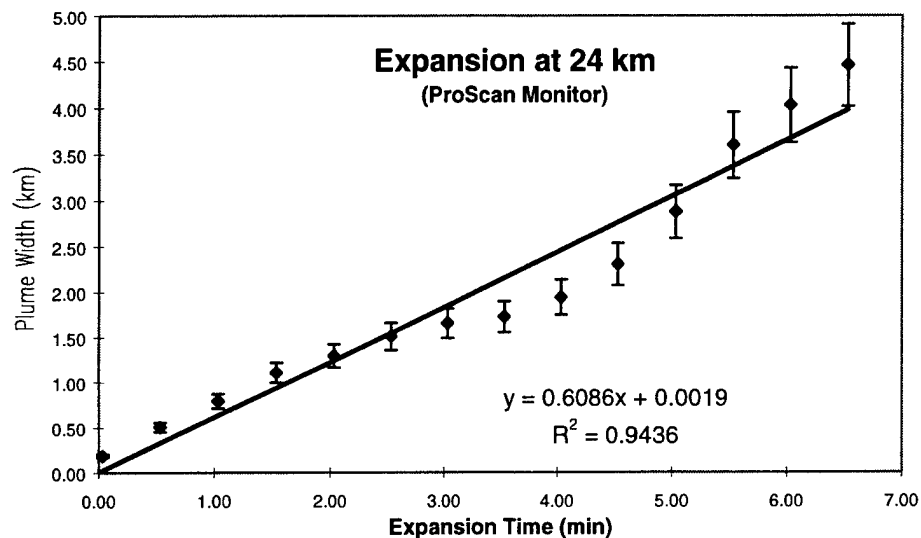


Figure 4-4. Plume width as a function of expansion time from U176L46 taken with the camera assigned to observe the plume at an altitude of 24 km.

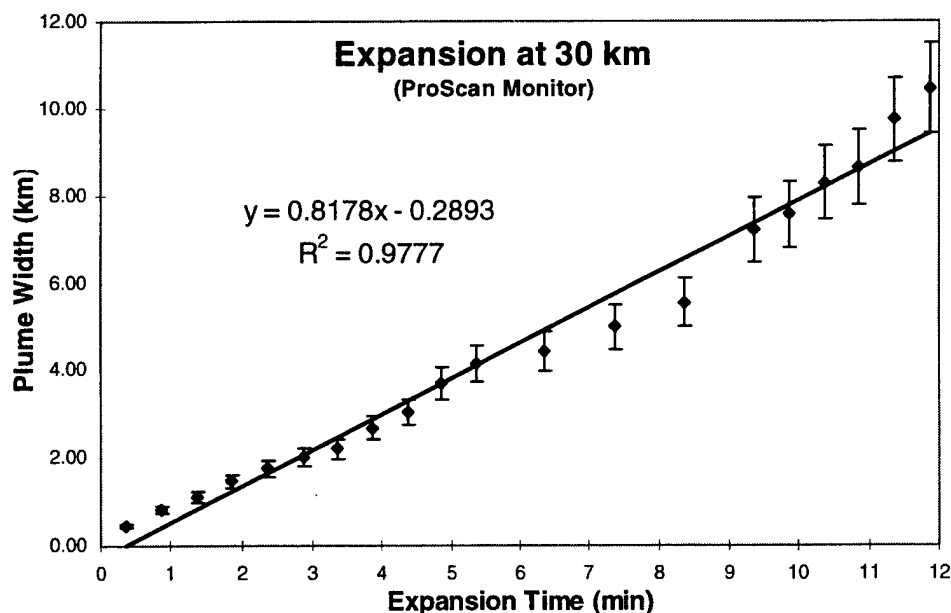


Figure 4-5. Plume width as a function of expansion time from U176L46 taken with the camera assigned to observe the plume at an altitude of 30 km.



studied. The diameters presented in these figures were measured on a large (41.4 cm x 30.8 cm) SVHS monitor. Linear fits to the diameters are shown on these plots. Note that there are significant deviations from linearity at both altitudes. The magnitude of these variations from linearity of the overall expansion rate were obtained by fitting linear subsets of the data. The results of these fits are shown in Table 4-1.

The data at both altitudes show up to a factor of 3 variation in the expansion rates during the observation periods. Note that each expansion rate decreases and/or increases with time but not monotonically. In viewing the gross motion of the plume on the video tape of the 30-km altitude data, it is apparent that there are significant variations in the velocity of plume moving across the sky. It is tempting to correlate these variations in plume velocity with the variations in plume expansion rates. The velocity of the plume can be estimated from this observed motion of the plume centerline.[See Appendix 2] Table 4-2 show the plume velocity estimated from the gross plume motion for several expansion times at this altitude. It is evident that these plume velocities do not correlate well with the plume expansion rates. For example, the plume expansion rate is constant during the first 3 min but the plume velocity shows its largest variation during that period. Note also that the highest expansion rate is during the 8–12 min interval when the plume is stationary. Furthermore, the motion of the plume centerline for the 24-km altitude data was nearly constant (at 0.45 km/min or 7 m/s) during the first 5 min of expansion, whereas the plume expansion showed significant variation during this time. These measurements of velocity are consistent with the rawinsonde data.

The principal results from these measurements are: the plume expansion rates at 24 and 30-km altitude were the largest values (0.61 and 0.82 km/min) observed to date at their respective altitudes. The deviations from linear expansion rates were also larger than have been previously observed. These large deviations could not be correlated with the large observed variations in wind velocity.

Table 4-1. STS-94 Plume Expansion Rates (km/min)

24 km			30 km		
Interval (min.)	Expansion Rate (km/min)	R <sup>2</sup>	Interval (min.)	Expansion Rate (km/min)	R <sup>2</sup>
0–2	0.56	0.993	0–3.4	0.59	0.993
2–4	0.30	0.976	2.9–5	0.88	0.979
4–7	1.06	0.992	5.5–8.5	0.47	0.982
0–7	0.61	0.944	8–12	1.35	0.987
			0–12	0.82	0.978

Table 4-2. STS-94 30-km Altitude Plume Velocity

Expansion Time (min)	Estimated Plume Velocity	
	(km/min)	(m/s)
0–1	1.0	17
1–2	0.4	6.7
2–3	0	0
3–4	0.2	3.3
5–6	0.9	15
6.5–7	0.7	12
7–13	0	0

## Appendix 5—STS-85 Analysis

The STS-85 was launched from Pad 39A of the Kennedy Space Center at 10:41:00.069 am EDT (1441 Z) on 7 August 97 into partly cloudy skies with extreme haze. The launch was viewed from a sandbar on Haulover Canal on Cape Canaveral Air Station (CCAS), which is 13.7 km north and 13.8 km west of Pad 39A. The locations of Pad 39A and the camera site are shown in Figure 5-1 as are the approximate vehicle ground track and the ground projection of the observation line-of-site vectors at the three altitudes studied. There was a  $27^\circ$  change in the azimuth between the 17-km altitude position and the 30-km altitude position. The change in elevation was  $4^\circ$  between the 17 and 30 km altitudes. The ground projection of the viewing vector and ground projection of the trajectory was about  $60^\circ$  at the 24-km altitude. The focal length of all three cameras was initially set to 48 mm, yielding a horizontal field-of-view of  $7^\circ$ . Subsequently, the focal length of the camera observing the 17-km altitude was sequentially decreased to 30, 20, 15, and 10 mm.

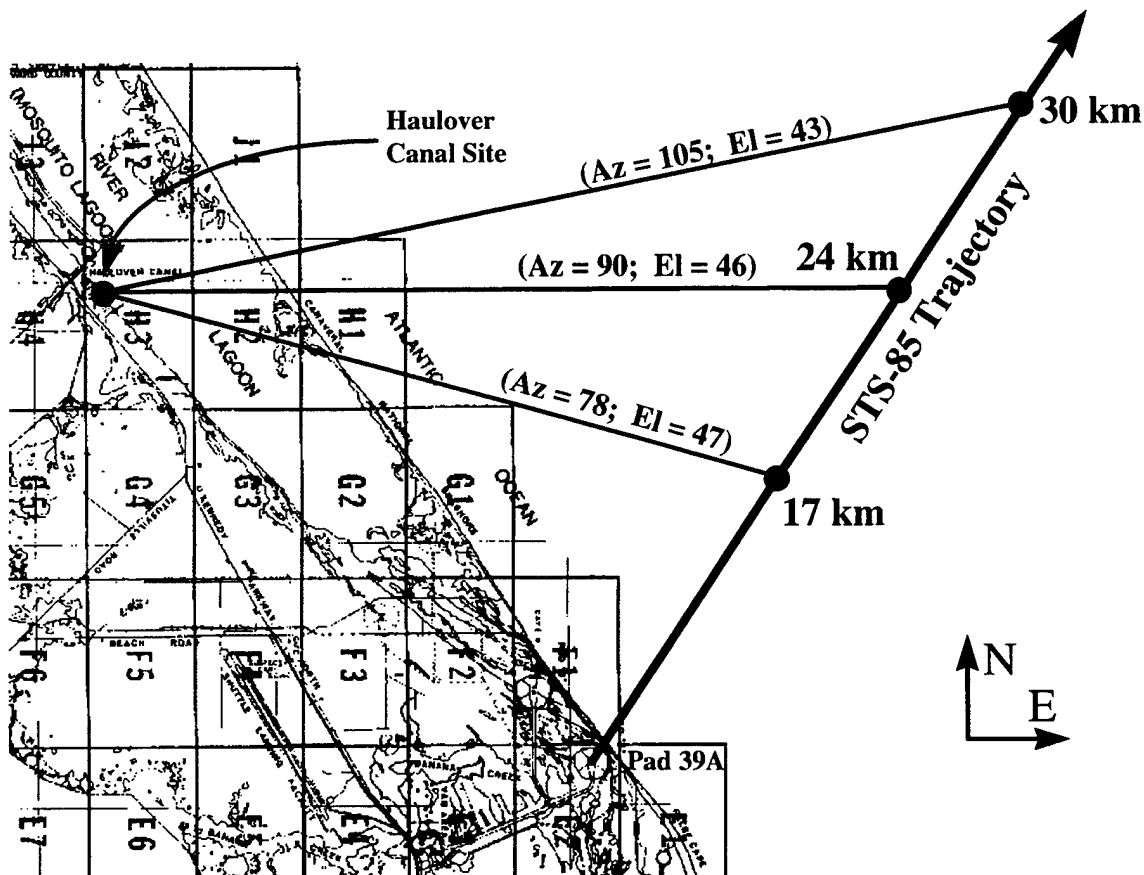


Figure 5-1. Scale map of the launch pad 39A, cameras' position, ground projection of STS-85 trajectory, and viewing vectors at the three altitudes studied.

The scattering angles of the sunlight off the plume segment studied are shown in Figure 5-2 as a function of altitude for three times of day. At launch, just after 10:41 p.m. EDT, the scattering angle is between 110° and 115° between 17-km and 30-km altitude, which is advantageous for contrast enhancement using the polarization method. The extreme haze (turbidity) during the launch and subsequent observation period depolarized the sunlight scattered by the atmosphere, mitigating the ability of the polarizer to enhance the contrast of the plume. Viewing the plume at infrared wavelengths, however, resulted in considerable contrast enhancement over that seen by eye, which is expected based on previous analysis. [Beiting, 1999]

Rawinsonde balloons were released during the day of the launch and provided stratospheric wind data. Figure 5-3 shows the wind data available closest to the time of vehicle launch. This rawinsonde balloon was released at 1411 Zulu and rose at 1000 ft/min, reaching stratospheric altitudes

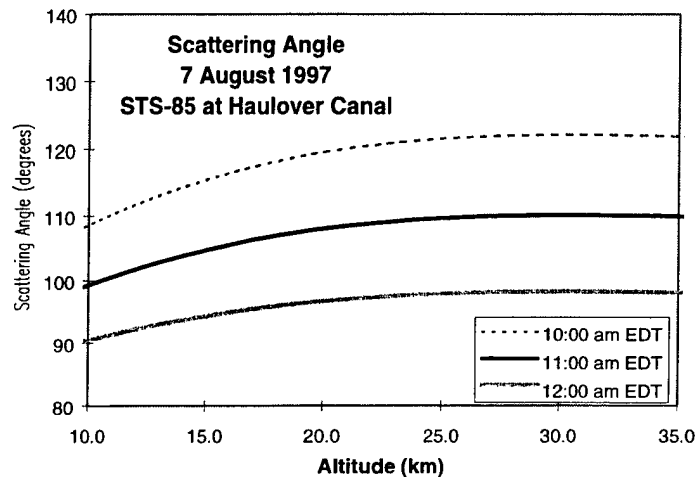


Figure 5-2. Scattering angle of light scattered from the plume for three different times. Launch time was 10:41 a.m. EDT.

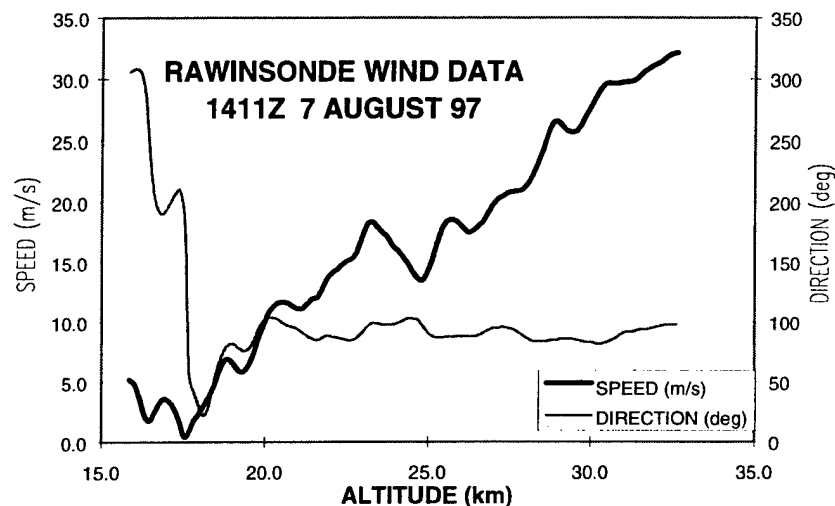


Figure 5-3. Stratospheric rawinsonde wind measurements about a half an hour after STS-85 passage.

about an hour later (15:00Z) and bursting at an altitude of 33 km (107,000 ft). STS-85 passed through the stratosphere at 1442 Zulu, about a half an hour before these wind data were taken. As seen, the wind is predominately from the east showing very little change in direction in the 17–30 km altitude range. The wind speed increased nearly monotonically from near 0 to 30 m/s (0–1.8 km/min) in this altitude range.

The plume widths as a function of time for the 17-km altitude are presented graphically in Figure 5-4; the diameters taken at 24-km altitude are shown in Figure 5-5; and the diameters taken at 30-km altitude are shown in Figure 5-6. The measurements were made under extremely hazy conditions and with viewing angles close to that of the sun. Measurements were terminated when clouds blocked the view of the plume (17 km) or when the edge of the camera's field-of-view began to intercept the sun. The plume centerline appeared stationary on the screen at the 17-km altitude, but was moving rapidly across the sky at the 30-km altitude. The plume centerline movement at the 24-km altitude was intermediate between these two extremes. These observations are consistent with the rawinsonde data presented in Figure 5-3.

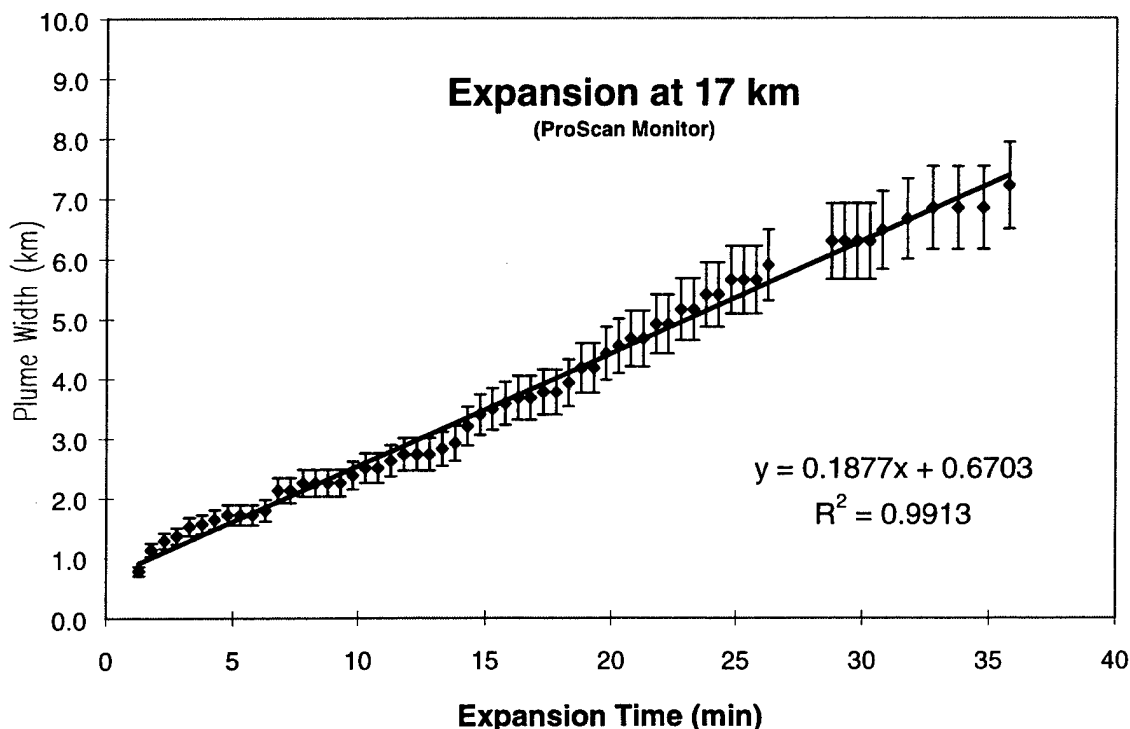


Figure 5-4. Plume width as a function of expansion time from Haulover Canal taken with the camera assigned to observe the plume at an altitude of 17 km.

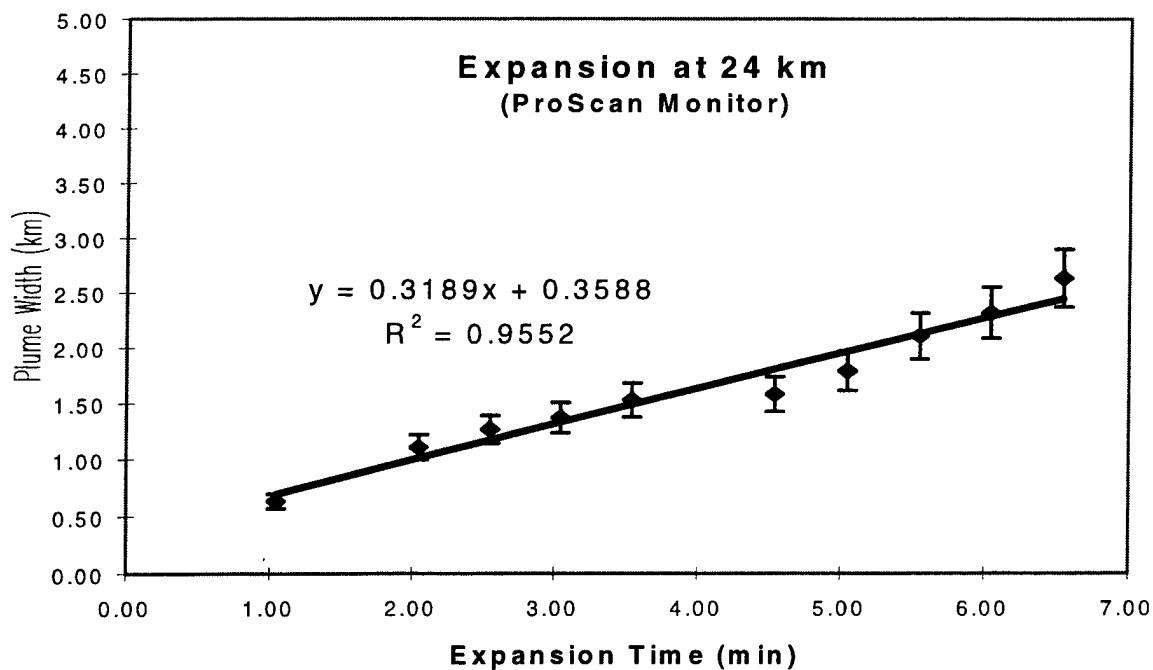


Figure 5-5. Plume width as a function of expansion time from Haulover Canal taken with the camera assigned to observe the plume at an altitude of 24 km.

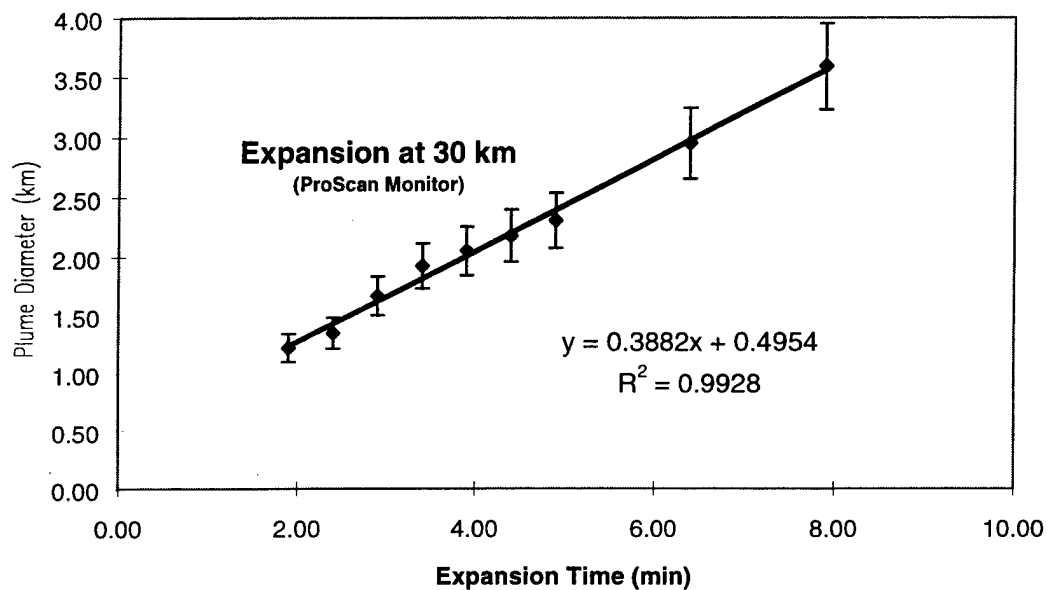


Figure 5-6. Plume width as a function of expansion time from Haulover Canal taken with the camera assigned to observe the plume at an altitude of 30 km.

Linear fits to the diameters are shown on these plots. Although there are short-term deviations from linearity in the 17-km altitude data, the expansion rates at this and the other two altitudes are remarkably constant. The measurement time interval (36 min.) at the 17-km altitude is the longest seen to date by a factor of 3. This is the first successful measurement at this altitude during this observation program (previous attempts at recording the expansion at this altitude were unsuccessful because portions of the tropospheric plume blew in front of this section of the plume at very early expansion times). For the 17-km altitude, the magnitude of the variations from linearity from the overall expansion rate were obtained by fitting linear subsets of the data. The results of these fits are shown in Table 5-1. The largest sub-interval excursion of the expansion rate from the overall expansion rate is about 30%, a small value compared with the maximum variation from the mean of about 200% seen the STS-94 data [Appendix 4].

The principal results from these measurements are: the plume expansion rates at 17-, 24-, and 30-km altitude measured increased monotonically with altitude in agreement with the general trend seen emerging from the previous measurements; the magnitudes of the expansion rates are somewhat less than those observed in the previous observation for the respective altitudes but within the deviations of the measurements. The plume velocities were not estimated from the plume centerline motion for this work but were in agreement qualitatively with the rawinsonde data taken very close to the time of the passage of the STS-85 through the stratosphere.

Table 5-1. Sub-interval Plume Expansion Rates at 17 km

Expansion Time (min)	Rate (km/min)	R <sup>2</sup>
2-6	0.14	0.987
7-14	0.13	0.942
15-25	0.23	0.987
29-37	0.13	0.928
1-36	0.19	0.991

## Appendix 6—STS-90 Analysis

The STS-90 was launched from Pad 39B of the Kennedy Space Center at 2:19 p.m. EDT (1819 Z) on 17 April 98 into cloudy skies. The launch was viewed from camera site U176L46, which is 13.4 km south and 4.8 km east of Pad 39B and a sandbar on Haulover Canal on Cape Canaveral Air Station (CCAS), which is 11.6 km north and 12.2 km west of Pad 39B. The locations of Pad 39B and the camera sites are shown in Figure 6-1

There was a  $15^\circ$  change in the azimuth between the 18-km altitude position and the 30-km altitude position at the Haulover site and a  $14^\circ$  change in the azimuth between these two positions at the U176L46 site. The change in elevation was  $4^\circ$  and  $3^\circ$  between the 18- and 30-km altitudes for the two sites, respectively. Thus the two sites were nearly identical in the views afforded. The angle between the ground projection of the viewing vector and the ground projection of the trajectory was between  $30^\circ$  and  $35^\circ$  at the 24-km altitude. One video camera and the electronic still camera were deployed at the Haulover Canal site, and the other two video cameras were deployed at the U176L46 camera site.

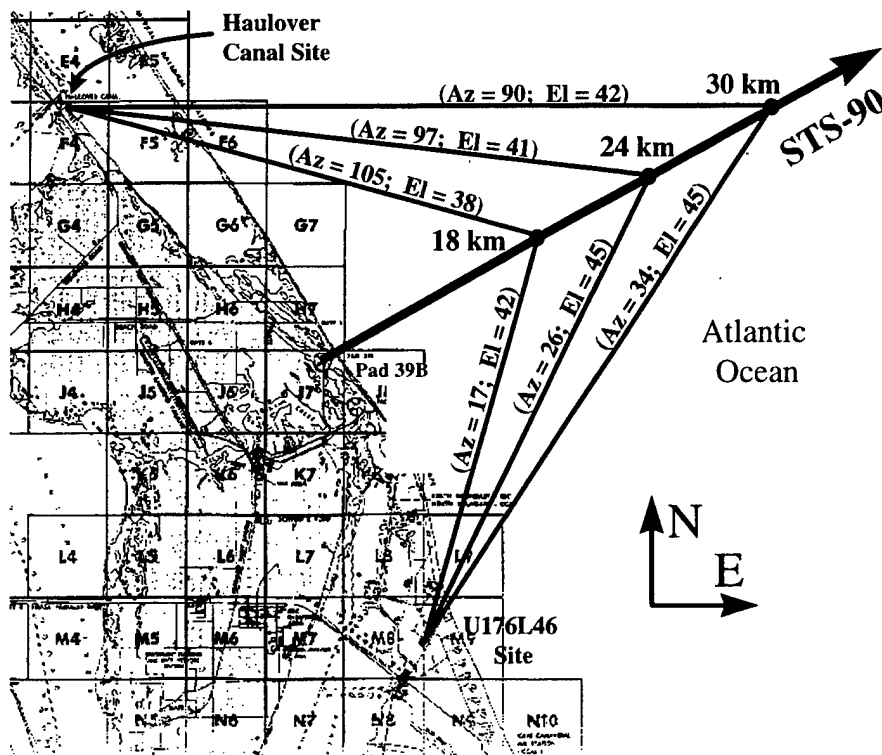


Figure 6-1. Scale map of the launch pad 39B, camera positions, ground projection of STS-90 trajectory, and viewing vectors at the three altitudes studied for both the Haulover and U176L46 sites.

Under conditions of low atmospheric turbidity (little haze), images of the plume can be recorded with enhanced contrast through a polarizer oriented parallel to the scattering plane if the scattering angle is between  $90^\circ$  and  $120^\circ$ . As seen in Figures 6-2 and 6-3, at time of launch, just after 2:19 p.m. EDT, the scattering angle is below  $90^\circ$ , and polarization was not useful for contrast enhancement using the polarization method. Viewing the plume at infrared wavelengths, however, resulted in considerable contrast enhancement over that seen by eye.

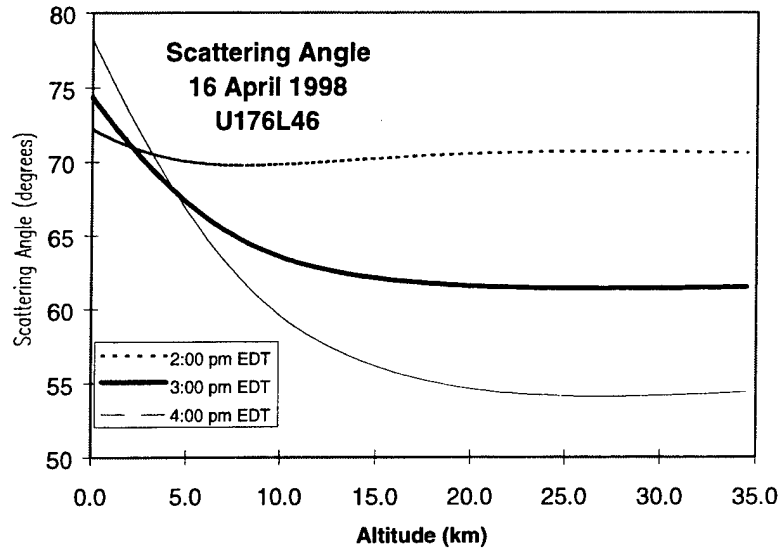


Figure 6-2. Scattering angle of light scattered from the plume for three different times as viewed from U176L46. Launch time was 2:19 p.m. EDT.

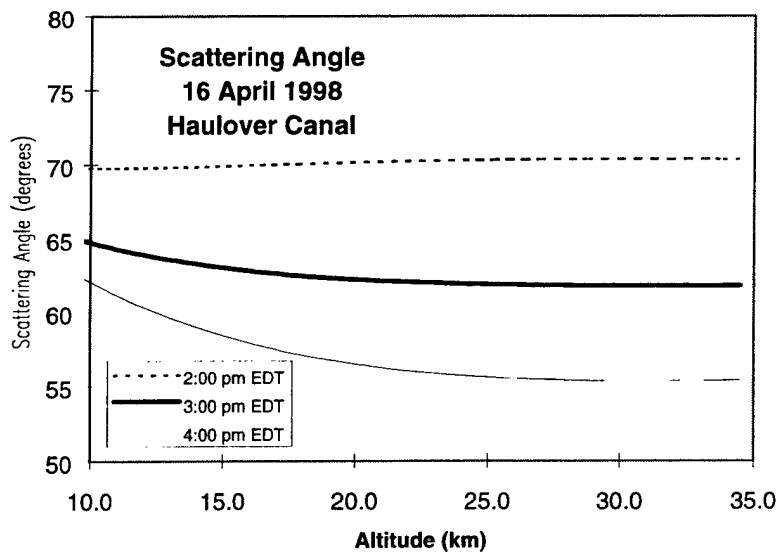


Figure 6-3. Scattering angle of light scattered from the plume for three different times as viewed from Haulover Canal. Launch time was 2:19 p.m. EDT.



Figure 6-4 shows the wind data available closest to the time of vehicle launch. This rawinsonde balloon was released at 1449 Zulu and rose at 1000 ft/min, reaching stratospheric altitudes about an hour later (16:00 Z) and bursting at an altitude of 28 km (92,000 ft). STS-90 passed through the stratosphere at 18:20 Zulu, about two and a half hours after these wind data were taken. As seen, the wind is predominately from the southeast, showing very little change in direction in the 20–26 km altitude range. The wind speed was nearly constant with a relatively low value of about 5 m/s (0.3 km/min) between 19 and 28 km.

The plume widths as a function of time for the 18-km altitude are presented graphically in Figure 6-5 for the Haulover site and Figure 6-6 for the U176L46 camera site. Clouds obscured the view of the plume for most of the observation period at the Haulover site, but because the plume appeared to be absolutely stationary, it was possible to make measurements at irregular intervals for 11 min at the 18-km altitude. The cloud cover precluded measurements at the higher altitudes at this site. It is clear from Figure 6-5 that the plume did not expand uniformly during the 11 min. The subinterval rates for this dataset are given in Table 6-1. During the first 3 min, the plume expanded at a rate of 0.28 km/min and then slowed by a factor of 4. However, because the plume could not be monitored continuously, the later definitions of the edges of the plume may not correlate well with the earlier definitions, leading to a discontinuity in the identification of the plume diameter. However, it was clear at a later time that the plume was largely stationary in the sky and not expanding at its earlier rate. At the U176L46 site, the tropospheric plume obscured the 18-km altitude after only 3 min of expansion, but this site measured the same expansion rate for this period as did the Haulover site, indicating a symmetrical expansion for these two viewing projections. In assigning an expansion rate for this altitude, this later rate will be given half weight of the earlier rates, leading to an average rate of 0.24 km/min.

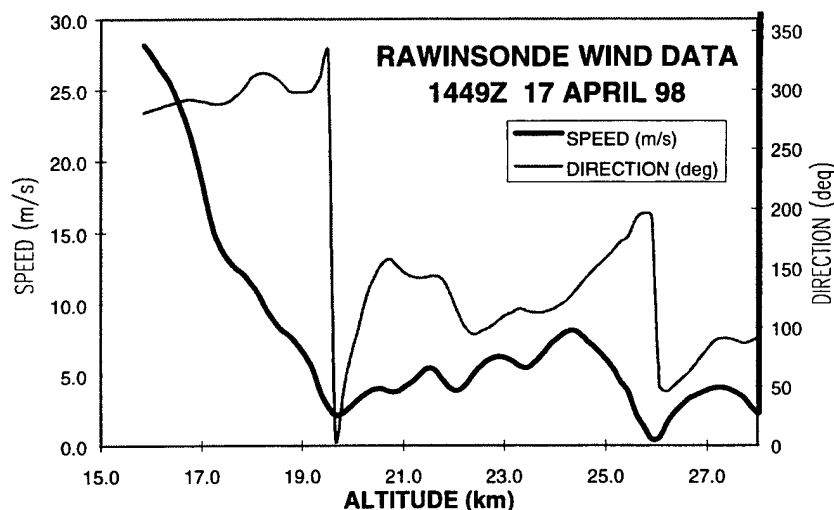


Figure 6-4. Stratospheric rawinsonde wind measurements about 2.5 hours before STS-90 passage.

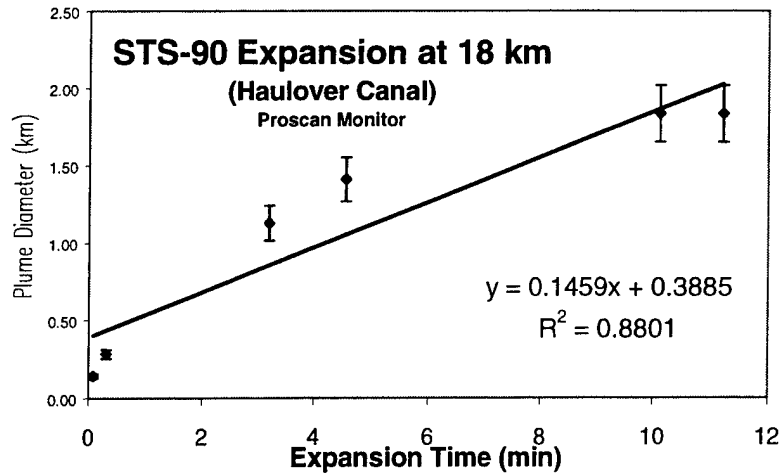


Figure 6-5. Plume width as a function of expansion time from Haulover Canal taken with the camera assigned to observe the plume at an altitude of 18 km.

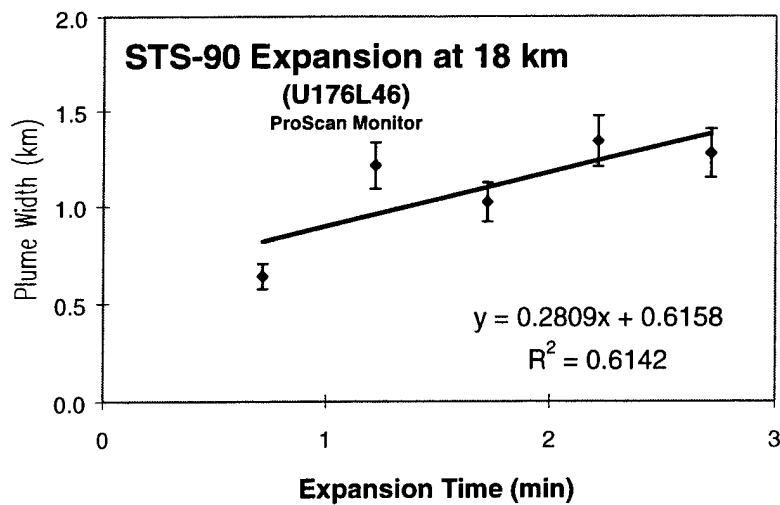


Figure 6-6. Plume width as a function of expansion time from the U176L46 camera site taken with the camera assigned to observe the plume at an altitude of 18 km.

Table 6-1. Haulover Sub-interval Plume Expansion Rates at 18 km

Expansion Time (min)	Rate (km/min)	R <sup>2</sup>
0-4.5	0.28	0.993
4.5-11	0.07	0.976
4.5-11	0.15	0.88

One camera at the U176L46 site was able to observe the 24–30 km altitude range. The plume also appeared stationary at these higher altitudes. The diameters taken at the 24-km altitude, displayed in Figure 6-7, show a uniform expansion rate during the 4-min measurement period available before this plume section was blocked from view by the lower plume. At the upper altitudes, the expansion was observed for 25 min. An altitude of 27 km was optimal for observation by this camera. These data and those for the 30-km altitude are presented in Figures 6-8 and 6-9, respectively. The expansion rates at these two altitudes were not constant as shown in Tables 6-2 and 6-3 where the subinterval expansion rates are presented. The early plume at the 27-km altitude expanded at a slightly lower rate at early times than did the 30-km plume. During the last 10 min of expansion, the 27- and 30-km altitudes had the same expansion rates. Thus, the average expansion rate over the 25-min observation period was slightly less at the 27-km altitude than at the 30-km altitude. The subinterval expansion rate varied by more than a factor of 2 during the observation period. The average expansion rates for all altitudes are presented in Table 6-4.

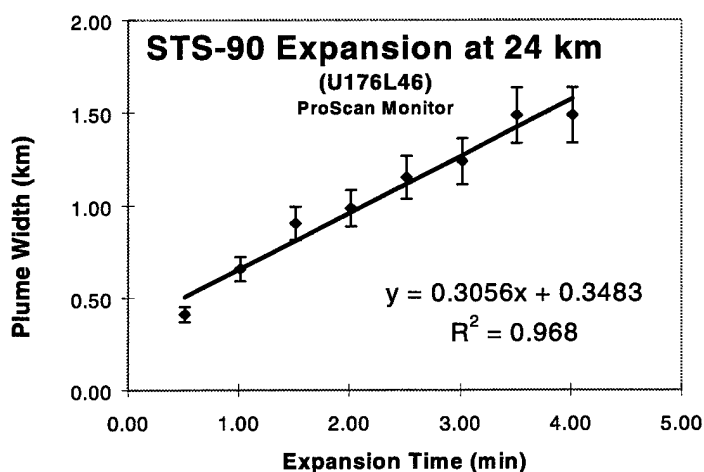


Figure 6-7. Plume width at 24 km as a function of expansion time from U176L46.

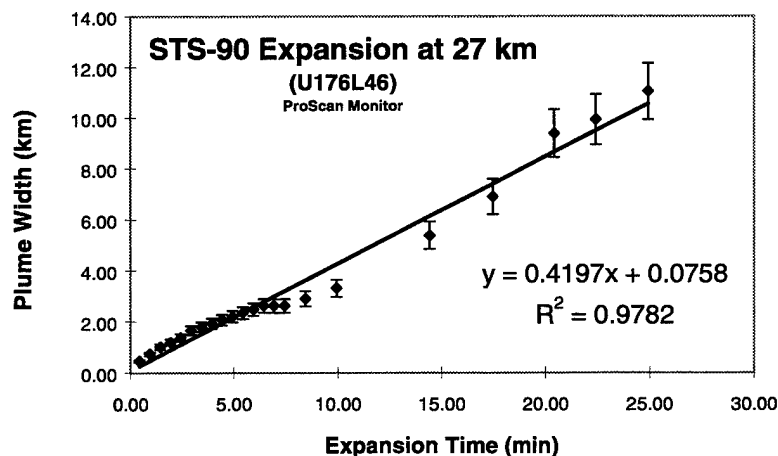


Figure 6-8. Plume width at 27 km as a function of expansion time from U176L46.

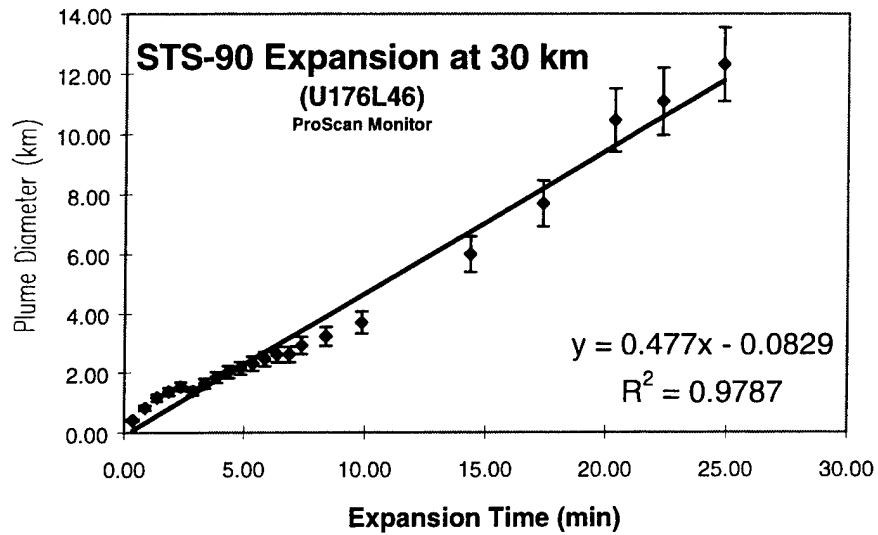


Figure 6-9. Plume width at 30 km as a function of expansion time from U176L46 taken with the camera assigned to observe the plume in the altitude range of 24 - 30.

Table 6-2. Sub-interval Plume Expansion Rates at 27 km

Expansion Time (min)	Rate (km/min)	R <sup>2</sup>
0-2.3	0.46	0.989
3-8.5	0.22	0.969
14-25	0.62	0.978
0.3-25	0.42	0.978

Table 6-3. Sub-interval Plume Expansion Rates at 30 km

Expansion Time (min)	Rate (km/min)	R <sup>2</sup>
0-2.3	0.56	0.964
3-8.5	0.32	0.987
14-25	0.62	0.978
0.3-25	0.48	0.979

Table 6-4. STS-90 Plume Expansion Rates

Altitude (km)	Rate (km/min.)		Duration (min)
	Subinterval	Average	
18 Haulover	0.28/0.07	0.15	11
18 U176L46	--	0.28	3
24	--	0.31	4
27	0.46/0.22/0.62	0.42	25
30	0.56/0.32/0.62	0.48	25

The principal results from these measurements are: the plume expansion rates at 18, 24, 27, and 30 km altitude increased monotonically with altitude in agreement with the general trend seen emerging from the previous measurements; the magnitudes of the expansion rates are consistent with those observed in the previous observation for the respective altitudes and within the deviations of the measurements. The plume appeared stationary from both observation sites, which is consistent with the low rawinsonde velocities measured 2.5 h before the rocket passed through the stratosphere.

## Appendix 7—STS-91 Analysis

The STS-91 was launched from Pad 39A of the Kennedy Space Center at 6:06:24 p.m. EDT (2206 Z) on 2 June 98 into partly cloudy skies. The launch was viewed from camera site U176L46, which is 11.3 km south and 3.2 km east of Pad 39A and a sandbar on Haulover Canal on Cape Canaveral Air Station (CCAS), which is 13.7 km north and 13.8 km west of Pad 39A. The locations of Pad 39A and the camera sites are shown in Figure 7-1.

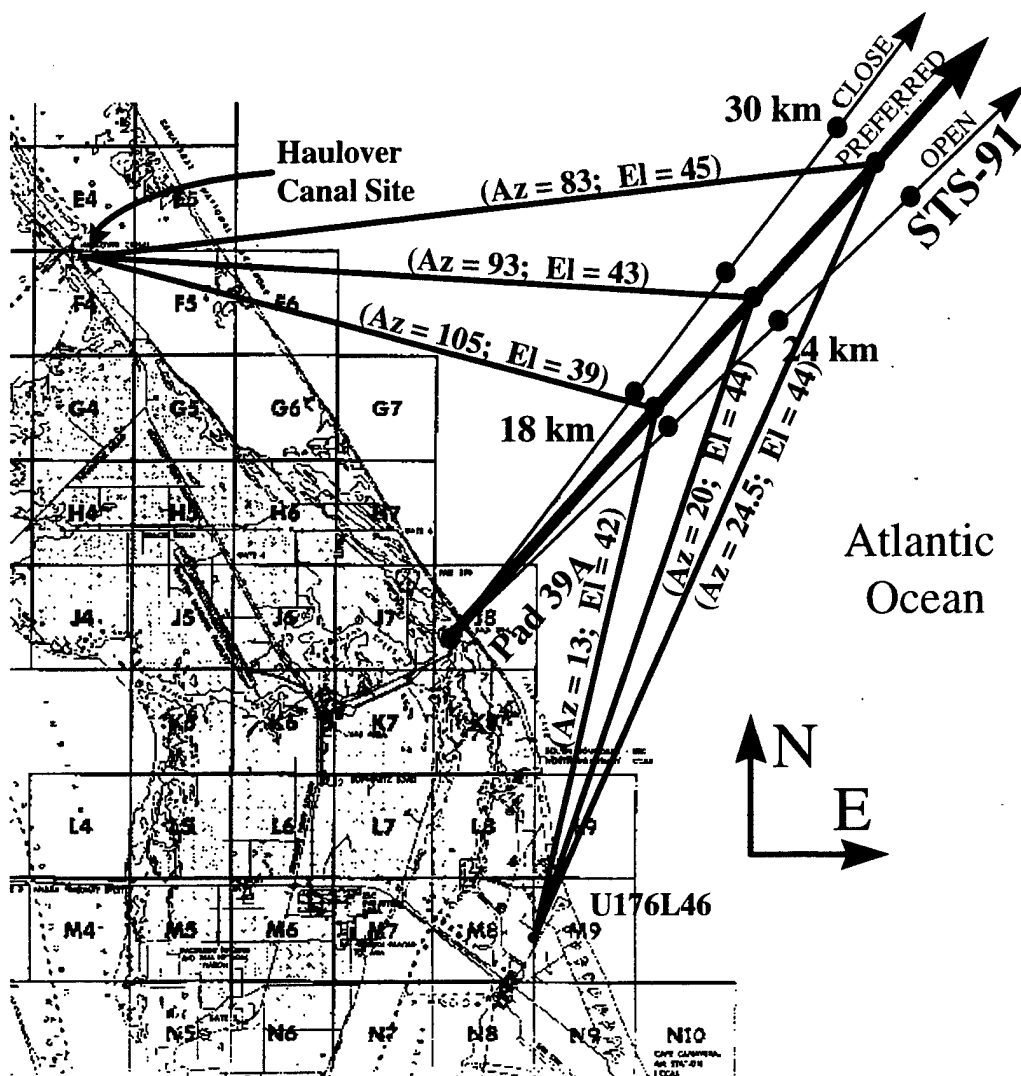


Figure 7-1. Scale map of the launch pad 39A, camera positions, ground projection of STS-91 trajectory and viewing vectors at the three altitudes studied for both the Haulover Canal and U176L46 sites. There was a significant change in the trajectory over the period of the 7 min launch window as indicated by the three trajectories plotted. STS91 followed the path marked OPEN.

The approximate vehicle ground track and the ground projection of the observation line-of-site vectors at the three altitudes studied also are shown to scale in Figure 7-1. Because this shuttle flight was launched to rendezvous with the MIR Space Station, there was a significant change in trajectory from the opening to the closing of the 7 min launch window. The liftoff took place near the opening of the launch window at 6:06 p.m. EDT instead of the preferred time (6:09 p.m. EDT) in order to get extra hold time if required to solve last-minute concerns during the countdown.

The vehicle attained the 18-km altitude at  $T + 77$  s, 24-km altitude at  $T + 88$  s and the 30-km altitude at  $T + 98$  s. There was a  $20.5^\circ$  change in the azimuth between the 18-km altitude position and the 30-km altitude position at the Haulover site and a  $12.7^\circ$  change in the azimuth between these two positions at the U176L46 site. The change in elevation was  $5.5^\circ$  and  $1^\circ$  between the 17- and 30-km altitudes for the two sites, respectively. The angle between the ground projection of the viewing vector and ground projection of the trajectory at the 24-km altitude was  $52^\circ$  at Haulover and  $37^\circ$  at U176L46 compared to an ideal orthogonal viewing angle for maximum differentiation of the different altitude positions in the plume. Thus, the Haulover site offered substantially better separation among the altitudes. Accordingly, three of the four instruments were deployed at that site. One video camera was placed at the U176L46 site in case the view of the plume from the Haulover site was blocked by clouds.

The scattering angles of the sunlight off the plume segment studied were calculated and are shown in Figure 7-2 for the main Haulover site as a function of altitude for three times of day. At launch, just after 6:06 p.m. EDT, the scattering angle is below  $90^\circ$ , and polarization is not useful for contrast enhancement using the polarization method. Viewing the plume at infrared wavelengths, however, resulted in considerable contrast enhancement over that seen by eye.

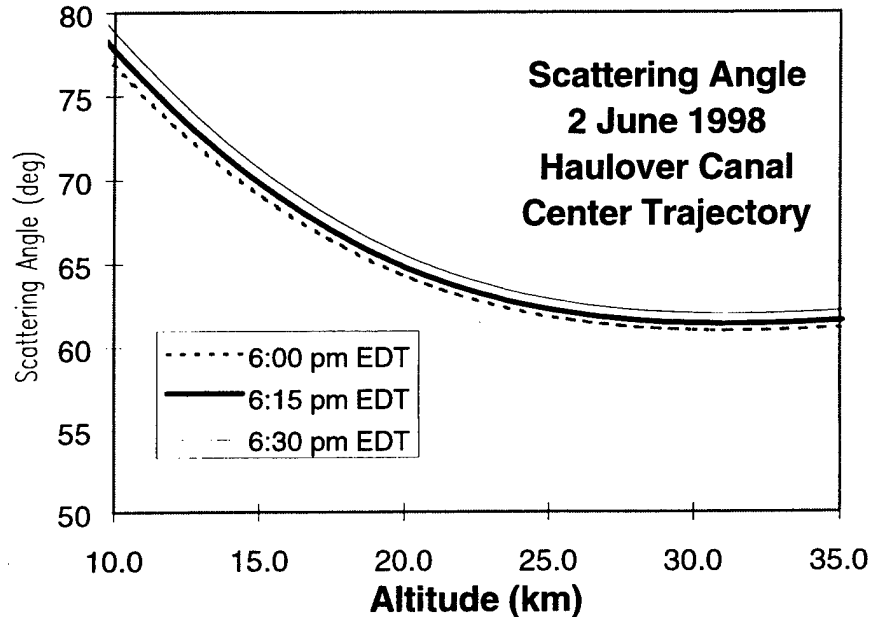


Figure 7-2. Scattering angle of light scattered from the plume for three different times as viewed from Haulover Canal. Launch time was 6:06 p.m. EDT.

Rawinsonde balloons were released during the day of the launch and provided stratospheric wind data. Figure 7-3 shows the wind data available closest to the time of vehicle launch. This rawinsonde balloon was released at 2135 Zulu and rose at 1000 ft/min, reaching stratospheric altitudes about an hour later (2235 Z) and bursting at an altitude of 29 km (95,000 ft). STS-91 passed through the stratosphere at 2207 Zulu, less than a half an hour before these wind data were taken. As seen, the wind is predominately from the east showing very little change in direction in the 20–29 km altitude range. The wind speed varied between 5 and 15 m/s (0.3–0.9 km/min) between 18 and 29 km.

The plume widths as a function of time for the 18-km altitude are presented graphically in Figure 7-4 for the Haulover camera site. At this altitude, the plume expanded uniformly for the first 20 min until the edges of the plume moved beyond the field-of-view of the instrument. Subsequently, the instrument was adjusted to its shortest focal length, and the measurements were resumed and continued to 50 min of expansion, the longest measurement to date. The 15-min gap in the data shown in Figure 7-4 is the period before the lens was readjusted. The plume width was no longer measurable beyond 50 min when its diameter exceeded the field-of-view of the lens at its shortest focal length (8mm). The increase in plume diameter with time is remarkably linear during this period with an  $R^2$  value of 0.989.

Clouds obscured the view of the plume for higher altitudes at this site, restricting the measurements to about 10 min at 24 km and 9 min at 30 km. The electronic still camera measured the expansion at both 24- and 30-km altitudes, obtaining values of 0.41 and 0.46 km/min, respectively (see Figures 7-5 and 7-6). The expansion rate was also nearly constant with an  $R^2$  value of 0.988. The video camera measured the expansion at 30 km only (see Figure 7-7), obtaining an expansion rate of 0.53 km/min, about 15% higher than the electronic camera, which is within the accuracy of the measurements.

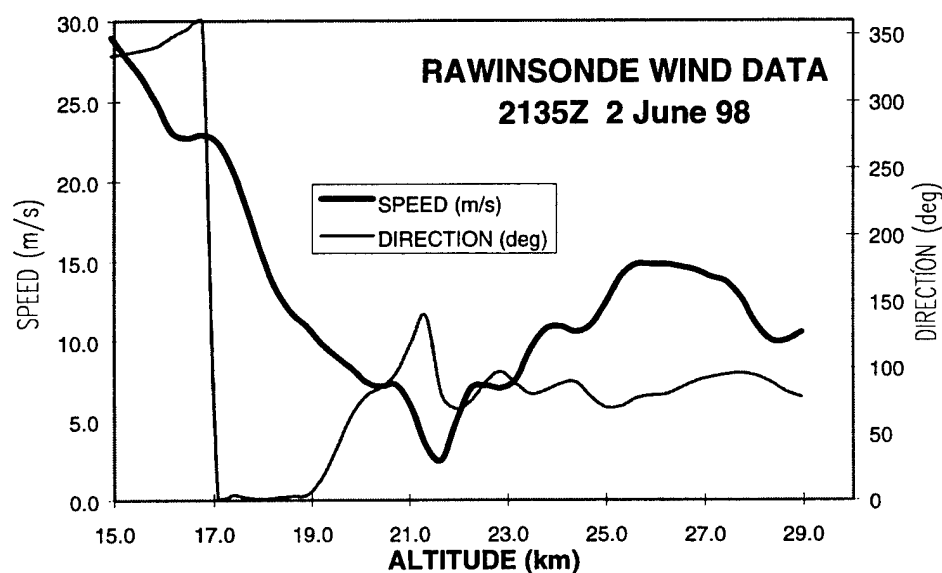


Figure 7-3. Stratospheric rawinsonde wind measurements about 0.5 an h after STS-91 passage.



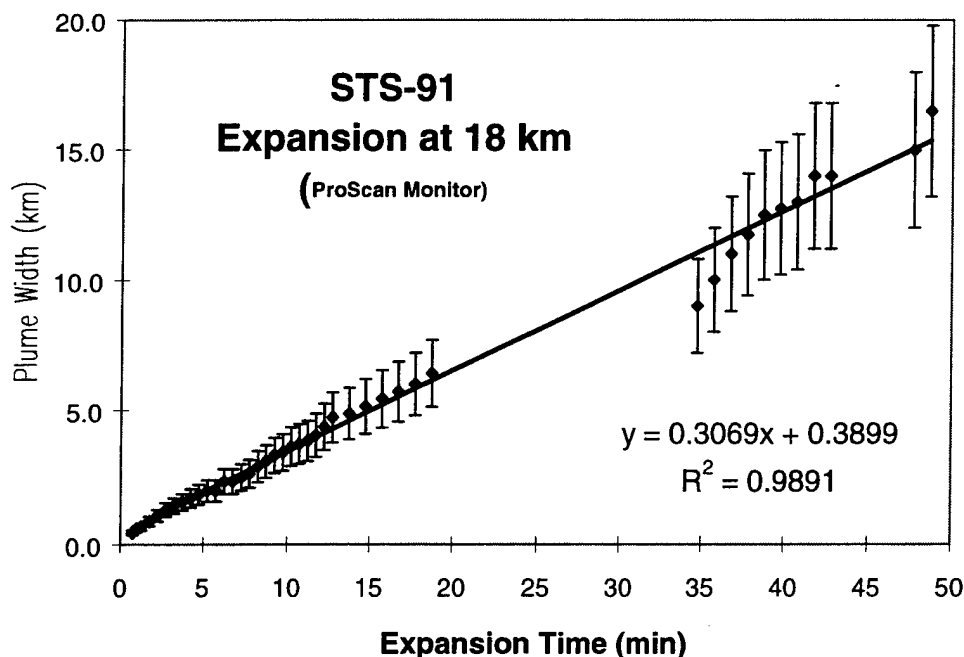


Figure 7-4. Plume width as a function of expansion time from Haulover Canal taken with the video camera assigned to observe the plume at an altitude of 18 km.

One camera at the U176L46 site tracked the 24-30 km altitude range. The 24-km altitude section of the plume was quickly blocked from view by a portion of the tropospheric plume. The 30-km altitude was subsequently blocked at about 3 min of expansion. However, the stratospheric plume reappeared at irregular intervals as the lower plume blew rapidly across the largely stationary (from this viewing angle) stratospheric plume section being observed. These data are shown in Figure 7-8. Because the measured plume section was not continuously observable, the diameters obtained at this site for this altitude are less certain than if the continuous evolution of the plume were followed. For comparison with the other two measurements at this altitude, the short-term rate (0-12 min) is 0.71 km/min, or about 35% higher than that obtained from the Haulover site for this altitude. This variation could be due to the different viewing angle (non-cylindrically symmetric expansion rate), or, more likely, differences in defining the edge of the plume due to different atmospheric conditions between the sites, or contrast enhancement techniques (used with the electronic still camera), or a combination of these three effects. Experience shows that expansion rates measured for short time intervals (or sub-intervals of a long measurement) can vary significantly from the values averaged for long time intervals. The average of the three rates for the first 10 min is 0.57 km/min, identical to the 25-min rate measured at this site.

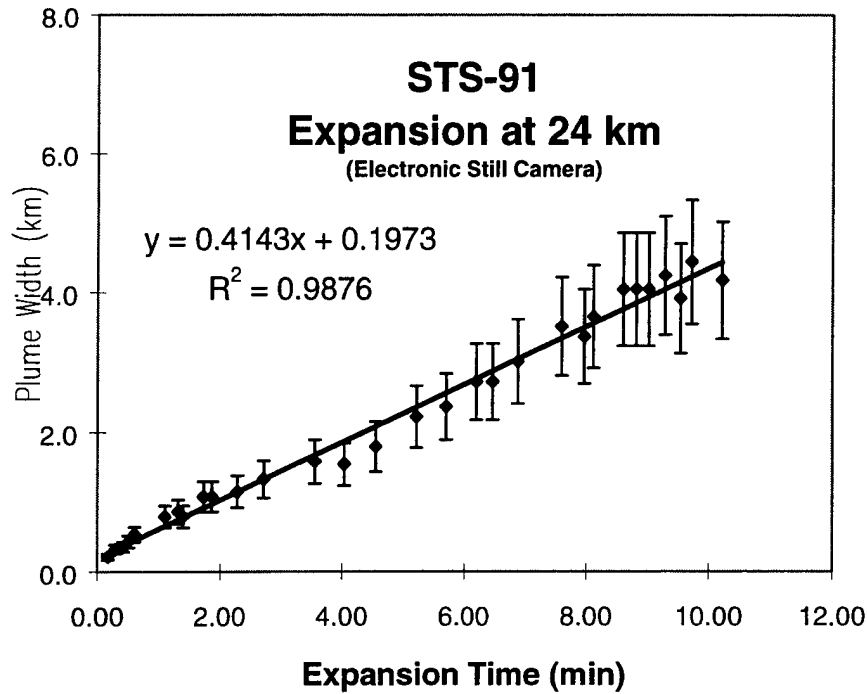


Figure 7-5. Plume width at an altitude of 24 km as a function of expansion time from the Haulover camera site taken with the electronic still camera.

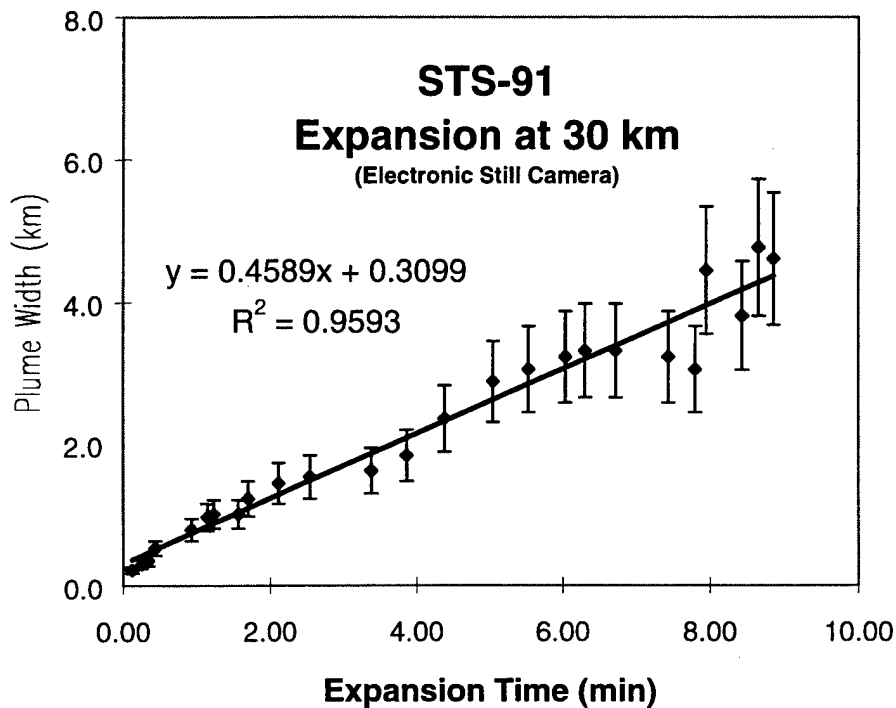


Figure 7-6. Plume width at an altitude of 30 km as a function of expansion time from the Haulover camera site taken with the electronic still camera.

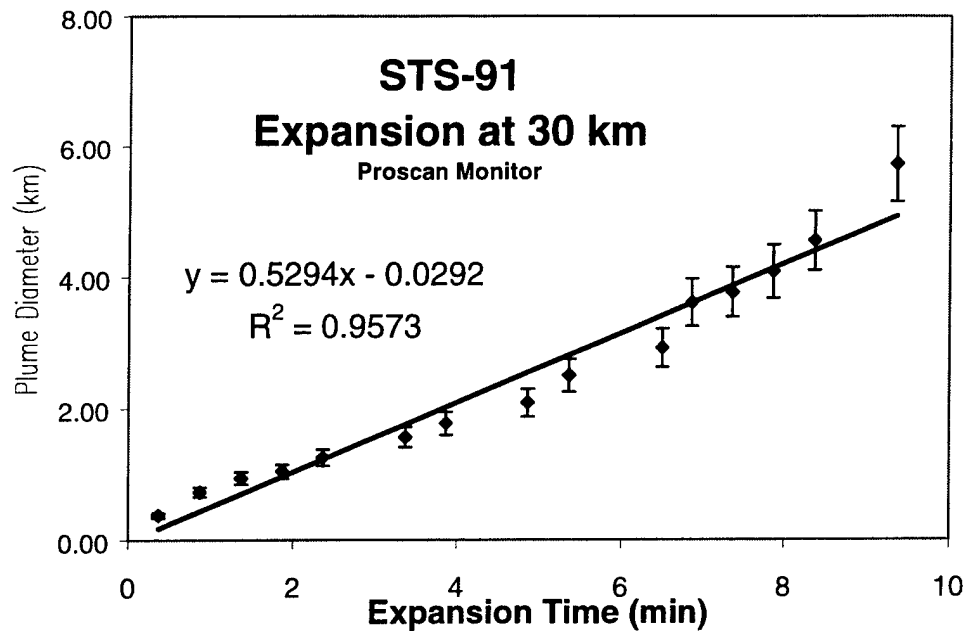


Figure 7-7. Plume width at 30 km as a function of expansion time from Hau-  
lover taken with the camera assigned to observe the plume in the  
altitude of 30 km.

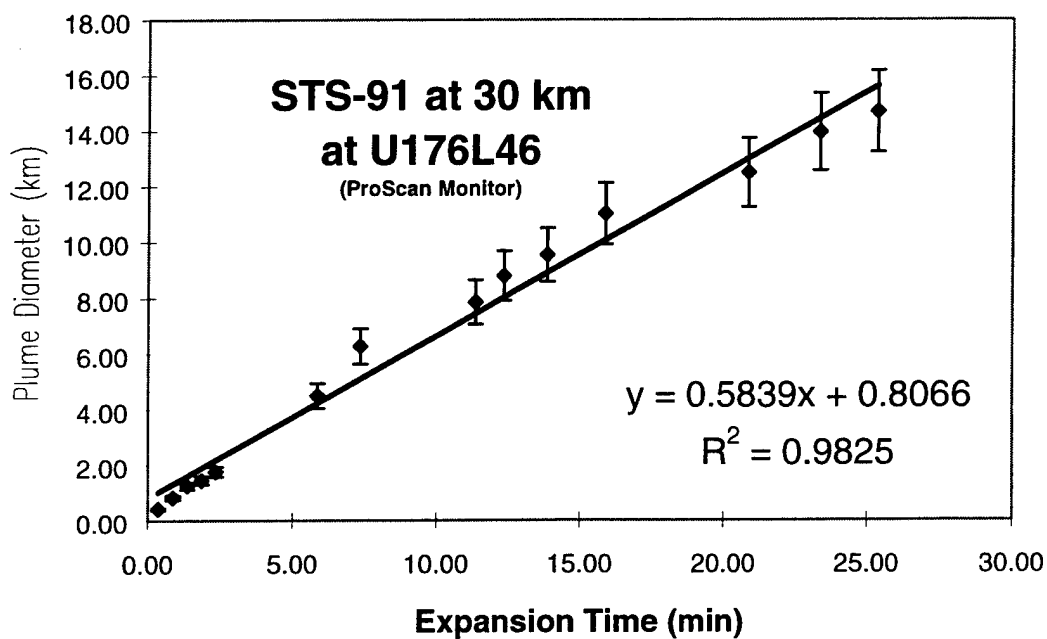


Figure 7-8. Plume width at 30 km as a function of expansion time from  
U176L46 taken with the camera assigned to observe the plume in  
the altitude range of 24 - 30.

The composite expansion rates measured are listed in Table 7-1. The time interval in minutes for which the widths were measured are listed next to the expansion rates. The principal results from these measurements are: the plume expansion rates at 18, 24, and 30 km altitude measured increased monotonically with altitude, in agreement with the general trend seen from the previous measurements; and the magnitude of the expansion rates are consistent with those observed in the previous observation for the respective altitudes and within the deviations of the previous measurements. The plume motion was consistent with rawinsonde velocities of approximately 10 m/s measured 0.5 h after the rocket passed through the stratosphere.

Table 7-1—STS-91 Expansion Rates

Alt (km)	STS-91	
	(km/m)	(min)
18	0.31	50
24	0.41	10
30	0.58	25

## TECHNOLOGY OPERATIONS

The Aerospace Corporation functions as an "architect-engineer" for national security programs, specializing in advanced military space systems. The Corporation's Technology Operations supports the effective and timely development and operation of national security systems through scientific research and the application of advanced technology. Vital to the success of the Corporation is the technical staff's wide-ranging expertise and its ability to stay abreast of new technological developments and program support issues associated with rapidly evolving space systems. Contributing capabilities are provided by these individual organizations:

**Electronics Technology Center:** Microelectronics, VLSI reliability, failure analysis, solid-state device physics, compound semiconductors, radiation effects, infrared and CCD detector devices, data storage and display technologies; lasers and electro-optics, solid state laser design, micro-optics, optical communications, and fiber optic sensors; atomic frequency standards, applied laser spectroscopy, laser chemistry, atmospheric propagation and beam control, LIDAR/LADAR remote sensing; solar cell and array testing and evaluation, battery electro-chemistry, battery testing and evaluation.

**Mechanics and Materials Technology Center:** Evaluation and characterizations of new materials and processing techniques: metals, alloys, ceramics, polymers, thin films, and composites; development of advanced deposition processes; nondestructive evaluation, component failure analysis and reliability; structural mechanics, fracture mechanics, and stress corrosion; analysis and evaluation of materials at cryogenic and elevated temperatures; launch vehicle fluid mechanics, heat transfer and flight dynamics; aerothermodynamics; chemical and electric propulsion; environmental chemistry; combustion processes; space environment effects on materials, hardening and vulnerability assessment; contamination, thermal and structural control; lubrication and surface phenomena.

**Space and Environment Technology Center:** Magnetospheric, auroral and cosmic ray physics, wave-particle interactions, magnetospheric plasma waves; atmospheric and ionospheric physics, density and composition of the upper atmosphere, remote sensing using atmospheric radiation; solar physics, infrared astronomy, infrared signature analysis; infrared surveillance, imaging, remote sensing, and hyperspectral imaging; effects of solar activity, magnetic storms and nuclear explosions on the Earth's atmosphere, ionosphere and magnetosphere; effects of electromagnetic and particulate radiations on space systems; space instrumentation, design fabrication and test; environmental chemistry, trace detection; atmospheric chemical reactions, atmospheric optics, light scattering, state-specific chemical reactions and radiative signatures of missile plumes.

**Center for Microtechnology:** Microelectromechanical systems (MEMS) for space applications; assessment of microtechnology space applications; laser micromachining; laser-surface physical and chemical interactions; micropropulsion; micro- and nanosatellite mission analysis; intelligent microinstruments for monitoring space and launch system environments.

**Office of Spectral Applications:** Multispectral and hyperspectral sensor development; data analysis and algorithm development; applications of multispectral and hyperspectral imagery to defense, civil space, commercial, and environmental missions.